

**Analyse von Erdzeitenbeobachtungen
zur Bestimmung der Parameter der
Erdkernresonanz**

**Analysis of Earth Tide Observations
for the Determination of Core Resonance
Parameters**

Zur Erlangung des akademischen Grades eines

DOKTORS DER NATURWISSENSCHAFTEN

von der Fakultät für Physik der
Universität (TH) Karlsruhe

genehmigte

DISSERTATION

von

Dipl.-Geophys. Gudrun Polzer
aus Zöschingen / Dillingen(Donau)

Tag der mündlichen Prüfung:

Referent:

Korreferent:

7. November 1997

Professor Dr. Helmut Wilhelm

Professor Dr. Hans-Georg Wenzel

Zusammenfassung

Geodynamische Phänomene reichen von Plattentektonik über postglaziale Hebungen zu Gezeiten der festen Erde, seismischen Eigenschwingungen und Raumwellen und überdecken damit ein breites Spektrum von Zeitskalen und Amplituden. Zu diesen Vorgängen zählen auch die Rotationsbewegung der Erde, Schwankungen der Tageslänge, Nutationen und Polschwankungen oder „Wobbles“. Allgemein spricht man von einem „Wobble“, wenn im einfachsten Fall ein homogener, starrer, symmetrischer Körper um eine Achse rotiert, die relativ zu seiner Figurenachse geneigt ist. Dieser „Wobble“ ist dann für einen Beobachter, der sich auf dem Körper befindet, als Bewegung der Rotationsachse um die Figurenachse wahrnehmbar. Damit verknüpft ist eine Nutation im raumfesten System. Hier wird der Konvention gefolgt, in der die Bewegung der Rotationsachse um den Vektor des Gesamtdrehimpulses des Systems als Nutation bezeichnet wird [z.B. *Rochester et al.*, 1974]. Bestimmt man die Charakteristika eines „Wobble“ aus Messungen auf der Erde, so kann man auf den Aufbau der Erde rückschließen. Das ist Ziel dieser Arbeit.

Hier wird ein Zweischicht-Erdmodell, das aus einem flüssigen Kern und einem elastischen Mantel aufgebaut ist, betrachtet. Die Begrenzungsfläche der beiden Bestandteile des Erdmodells bildet eine elliptische Kern-Mantel-Grenze (CMB). Die Frequenzen der Eigenschwingungsmoden dieses Systems erhält man analog zum kräftefreien Kreisel [z.B. *Sommerfeld*, 1964]. Die theoretische Beschreibung (Kapitel 5) folgt *Hinderer et. al* [1982] mit der Betrachtung der gravitoelastischen Deformation der rotierenden, hydrostatisch vorgespannten Erde aufgrund eines äußeren Drehmoments und der Heranziehung der Euler-Gleichungen zur Drehimpulserhaltung. Die resultierenden Bewegungsgleichungen im körperfesten Koordinatensystem (Liouville-Gleichungen) lassen sich aufspalten in den Kern und den Mantel betreffende Terme und mit einem Störansatz lösen. Den wesentlichen Anteil der Wechselwirkung zwischen Mantel und Kern trägt die Trägheitskopplung über den Druck an der CMB bei [z.B. *Toomre*, 1974]. Ein einfaches Modell erklärt das Auftreten von Trägheitskopplung, wenn die Rotationsachse des elliptisch begrenzten flüssigen Kerns und die Figurenachse des Mantels nicht parallel sind. Dann werden Flüssigkeitspartikel, die am Äquator umlaufen, auf eine engere Bahn gezwungen. Es entsteht ein nichthydrostatischer Druck auf die CMB. Die Erde reagiert als Kreisel mit einem „Wobble“ im erdfesten System und einer damit verknüpften Nutation im raumfesten System.

Die Eigenlösungen des Systems, die Eigenmoden als freie Schwingungen des genannten Erdmodells erhält man, wenn keine äußeren Drehmomente wirken. Zwei Rotationsmoden bilden diese Lösungen: der prograde „Chandler-Wobble“, der dem „Euler-Wobble“ beim Modell eines homogenen, rotierenden Ellipsoids entspricht und eine retrograde Mode, der „Nearly Diurnal Free Wobble“ (NDFW) [z.B. *Rochester et al.*, 1974]. Diese Arbeit beschränkt sich auf den NDFW. Der NDFW stellt zusammen mit einer Nutation im Inertialsystem des Fixsternhimmels, der „Free Core Nutation“ (FCN) [*Herring et al.*, 1986], zwei Ausprägungen der Mode einer rotierenden Zweischicht-Erde mit elliptischer CMB dar, die schon letztes Jahrhundert [*Hough*, 1895] theoretisch vorhergesagt wurde. Wäre die CMB sphärisch und

gäbe es keine visko–magnetischen Wechselwirkungen, dann wäre die Kernbewegung vollkommen unabhängig von der Mantelbewegung. Die Mode NDFW/FCN würde dann nicht existieren.

Die freie Schwingung konnte in der Schwere noch nicht nachgewiesen werden. Jedoch detektierten *Herring und Dong* [1994] die frei angeregte Nutation, deren Amplitude um Größenordnungen stärker ist, in astronomischen Messungen. Im Druckfeld der Atmosphäre scheint genügend Energie mit passender räumlicher (tesseraler) und zeitlicher (ganztägiger) Verteilung vorhanden zu sein, um eine zufällige Anregung zu ermöglichen [*Herring und Dong*, 1994]. Da es sich bei dem NDFW und der FCN um zwei Ausprägungen eines physikalischen Phänomens handelt, sind die Eigenkreisfrequenz des NDFW und die Periode der FCN gekoppelt. NDFW–Frequenzen können auch als FCN–Perioden ausgedrückt werden und umgekehrt.

Im Unterschied zur freien Schwingung führt das System Erde bei äußerer Anregung erzwungene Schwingungen aus. Die Gezeitenkräfte von Mond, Sonne und Planeten im ganztägigen Periodenbereich repräsentieren die periodische Anregung. Wegen der unterschiedlichen Antwort von flüssigem Kern und elastischem Mantel auf das anregende Potential existiert eine differentielle Rotation zwischen diesen beiden Bestandteilen der Erde. Diese Relativbewegung kann man in der Gezeitenantwort der Erde als Resonanzverstärkung der Gezeitenadmittanzen nachweisen. Die Beobachtung der Gezeiteneffekte der festen Erde liefert so Informationen über die Antwort der Erde auf das astronomisch genau ermittelte Gezeitenanregungspotential von Mond, Sonne und Planeten und kann deswegen benutzt werden, um auf die Struktur des Erdinnern zu schließen. Eine Motivation für diese Arbeit war, daß man mit seismologischen Methoden keine vergleichbare Auflösung im Tiefenbereich der CMB erreichen kann. Gezeiten der festen Erde können in Deformationen oder Massenumverteilungen nachgewiesen werden, die zu Schwereänderungen an der Oberfläche, Dehnungen der Kruste und Neigungen relativ zum lokalen Lot führen. Obwohl an der Erdoberfläche die Gezeitenschwereänderungen nur etwa ein Zehnmillionstel der Gravitation an der Erdoberfläche betragen, können sie besser als auf 1% aufgelöst werden. Die Gezeitenkräfte führen an Orten niedriger Breite zu Verschiebungsamplituden der Erdoberfläche von bis zu 40 *cm*.

Die Datenbasis zur Bestimmung des NDFW bilden in dieser Arbeit Registrierungen der Gezeiten der festen Erde von hoher Qualität, die am geowissenschaftlichen Gemeinschaftsobservatorium der Universitäten Stuttgart und Karlsruhe in Schiltach im Schwarzwald (BFO) aufgezeichnet wurden. Bei den Instrumenten handelt es sich um das LaCosteRomberg–Gravimeter ET19 mit elektrostatischem Feedback, das Cambridge–Invar–Strainmeter St3 und das Askania–Bohrlochpendel BLP10 (Kapitel 2 und Appendix A–C). Unter anderem wurde diese Arbeit motiviert durch die verbesserte Datenqualität der Station BFO im Vergleich zu älteren Registrierungen, durch die Möglichkeit der Stapelung von Datensätzen verschiedener Instrumente, sowie durch die Verfügbarkeit einer genaueren Gezeitenpotentialentwicklung und eines neuen Ozeangezeitenmodells.

Die Gezeitenanalyse wurde mit dem Gezeitenanalyse–Paket ETERNA durchgeführt [*Wenzel*, 1994b; *Wenzel*, 1994c; *Wenzel*, 1996] (Kapitel 3). Als Erdmodell dient ein elliptischer, gleichförmig rotierender Körper mit flüssigem äußeren Kern in

inelastischem Mantel (PREM-Modell [*Dziewonski und Anderson, 1981*]) mit abgeplatteter CMB ohne Berücksichtigung der Ozeane. Ebenso wie die feste Erde unterliegen die Ozeane (Amplituden bis $\pm 5 m$) und die Atmosphäre den periodischen Gezeitenkräften. Durch die Ozeanauflast kann sich die Amplitude um weitere $10 cm$ erhöhen. Für die NDFW-Untersuchung werden die Effekte der Ozeangezeiten auf die feste Erde (Auflastgezeiten) durch Korrekturterme kompensiert (Kapitel 4). Die Ozeankorrekturen [*Agnew, 1995*] gehen auf Ozeangezeitenmodelle aus den modernsten Ozean-Altimeterdaten der TOPEX/POSEIDON-Mission zurück [*Le Provost et al., 1994; Eanes und Bettadpur, 1995*]. Die Reaktionen der Atmosphäre auf die Gezeitenanregung sind gering ($\pm 0.03 hPa$), aber große Gezeitenamplituden sind im Luftdruck aufgrund der tagesperiodischen Wärmeeinstrahlung durch die Sonne [z.B. *Chapman und Lindzen, 1970*] zu finden. Wie sich diese globalen Wellen des Luftdruckes [z.B. *Crossley et al., 1995*] auf Schweremessungen auswirken, wird in Kapitel 8 untersucht. Große Effekte auf die feste Erde und die Instrumentenmassen werden von wetterbedingten Druckschwankungen aufgrund von Dichteveränderungen der Luftmassen ($\pm 30 hPa$) produziert. Um diese Wettereinflüsse zu unterdrücken, wird in der Gezeitenanalyse auch immer simultan der Luftdruck angepaßt.

Der Resonanzanteil in der Gezeitenantwort wird hier isoliert und in bezug auf einen harmonischen Oszillator interpretiert [*Neuberg, 1987*] (Kapitel 5). Für die NDFW-Anpassung werden die Tiden O_1 , P_1 , K_1 , ψ_1 und ϕ_1 herangezogen. Die letzten vier Tiden werden stark von der Resonanz in Amplitude und Phase beeinflusst, die Tide O_1 dient als Referenztide. Das funktionale Modell für die Resonanz entspricht dem von *Neuberg et al. [1987]* und weiteren Autoren. Es handelt sich um das Modell eines harmonischen Oszillators mit einer Eigenfrequenz, einem Dämpfungsfaktor und einer komplexen Resonanzstärke.

Um aus den Daten ein Modell zu extrahieren, werden die Abweichungen zwischen Daten und Modell minimiert (Kapitel 6). Hier wird die Methode der kleinsten Fehlerquadrate angewendet. Um das dabei entstehende Gleichungssystem zu lösen, wird einerseits die Singulärwert-Zerlegung benutzt, andererseits wird eine Simplex-Methode zur Minimierung von Funktionen [*Nelder und Mead, 1965*] mit Nebenbedingung angewendet. Die Nebenbedingung soll verhindern, daß die Dämpfungskonstante negative Werte annimmt, was physikalisch nicht sinnvoll ist.

Die FCN-Perioden, die in dieser Arbeit bestimmt wurden, sind alle beträchtlich kleiner als theoretische Vorhersagen und bisher veröffentlichte Analysen aus anderen Datensätzen. Für die Gravimeter-Daten, die die höchste Güte besitzen, wurde die kleinste Resonanzperiode $T_{FCN} = 405.8 \pm 4.2 \text{ siderische } d (\text{sid. } d)$ bestimmt. Die gemeinsame Anpassung von Schwere- und Strangezeitenparameter an ein Resonanzmodell liefert $T_{FCN} = 412.6 \pm 4.2 \text{ sid. } d$. Bei allen hier durchgeführten Analysen liegen die Schätzwerte für den Dämpfungsfaktor sehr nah bei 0.

Wegen der Abweichungen der Ergebnisse der FCN-Perioden zu Untersuchungen anderer Autoren wurde in dieser Arbeit sehr viel Wert auf die Fehlerbetrachtung gelegt (Kapitel 7). So wird die Fehlerfortpflanzung von den Gezeitenadmittanzen in die NDFW-Parameter detaillierter als bisher untersucht. Einerseits wurden Monte-Carlo-Simulationen durchgeführt, andererseits wurde gezeigt, wie sich systematische Störungen der Gezeitenparameter und Ozeankorrekturen in den Unsicherheiten der

NDFW-Parameter niederschlagen. So stellte sich heraus, daß die entscheidende Fehlerquelle bei den Gezeitenparametern lag. Einen breiten Raum nehmen auch Luftdruckeffekte und deren Einfluß auf die Schweremessungen und letztendlich auf die NDFW-Parameter ein (Kapitel 8). Aus den Untersuchungen ergab sich, daß sich die Luftdruckeffekte nicht maßgeblich auf die NDFW-Periode auswirken.

Theoretische Berechnungen der Resonanz beruhen auf einem Erdmodell, bei dem sich der Erdkern im hydrostatischen Gleichgewicht befindet [z.B. *Wahr*, 1981]. Die Mehrzahl der publizierten Beobachtungen zeigt aber eine Frequenzverschiebung weg von der theoretisch ermittelten Resonanzstelle. Diese Frequenzverschiebung wird hier als erhöhte Elliptizität der CMB interpretiert [*Neuberg*, 1987]. Mit Annahmen über die Dichte des Kerns und die Elastizität des Mantels führen die beschriebenen Beobachtungen der Station BFO auf einen um 500 – 700 m reduzierten polaren Kernradius. In der Literatur werden noch andere geophysikalische Beobachtungen wie Raumwellenlaufzeiten [z.B. *Doornbos und Hilton*, 1989] und Eigenschwingungen des gesamten Erdkörpers zur Abschätzung der CMB-Topographie verwendet. Hier wird exemplarisch gezeigt, wie Strukturkoeffizienten, die aus der Aufspaltung von Eigenschwingungsmoden gewonnen wurden [*He und Tromp*, 1996; *Widmer et al.*, 1992(a)], zur Bestimmung der Elliptizität der CMB herangezogen werden können (Kapitel 9). Die Auflösung für die nichthydrostatische Elliptizität der CMB, die aus Strukturkoeffizienten resultiert, ist sehr viel geringer als diejenige aus NDFW/FCN-Analysen.

Abstract

High quality records of earth tides from the Black Forest Observatory (BFO) have been analyzed to estimate parameters of the Nearly Diurnal Free Wobble (NDFW) which together with the Free Core Nutation (FCN) represent two different aspects of the same free mode of the rotating Earth with elliptical core–mantle boundary (CMB). When the figure axis of the mantle and instantaneous rotation axis of the core become misaligned, then torques at the CMB arise which try to realign these two axes. The Earth reacts as a gyroscope with a wobble in the earth–fixed system and an associated nutation in the inertial system of space. A direct observation of the free mode has only recently been reported for the FCN. Until now the intrinsically excited wobble of smaller amplitude could not be detected in the spectrum of orientation changes in the earth rotation, but in the Earth’s response to tidal forcing evidence is found for its existence: diurnal tidal waves in close proximity to this eigenmode in the frequency domain experience a resonant amplification. This resonance in the observed tidal admittances can be quantified with the help of the harmonic oscillator model which relates the observed tidal admittances to the parameters describing the NDFW. With the functional dependence being non–linear the inversion for the NDFW parameters is performed by a linearized least squares method.

Tidal forces not only act on the solid Earth but also on the world oceans and the surrounding atmosphere. In turn these two parts of the Earth contaminate the observations of the solid earth tides. The frequency dependent ocean effects are the direct Newtonian attraction of the sensor mass and the effects of deformation of the Earth due to loading by the periodically shifting water masses. Because of that ocean load corrections based on the most recent altimeter data from the TOPEX/POSEIDON mission are applied to the tidal admittances. No significant influences on the NDFW parameters with respect to an older, commonly used ocean load model has been found.

The gravitational reactions of the atmosphere to the tidal forces are rather small, but there are large tides in the atmosphere for solar constituents due to the radiational energy input from the Sun. Additionally broad–band noise of meteorological origin due to density variations of air masses has to be corrected for. Efforts are undertaken to study especially the air pressure–gravity admittance. These investigations reveal that the influence of the air pressure–gravity admittance on the NDFW period is only small.

The gravity and strain data from BFO are of very high quality. For the data set with the best quality, namely gravity, an equivalent FCN period of $T_{FCN} = 405.8 \pm 4.2 \text{ sid. d}$ was obtained. The joint inversion of gravity and strain tidal parameters results in $T_{FCN} = 412.6 \pm 4.2 \text{ sid. d}$. All these resonance periods are well below the majority of previously published values. Since dissipative mechanisms are conceivable besides the resonance period also the quality factor Q has been determined simultaneously. The Q estimates of this work are very high. Theoretical calculations for the resonance are based on an earth model in hydrostatic equilibrium. But the majority of observations cannot confirm these theoretically determined values for the resonance period. In this work the shift between the resonance frequency of a non–

hydrostatically prestressed earth model and the resonance frequency resulting from observations is interpreted as excess ellipticity of the CMB. For a hydrostatically prestressed Earth the mean polar radius of the outer core of about 3480 km [Yoder, 1995]. is reduced due to the rotation by 9 km . Under appropriate assumptions the obtained frequency shift is equivalent to an additional reduction of the polar radius of the outer core of $500 - 700\text{ m}$. In the literature geophysical data of various kind are used to constrain the CMB ellipticity. As an example it is shown that recent normal mode splitting analyses for the retrieval of the structure coefficient c_2^0 cannot provide comparable tight bounds for the core ellipticity.

Salient in this work is the assessment of the parameter uncertainties. Especially the error propagation from the noise in the tidal admittances to the NDFW parameters is tried to be assessed more realistically than this has been done so far. Monte Carlo simulations have been performed and also the effects of systematic perturbations are studied. It turns out that the uncertainties in the tidal admittances are the most serious error source for estimating NDFW parameters.

Contents

1	Introduction	1
2	Description of station and data	7
2.1	Station and instruments	7
2.2	Data processing	9
3	Earth tides	11
3.1	Theoretical earth tides	12
3.2	Tidal Analysis	17
4	Ocean and air pressure correction	23
4.1	Ocean load correction	23
4.2	Air pressure correction	26
5	Theoretical aspects of the wobble	29
5.1	A force free gyroscope	29
5.2	The Earth – a gyroscope	30
5.2.1	Free Wobble	37
5.2.2	Forced Wobble	39
5.3	The model of the classical harmonic oscillator	40
6	Estimation of the NDFW Parameters	42
6.1	Linearized least squares method	43
6.2	Singular value decomposition (SVD)	44
6.3	Nelder–Mead simplex method	45
6.4	Inversion results	46
7	Confidence intervals for the NDFW parameters	51
7.1	Variances from F–statistics	52
7.2	Propagation of deterministic errors	56
7.3	The Monte Carlo simulation	63
8	Investigations of air pressure	73
8.1	Air pressure–gravity admittance	73
8.2	Possible modulations of S_1	77

9 Interpretation with respect to CMB ellipticity	83
9.1 CMB ellipticity from other geophysical data	85
9.1.1 Normal mode splitting and CMB ellipticity	86
10 Conclusions and outlook	91
Glossary of notations	94
References	96
A The instrument responses	104
B Tidal observations	106
C Comparison with Noise Models	108

Chapter 1

Introduction

Viscoelastic processes within the Earth lead to a wide variety of geophysical phenomena that are characterized by extremely different timescales and levels of stress. These phenomena include glacial isostatic adjustment as well as the anelasticity effects evident in solid body tides, luni-solar nutations and wobbles.

On the turn of the century observation of the solid earth tides were of considerable interest in understanding the global elastic response of the Earth to applied forces, as well as providing information on the major subdivision of the Earth into mantle and core. Since that time the interior of the Earth has been further investigated revealing the elastic structure of its components crust, mantle, outer fluid and inner solid core. Nowadays observations of free oscillations at seismic frequencies certainly provide more insight in the global radial structure of the planet than tidal observations. Tidal gravity variations which are only about 10^{-7} of the gravitational attraction of the Earth can be resolved with the help of modern instrumentation at quiet stations to better than 1% [*Richter et al.*, 1995]. Nevertheless it is intriguing that tidal observations allow to constrain the ellipticity of the fluid outer core of the Earth with a resolution which cannot be attained by other geophysical data [eg. *He and Tromp*, 1996; *Widmer et al.*, 1992(a)]. The shape of the interface confining the fluid core, the core-mantle boundary (CMB) is of particular interest, since its topography additionally to thermal and chemical processes near the CMB play a major role in the planet's evolution, influencing the magnetic field behaviour, chemical cycling in the mantle, irregularities in the rotation and gravitation of the Earth, and the configuration of mantle convection.

Any homogeneous, rigid, ellipsoidal, rotating body (which represents a force-free gyroscope) supports a rotational eigenmode when the figure axis becomes misaligned with the rotation axis of the body. The resulting motion of the rotation axis around the figure axis is called Eulerian wobble. Associated with this motion in the body-fixed reference frame is the motion of the rotation axis around the axis of total angular momentum in inertial space, the associated Euler nutation. For a homogeneous, rigid earth model this wobble would have an eigenperiod of 306 *d*.

A more interesting model in view of the Earth is a 2-layer sphere consisting of a homogenous, incompressible, frictionless, fluid core surrounded by a rigid mantle. If non-mechanical coupling mechanisms between the core and the mantle are excluded motions of these two earth components are almost independent of each other. A modification of this model would be the introduction of an ellipsoidal CMB which gives rise to dynamical coupling between core and mantle. [*Lamb*, 1932]. This results in two free modes of rotation. Besides the Eulerian wobble a wobble with nearly diurnal period comes into existence. A more realistic earth model must take into consideration the elastic properties of the mantle. If the elastic deformations are only small then perturbation theory can be used to find solutions of the equations of motion. This model supports also two eigenmodes: the prograde Chandler wobble (435 *d*) with its associated nutation and the retrograde Nearly Diurnal Free Wobble (NDFW) with the associated Free Core Nutation (FCN). The NDFW and the FCN are two aspects of one free mode which is sometimes in the literature also called core resonance [eg. *Wahr*, 1981].

Since the fluid core and the elastic mantle respond differently to the luni-solar tidal force, there exists a differential rotation between mantle and core (Fig. 1.1). This differential core-mantle motion leads to resonant elastic deformation which represents a normal mode of the rotating Earth. A simple way to describe the characteristics of this mode is the Poincot representation [eg. *Rochester et al.*, 1974]. The wobble is felt in an earth-fixed system, whereas the nutation can be observed in the inertial system of space. The deformations result in gravity changes, strains and tilts observable at the earth surface [eg. *Hinderer et al.*, 1991] and nutations in space.

The observation of solid earth tides provides information on the Earth's response to a known force and can therefore be used to constrain certain properties of the earth interior. From the theory of linear systems we know that the response of a system to a known input allows to determine the system transfer function. Our system is the Earth (Fig. 1.2). The input to the system is the accurately known tidal forcing function by the Moon and Sun and planets [*Wenzel*, 1994b; *Wenzel*, 1994c, *Wenzel*, 1996] $x(t)$ in the time domain or $X(\omega)$ in the frequency domain. The system output, which includes the response of the Earth due to the NDFW is represented by registrations of for example tidal gravity variations, tidal deformations or nutations denoted by $y(t)$ in the time domain or $Y(\omega)$ in the frequency domain. The aim is to estimate the transfer function $H(\omega)$ in the vicinity of the core resonance period, in order to constrain the physical properties in a restricted frequency and space region. Fitting a theoretic tidal model to the tidal observations results in dimensionless tidal parameters (the so-called Love numbers) for an elastic Earth and subsequently allows to isolate the resonant part in the response. With the help of a theoretic model for the core resonance, namely the damped harmonic oscillator [*Neuberg et al.*, 1987], the NDFW parameters inherent in $H(\omega)$ can be determined by an inversion.

In Fig. 1.3 a simplified geophysical scenario with effects important for the nearly diurnal free wobble is depicted. This simple 2-layer earth model with elliptical

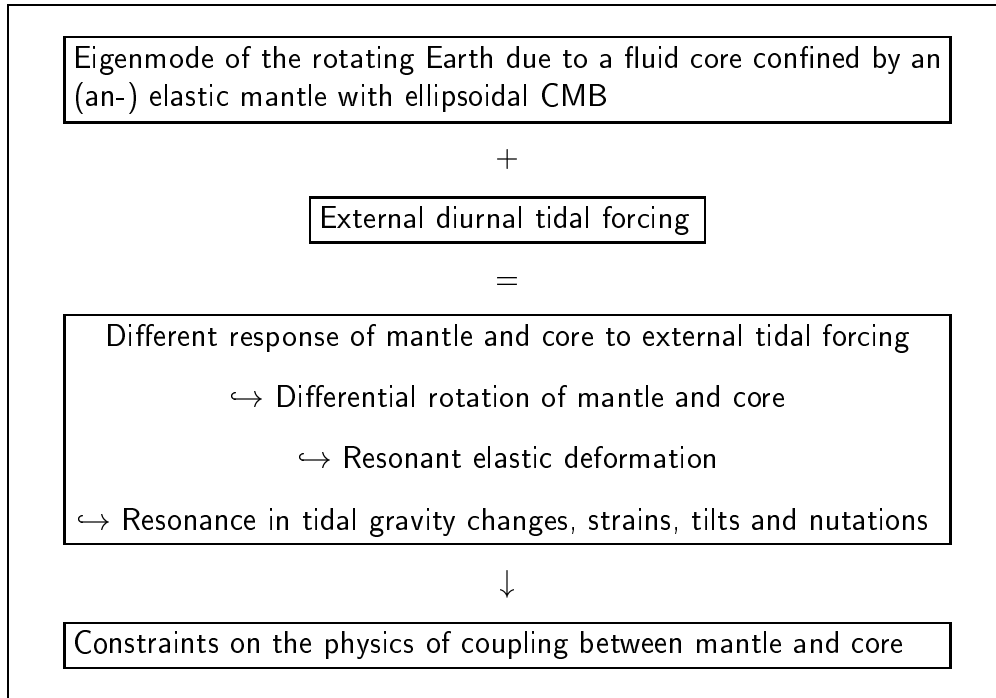


Figure 1.1: Synopsis of NDFW or core resonance effect.

core–mantle boundary supports the NDFW. The wobble is excited by periodic tidal forcing of the Moon and Sun. For the transient excitation of the wobble atmospheric pressure forces (winds) are under discussion [Herring and Dong, 1994]. If the CMB would be spherical and no coupling mechanisms between core and mantle would exist they could rotate totally independent and no NDFW would exist. Possible coupling mechanisms are viscous, electromagnetic and inertial coupling [eg. Toomre, 1974]. Not only the solid Earth, but also the oceans and the atmosphere are subjected to tidal forces. Their tidal responses together with the solar heating tide [Crossley *et al.*, 1995] and meteorological effects in the atmosphere have to be eliminated. Therefore the corresponding corrections are applied [eg. Agnew, 1995; Merriam, 1994].

Already a century ago there has been a theoretical prediction of this wobble [Hough, 1895]. But only in the last twenty years the quality of the instruments recording tidal signals made a verification possible [Gwinn *et al.*, 1986; Richter and Zürn, 1988]. In Neuberg [1987] and Neuberg *et al.* [1987] a record from the LaCoste–Romberg Gravimeter ET–19 at the Black Forest Observatory (BFO) was included in a stack of six gravimeter records from Central Europe to retrieve the parameters of the NDFW.

The new digital records of this work obtained at BFO (consisting of gravity, strain and tilt data) should show the improvement of the data which should be much less noisy and therefore better suited for an analysis for NDFW parameters. Another motivation for the analysis is the availability of new ocean tide models

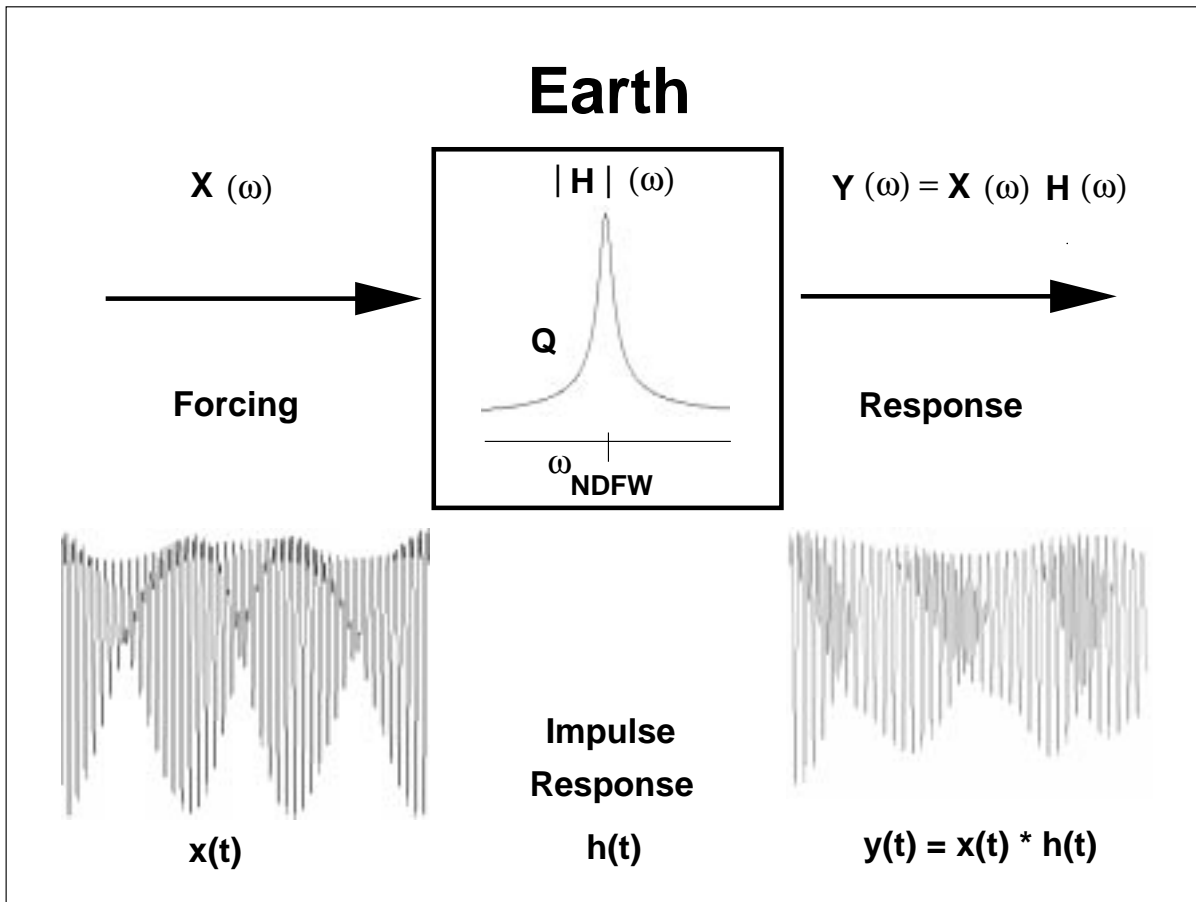


Figure 1.2: Illustration of the extraction of the core resonance from tidal data. On the upper panel a flow chart known from the theory of linear systems is sketched. The input to the system is the forcing denoted by $X(\omega)$. The output is represented by the response $Y(\omega) = X(\omega) H(\omega)$. The resonance can be determined by the frequency dependence of the tidal admittance function $H(\omega)$ in the vicinity of ω_{NDFW} . On the lower panel the corresponding time series are found with $h(t)$ representing the impulse response of the system and $*$ denoting the convolution. The essential features in this figure are enormously exaggerated.

after the first years of the TOPEX/POSEIDON mission [*Le Provost et al.*, 1995], promising improved estimates of ocean effects on earth tide recordings.

After this introduction of the topic of this work follows the description of the station BFO and the data collected at this site in Chapter 2. The tidal forcing is represented by the series expansion of the tidal potential of the Moon, Sun and planets in Chapter 3. The predictions for tidal gravity changes and deformations on the earth surface are found by solving the gravitoelastic problem. The correction of the influences of oceans and atmosphere including meteorological effects are the topic of Chapter 4. A summary of the theory of the dynamics of the core resonance which is based on a radially stratified reference earth model and Poincaré flow of

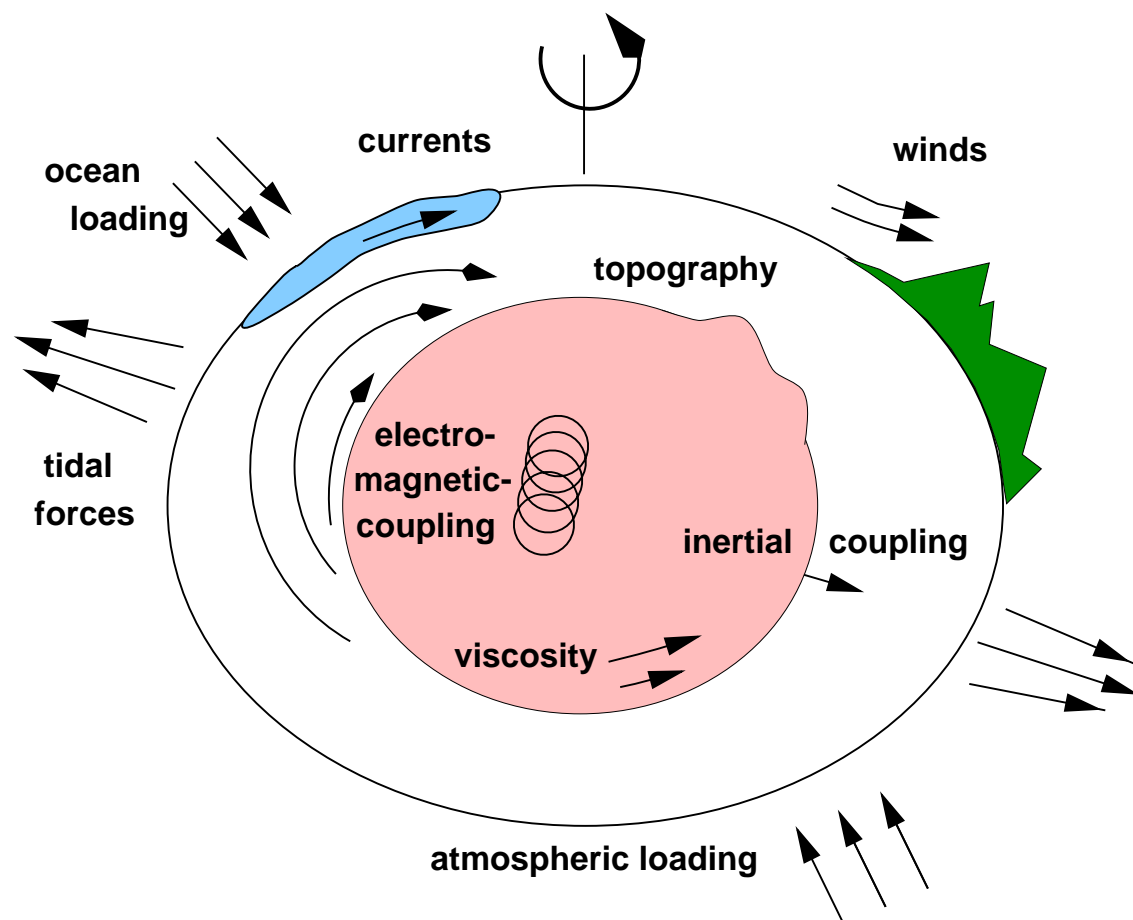


Figure 1.3: Geophysical scenario showing torques exerted on a simple, rotating 2-layer earth model (consisting of a fluid core confined by an elliptical container, the elastic mantle) which are related to the excitation, respectively, the observation of the nearly diurnal free wobble.

the core is found in Chapter 5. In this context the Poincaré representation for the NDFW is introduced. Also in this chapter the harmonic oscillator model for the core resonance with the non-linear dependence of the NDFW parameters resonance frequency, damping term and complex resonance strength on the reduced tidal admittances is presented. Different iterative inversion methods for the retrieval of the resonance parameters are described in Chapter 6. In this chapter also the results of this work are compared to published NDFW parameters. Additionally in this work a stack of gravity, strain and tilt tides is performed. The aim is to reduce besides the statistical errors, the systematic errors in the stack of different types of data. The uncertainties of the parameters are tried to be thoroughly assessed by systematic and random modifications of the input data to the NDFW analyses in Chapter 7. Further investigations are performed in order to reveal the influence of atmospheric effects (Chapter 8). The interpretation of the results obtained in this work with regard to CMB ellipticity together with estimates from other geophysical data including normal mode splitting observations are discussed in Chapter 9. After

the conclusions and outlook in Chapter 10 an appendix with the following contents is attached: The instrument responses are depicted in Appendix A, the spectra of the observations in Appendix B and a comparison of the residual data to published noise models is found in Appendix C.

Chapter 2

Description of station and data

2.1 Station and instruments

The digital gravity, strain and tilt registrations of the station Black Forest Observatory (BFO) which is situated in the southwest of Germany near the small town of Schiltach (48.33°N, 8.33°E, 587 m elevation above sea-level, see Fig. 2.1) are the basis for the NDFW investigations. The station BFO has been built as a joint facility of the Universities of Karlsruhe and Stuttgart. The instruments are installed in the granitic basement rock of a disused silver mine. An air-lock inside the mine in front of the instrument vaults should shield the instruments from direct effects of high frequency atmospheric pressure variations.

In the investigation recordings of the LaCoste-Romberg Gravimeter ET-19 with electrostatic feedback [*Richter et al.*, 1995], the EW-component of Askania bore-hole pendulum BLP10 and the Cambridge-Invar-Strainmeter St3 with an azimuth of N 300°E are used. The gravimeter measures the temporal variation of local vertical accelerations, the Askania pendulum the temporal variation of tilt relative to the local vertical and the strainmeter the temporal variation of linear strain. The instrument responses in the magnitude and phase representation of the respective transfer function are found in Appendix A. Data from this strainmeter and this Askania pendulum provided some of the best results on torsional free oscillations after the Macquarie Rise-quake of 1989 [*Widmer*, 1991; *Widmer et al.*, 1992(b)]. Diurnal tidal tilts in NS-direction at the latitude of BFO have very small amplitudes due to a theoretical node at 45°N, therefore this component was not included in our analysis. Additionally the local air pressure is registered with the microbarograph BM-G-06 in front of the air-lock in order to be able to correct air pressure induced effects by gravitation or deformation of the Earth on the other instruments.

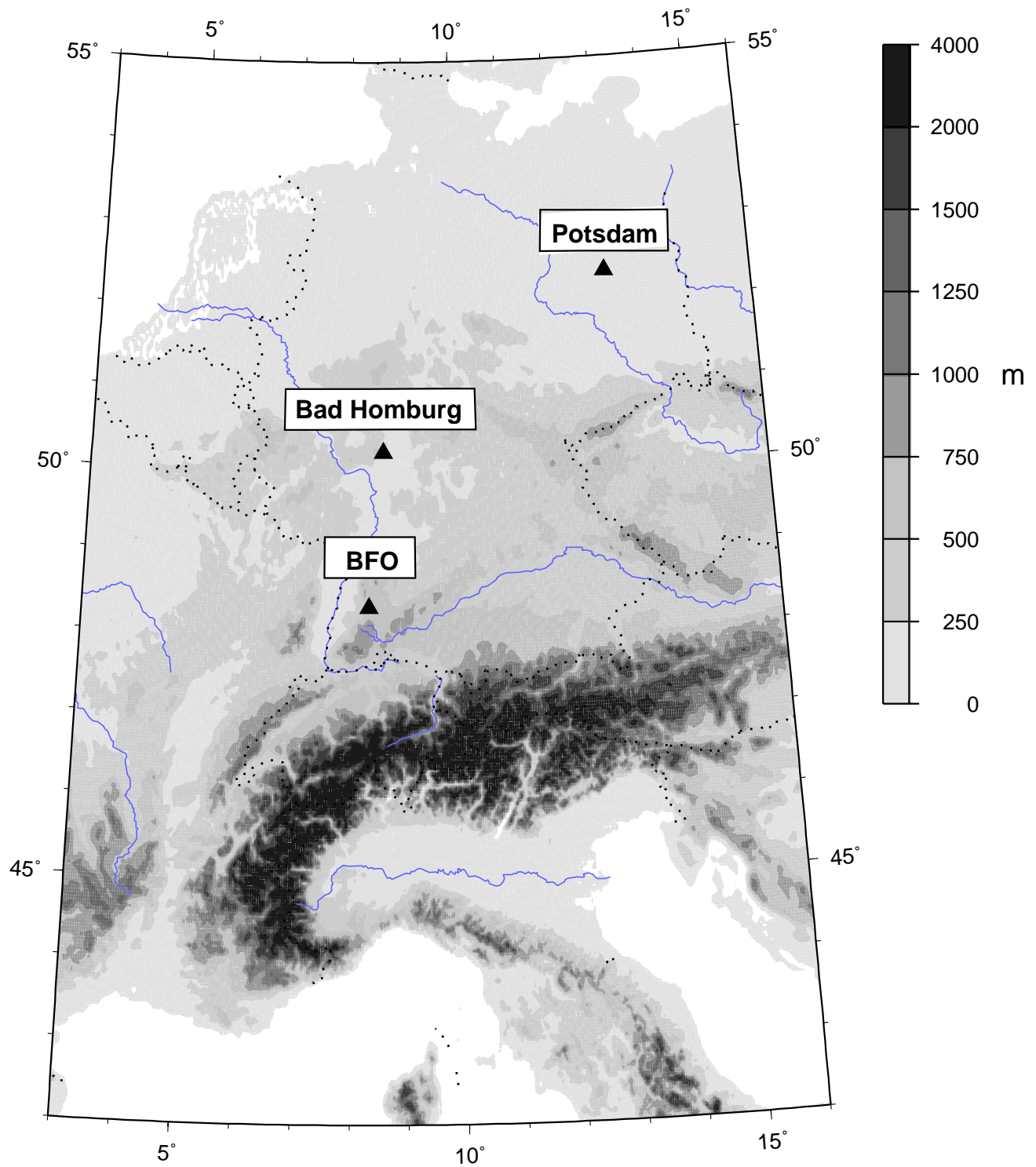


Figure 2.1: Topographic map of Central Europe given in Cassini Cylindrical projection – a compromise between conformal and equal-area projection. The triangles mark the station BFO and additionally the stations Bad Homburg and Potsdam, which are of concern in following chapters.

2.2 Data processing

The data were digitally recorded with 16 bit resolution at BFO with a sampling interval of 5 s after low-pass filtering with an 8-pole/25s Butterworth filter. The clock of the digitizing computer was kept synchronized to the millisecond with the DCF 77 time signal. The lengths of the records amount to approximately 13 months for gravity and tilt and 20 months for strain after the common start on November 23, 1988. The air pressure data in front of the air-lock were recorded and processed in the same manner as the tidal data. The analysis of tidal measurements for NDFW parameters requires tidal parameters of highest accuracy. Therefore the raw 5s data were carefully inspected for spikes and steps which were removed interactively, before the data were low-passed and resampled at 1-minute intervals. This procedure was very time-consuming. These data were then further processed with the pre-processing software PRETERNA [*Wenzel, 1994a*], filling gaps in the residuals with the help of a theoretical tidal model and the simultaneously recorded barometric pressure. Applying PRETERNA results in a time series resampled at the full hours.

The observations processed in the way described above are shown in the frequency domain in Appendix B. To show the improvement of the data quality at the station BFO old analog registrations are compared to the new digital data by means of histograms of residual data from tidal analysis in section 3.2. Additionally you find a comparison of residuals from tidal analysis and published noise models in Appendix C.

Chapter 3

Earth tides

Already at the beginning of this century ocean tide observations provided a possibility to estimate the Earth's shear modulus μ . From the differences of observations and theoretical calculations on the basis of a rigid earth model a shear modulus comparable to the rigidity of steel was found. Nowadays the core resonance verified in tidal registrations provides the only possibility to gain insight beyond seismological findings into the interior properties of the Earth with this kind of data.

Gravitation represents an inhomogeneous force field, so the forces exerted by the Moon, the Sun and the planets on the extended body of the Earth are dependent on the distance between the location at the Earth and the celestial body. This results on one hand in a torque on the rotating Earth tending to tip the Earth's rotation axis to bring it into a position perpendicular to the ecliptic or the orbital plane of the Moon respectively. On the other hand differential tidal forces arise which cause deformations and variations in the gravitational potential on the Earth. These effects comprise changes in gravity, tilt relative to the local vertical and strain in the crust.

The tidal forces of Moon, Sun and planets cause vertical displacements at the surface of the Earth up to 40 *cm*, variations in gravity and horizontal accelerations of 10^{-6} m/s^2 and tilts of hundred of *nrad*s respectively at moderate latitudes. Variations in linear strain are of the order of $50 \cdot 10^{-9}$. The loading due to the oceans can add another 10 *cm* to the displacement. Just like the solid Earth the oceans (amplitudes up to $\pm 5 \text{ m}$ and more) and the atmosphere are subjected to periodic tidal forces. For the NDFW analysis the load effects of the oceans on the solid Earth are a systematic noise signal. With the help of an ocean model these ocean signals can be estimated and subtracted (Chapter 4). The tides of the atmosphere are small ($\pm 0.03 \text{ hPa}$) compared to meteorological pressure variations ($\pm 30 \text{ hPa}$). Effects of air pressure variations on gravity are discussed in detail in Chapter 8.

3.1 Theoretical earth tides

In the following tensors and vectors are printed in bold face. For matrices capital letters are used. The tidal potential due to a massive body can be described in the following way:

$$V = \frac{GM}{r} \sum_{n=2}^{\infty} \left(\frac{R}{r}\right)^n P_n(\cos \zeta) \quad (3.1)$$

with Newton's gravitational constant G , the mass M of the tide-generating body, the mean radius of the Earth R and the mean distance r between the centre of gravity of the tide-generating body and an observation point A at the surface of the Earth, the Legendre polynomials P_n of degree n and the zenith angle ζ (angle between the observation point A and the tide-generating body in reference to the centre of the Earth). Terms of $n < 2$ do not contribute to differential forces within the Earth, but to the orbital motion ($n = 1$).

Sometimes it is convenient to express the relative positions of the observer on the Earth and the celestial body in a combination of geocentric and celestial coordinates. The geocentric coordinates are the spherical co-latitude θ and spherical longitude λ . The celestial coordinates of the tide generating body are the declination δ which means the angular distance north of the celestial equator and local hour angle τ which is defined as the difference in longitude between A and the tide-generating body. The potential can then be rewritten:

$$V = \frac{GM}{r} \sum_n^{\infty} \left(\frac{R}{r}\right)^n \frac{1}{2n+1} \sum_{m=0}^n P_n^m(\cos \theta) \cdot P_n^m(\sin \delta) \cdot \cos(m\tau + m\lambda) \quad (3.2)$$

P_n^m are the associated Legendre functions (eg. p. 10 [Lambeck, 1988]). Due to the Earth's rotation the hour angle τ of the celestial body varies from 0 to 2π in 24 hours. Each term of the sum over m in Equation (3.2) has a certain spatial periodicity. The potential V therefore has a long period term connected to zonal harmonics P_n^0 ($m = 0$), a diurnal term connected to tesseral harmonics P_n^1 ($n > m$) and a semi-diurnal term connected to sectorial harmonics P_2^2 ($m = n = 2$). The variations of the distributions of the masses at the surface obeying the zonal distribution change the large polar moment of inertia C , whereas those obeying the tesseral distribution cause the position of the pole of inertia to change. The latter effect is as we see below essential for exciting the wobble. Sectorial distribution implies neither the first nor the second effect. Since R/r is about $1/60$ for the Moon and about $1/23000$ for the Sun, for large n terms of higher order m are negligible. For a first approximation it is justifiable to terminate the series expansion at $n = 2$ with V_2 comprising 98% of V . At the surface of the Earth the tidal forces exerted by the Moon dominate the ones of the Sun, since as can be seen in Equation (3.2) the larger solar mass is compensated by the smaller reciprocal distance Earth-Sun compared to the distance Earth-Moon. The maximum tidal acceleration due to the Moon, the Sun and Venus (which has the strongest effect of the planets) are: $1.37 \cdot 10^{-6} \text{ m/s}^2$, $0.50 \cdot 10^{-6} \text{ m/s}^2$ and $5.88 \cdot 10^{-11} \text{ m/s}^2$ respectively at the surface of the Earth [Wenzel, 1997]. In

Fig. 3.1 an example of the *Tamura* [1987] theoretic tidal potential (details see next section) for the location of BFO is shown. The contributions of different periods to the tidal potential can even be distinguished in the time domain. Prominent are the diurnal and semi-diurnal waves which are modulated by the long period fortnightly and semi-annual waves.

Thus far only the driving forces were described. To determine the response of the Earth to the forcing potential a description of the Earth's mechanical properties is needed. The basic relations of elastic deformation in classical continuum mechanics serve for this purpose (Equations 3.3 – 3.6). The first equation relates the linear momentum of a volume element of density ρ and velocity \mathbf{v} to the applied forces.

$$\rho \frac{d\mathbf{v}}{dt} = \mathbf{F} + \nabla \cdot \mathbf{S} \quad (3.3)$$

with the volume force $\mathbf{F} = \nabla V$ and a surface force or stress tensor \mathbf{S} and where d/dt denotes the time derivative. The generalization of Hooke's law for a linear isotropic elastic body is the following linear relation between stress \mathbf{S}_{ij} and strain $\boldsymbol{\varepsilon}_{ij}$:

$$\mathbf{S}_{ij} = \lambda D \delta_{ij} + 2\mu \boldsymbol{\varepsilon}_{ij} \quad (3.4)$$

with the cubic dilatation D , the shear and bulk modulus, μ and K and the Lamé constant $\lambda = K - 2\mu/3$ and the Kronecker symbol δ_{ij} . The next equation gives the relation between strain $\boldsymbol{\varepsilon}_{ij}$ and displacement u_i .

$$\boldsymbol{\varepsilon}_{ij} = \frac{1}{2} \left(\frac{\partial u_i}{\partial x_j} + \frac{\partial u_j}{\partial x_i} \right) \quad (3.5)$$

where $\frac{\partial}{\partial x}$ denotes the spatial derivative in cartesian coordinates. Additionally the equation of continuity must hold:

$$\frac{\partial \rho}{\partial t} + \nabla \cdot (\rho \mathbf{v}) = 0 \quad (3.6)$$

Under the assumption of small tidal deformations and subject to appropriate boundary conditions the gravitoelastic problem given in Equations 3.3 – 3.6 can be solved with perturbation theory. In spherical coordinates the solutions at the surface for a spherical, non-rotating, elastic, isotropic earth model (SNREI) with the forcing tidal volume potential V_2 are [eg. *Zürn and Wilhelm, 1984*]

$$u_r = h_2(\theta, \lambda) \frac{V_2(\theta, \lambda, t)}{g} \quad (3.7)$$

$$u_t = l_2(\theta, \lambda) \frac{1}{g} \frac{\partial V_2(\theta, \lambda, t)}{\partial \theta} \quad (3.8)$$

$$V' = k_2(\theta, \lambda) V_2(\theta, \lambda, t) \quad (3.9)$$

with the radial displacement u_r , the tangential displacement u_t and the potential V' due to the tidal redistribution of mass. g denotes the gravity acceleration at the

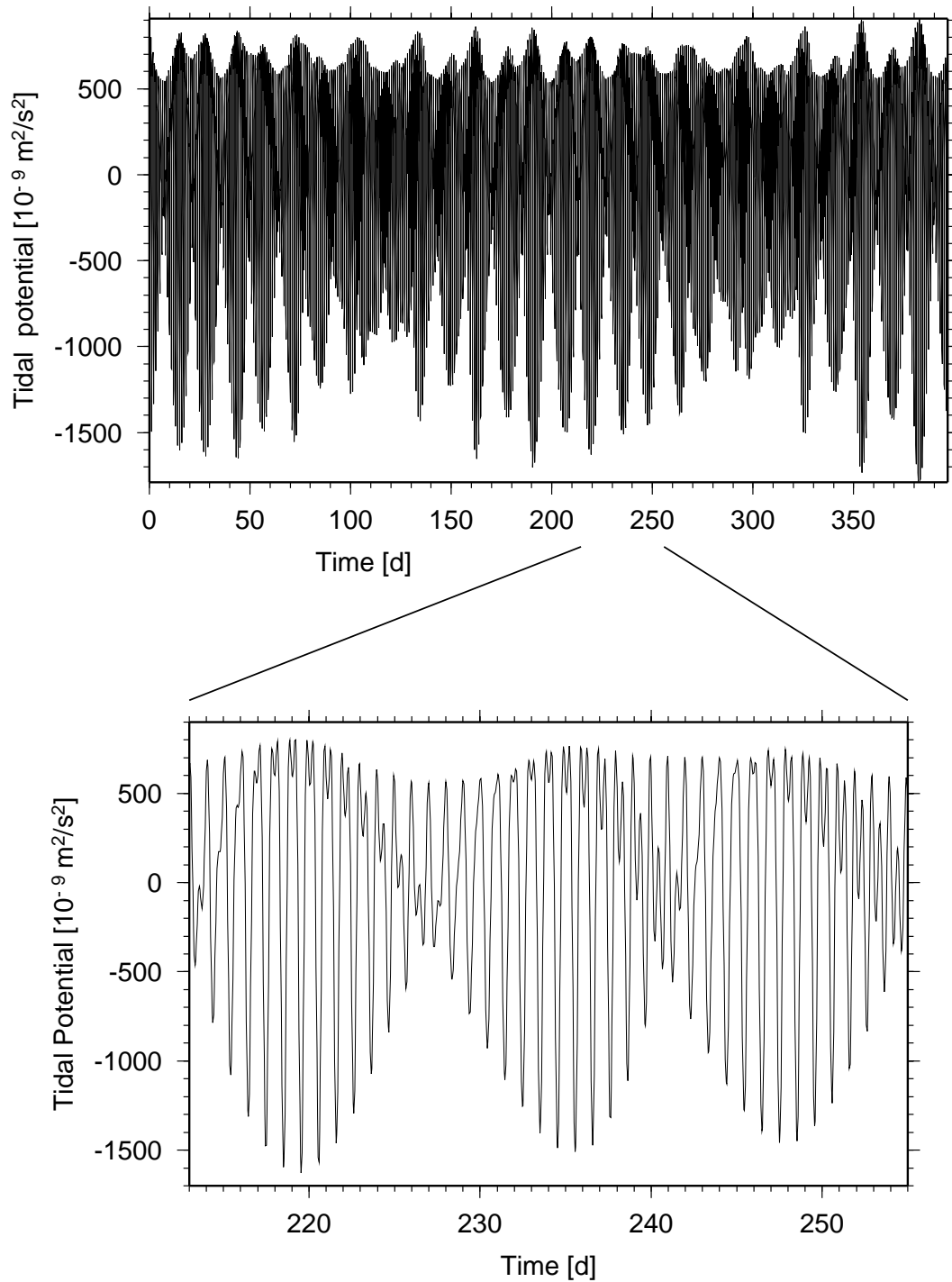


Figure 3.1: Time series synthesized by Tamura's theoretic tidal potential development (next section) for the location of the station BFO in different temporal resolution. The time series in the upper panel starting at November 23, 1988 is dominated by the fortnightly waves which are semi-annually modulated. Below a period of 42 days is extracted. Here besides the fortnightly tidal constituent the semi-diurnal and diurnal tides are resolved.

Earth's surface. The proportionality factors between the solutions of the gravito-elastic problem and the exciting potential of degree n (here $n = 2$) are the so-called Love numbers h_n, k_n and l_n . (l_n is also designated as Shida number). Alternatively expressed this means: The Love number h_n gives the ratio of the vertical displacement to the uplift of the equipotential surface due to the potential V_n , whereas k_n describes the ratio of the potential due to the tidal redistribution of mass and the forcing tidal potential and finally l_n is the ratio of angles defined by the tidal horizontal displacement relative to the radial distance r and the horizontal component of the forcing field relative to gravity $g(r)$. For the spherically symmetric Earth model PREM and low degree potentials the respective Love numbers amount to [Wang, 1997]

n	h_n	k_n	l_n
2	0.6032	0.2980	0.0839
3	0.2879	0.0920	0.0147
4	0.1750	0.0414	0.0102

Because of the linearity of the Earth's response the potential and the deformation possess the same temporal dependence. For a SNREI earth model the forcing and the response depend both on the same spherical harmonics P_n^m . So far only the volume forces due to the so-called body-tide were discussed. But normal and shear forces on the surface also induce deformations. For example ocean and ice load exert normal forces to the crust. At the CMB pressure is exerted due to the core rotation around an axis slightly different from the rotation axis (this is due to inertial coupling which will be discussed in detail in the next chapter). The corresponding Love numbers are the load Love numbers h', k', l' and the internal pressure Love numbers ${}^c h', {}^c k'$ and ${}^c l'$. The sources of shear deformation on the Earth's surface can be electromagnetic coupling forces or horizontal frictional forces arising from winds and ocean currents. The shear love numbers h'', k'', l'' which are also known as traction coefficients are found in *Wilhelm* [1986].

Each deformational effect on the surface of the Earth can be expressed as a linear combination of Love numbers [eg. *Wang*, 1997]. This is done below for the observables investigated in this work on the basis of a SNREI Earth model. The tidal variation in gravity at the surface of the Earth measured with a gravimeter is given by

$$\Delta g = -\delta \frac{\partial}{\partial r} V \quad (3.10)$$

with a dimensionless amplitude factor, the so called gravimetric or δ -factor

$$\delta = 1 + h - \frac{3}{2} k. \quad (3.11)$$

This δ -factor is the ratio of tidal gravity variations on an elastic Earth relative to those on a rigid Earth. The first term of δ (the one which equals 1) represents the difference between gravitational attraction of the gravimeter mass by the celestial

bodies and orbital acceleration. This term contains no information about the elastic properties of the Earth, it is an effect of the tide-generating forces. Only the second and the third term contribute to the Earth's response. The second term h describes the variation in gravity due to the radial displacement of the gravimeter in the undisturbed gravity field of the Earth (the free air effect). The variation of gravity due to mass redistribution is given by the third term.

Tilt and strain both are measures of deformation, though tilt includes terms arising from changes in local local accelerations as well. Tilts are defined as deflections of the crust with respect to the local vertical. A horizontal acceleration \ddot{x} causes an apparent tilt $\Delta = \ddot{x}/g$. Δ_N und Δ_E are southward and eastward tilt angles of the surface due to the horizontal tidal accelerations for a SNREI earth model:

$$\Delta_S = \eta \frac{1}{gR} \frac{\partial}{\partial \theta} V \quad (3.12)$$

$$\Delta_E = \eta \frac{1}{gR \sin \theta} \frac{\partial}{\partial \lambda} V \quad (3.13)$$

For a SNREI earth model the ratio of tidal tilt variations on an elastic Earth relative to those on a rigid Earth is called amplitude factor η (in the literature often denoted by γ) or tilt diminishing factor. Its representation in Love numbers is:

$$\eta = 1 - h + k \quad (3.14)$$

The contributions to η are analogous to the gravimetric factor, only the second and third terms of η are contributions from the response of the elastic Earth.

Tidal effects also incorporate strains within the crust. Linear strain is defined as the ratio $\Delta L/L_0$, where ΔL is the total change in baseline length and L_0 is the unperturbed length. Strain has second order tensor properties. At the stressfree surface of the Earth there exist three independent components of the strain tensor. These can be expressed through the normal components in north-south and east-west direction, ε_{NS} and ε_{EW} , as well as the horizontal shear strain ε_{SE} . The linear strain observed under an azimuth angle ξ (measured from north to east) can then be determined by:

$$\frac{\Delta L}{L_0}(\xi) = \varepsilon_{NS} \cos^2 \xi + \varepsilon_{EW} \sin^2 \xi - \varepsilon_{SE} \sin \xi \cos \xi \quad (3.15)$$

The relation between the tidal forcing and the response in strain is for a SNREI earth model given by:

$$\varepsilon_{NS} = \frac{1}{gR} \left(hV + l \frac{\partial^2 V}{\partial \theta^2} \right) \quad (3.16)$$

$$\varepsilon_{EW} = \frac{1}{gR} \left[hV + \frac{l}{\sin \theta} \left(\cos \theta \frac{\partial V}{\partial \theta} + \frac{1}{\sin \theta} \frac{\partial^2 V}{\partial \lambda^2} \right) \right] \quad (3.17)$$

$$\varepsilon_{NE} = \frac{l}{gR} \frac{\partial^2}{\partial \theta \partial \lambda} \left(\frac{V}{\sin \theta} \right) \quad (3.18)$$

Also the linear strain can be expressed in Love numbers

$$\frac{\Delta L}{L_0}(\xi) = f_1(\xi, \theta) h + f_2(\xi, \theta) l \quad (3.19)$$

where f_1 and f_2 are functions of the azimuth ξ of the strain direction and the co-latitude θ [Zürn and Wilhelm, 1984].

Substituting the Love numbers h and k into Equation 3.11 and 3.14 reveals that only a small fraction of the observed gravity and tilt signal describes the response of the elastic Earth. Actually the contribution of the deformable Earth in the δ -factor is only 0.16 respectively 0.30 in the tilt factor:

$$\delta = 1 + 0.16 = 1.16 \quad (3.20)$$

$$\eta = 1 - 0.30 = 0.70 \quad (3.21)$$

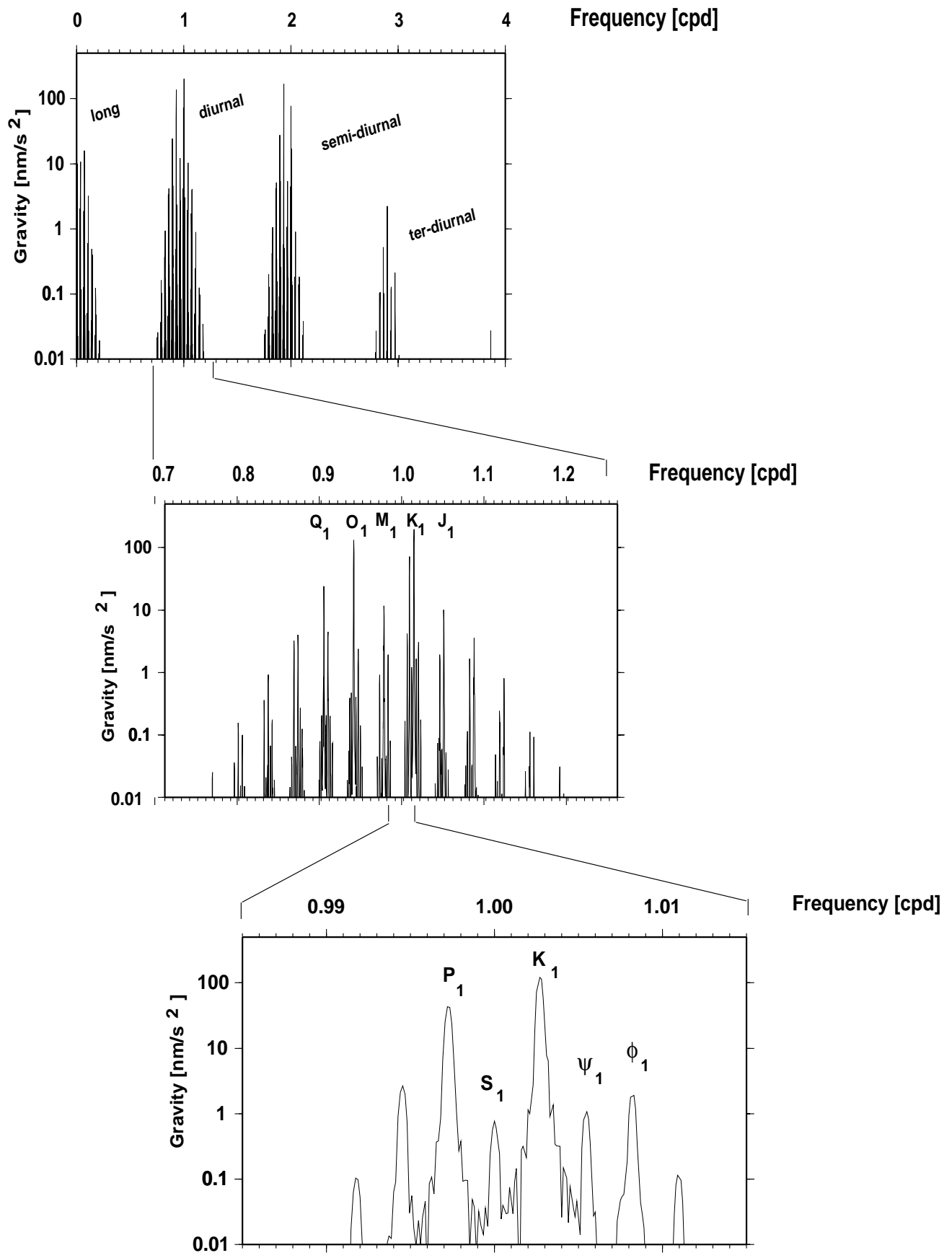
However, since on a rigid Earth there would be no deformation, the observed strain signal is to 100 % the response of the Earth.

Gravity tides are hardly influenced by local effects due to cavities, topography and geological structure. Strain and tilt tides on the other hand are strongly affected by these types of inhomogeneities near the observation site [Harrison, 1985]. Cavities like mines and tunnels in which instruments are often installed modify the local strain field and cause local strain induced tilts which can be of a similar order to tidal tilts. These cavity effects depend on the strain tensor components and provided that they are not frequency dependent they should not affect this work, since only differential signals are used for the NDFW analysis [Neuberg and Zürn, 1986].

Even a simple earth model with elastic mantle, fluid core and an elliptical boundary (as the only deviation from a SNREI model) between them leads to a frequency dependence in the Love numbers. This effect, the core resonance is the subject of this work and will be introduced theoretically in the next chapter. In Fig. 3.2 the theoretical tidal gravity variations at the location of BFO for an earth model as described in the next section are shown. The frequency range is zoomed gradually to expose the tidal constituents relevant for the core resonance.

3.2 Tidal Analysis

Tidal analyses were performed with the earth tide analysis program ETERNA, versions 3.0 up to 3.3 [Wenzel, 1994b; Wenzel, 1994c, Wenzel, 1996]. In the following the options set in ETERNA are described. As tidal potentials the Tamura [1987] model with 1200 waves and the HW95 [Hartmann and Wenzel, 1995] model with 12935 constituents were chosen. In the Tamura potential the tide-generating forces up to degree 4 for the Moon, degree 3 for the Sun and degree 2 for the planets Venus and Jupiter are considered, whereas the HW95 potential (available in ETERNA version 3.3) additionally takes into account the effects of higher orders for Moon, Sun



Previous page:

Figure 3.2: Spectra of theoretical gravity tides due to the forcing tidal potential shown in Fig. 3.1 with an extended series length of thirteen years. Upper panel: The contributions of the diurnal and semi-diurnal band to the spectrum are prominent. Middle panel: The diurnal band with the largest wave groups indicated. Lower panel: highly resolved tidal constituents relevant for the core resonance analysis.

and direct effects of the planets Mars, Mercury and Saturn. A series expansion up to degree $n = 6$ for the Moon, degree $n = 3$ for the Sun and degree $n = 2$ for the planets leads to an accuracy of $1.4 \cdot 10^{-12} \text{ ms}^{-2}$ rms in the time domain in comparison to a benchmark series. With ETERNA version 3.2 corrections for the body tide arising due to latitude variations in connection with polar motion are introduced. Also measures against the variable length of day are taken in this programme version. Within the error bars no significant differences between the results for the two potential developments in the period range relevant in this work are found. Therefore usually the Tamura potential is used for reasons of reduced computing time. The underlying earth model is the PREM model [Dziewonski and Anderson, 1981] with fluid outer core and inelastic mantle. The Love numbers belong to an oceanless, elliptical and uniformly rotating Earth.

To eliminate the drift and long period waves which are of no concern here, a high-pass filter without phase shift, the ETERNA filter No. 6 with a filter cut-off frequency of 0.8 cpd (half power point), was applied to the data. The spectra of the gravity, strain and air pressure observations treated in this way can be found in Appendix B. Simultaneously to the amplitudes and phases of a theoretical tidal model, the local air pressure was fit to the filtered data by a least squares method. The frequencies of the constituents are determined with high accuracy from astronomical observations and therefore they are treated in this inversion as constants. The results of the ETERNA analyses for all three data sets are shown in Table 3.1. As reference signals for gravity, tilt and strain have served the vertical and horizontal accelerations on a rigid Earth and the linear deformations on the PREM model respectively. The gravity results for the largest constituent in the semi-diurnal band, the tide M_2 correspond to older values determined for the location of BFO [Neuberg, 1987].

To show the improvement of the data quality we compared residuals of old analog [eg. Neuberg, 1987] and our new digital data after the tidal analysis with air pressure as an additional input channel. In Fig. 3.3 histograms of these residuals are depicted. The histogram-bin width depends on the amplitude of the largest residual. In the underlying ETERNA analyses the same filters and wave group partitioning as in the former HYCON analysis [Schüller, 1986] of analog data were used. The gravity residuals (standard deviation with the HYCON filter applied: 0.873 nm/s^2) show the most impressive improvement with a variance reduction of 97.5 %.

In comparison the well known, excellent data set from the Bad Homburg super-

Table 3.1: Observed amplitudes $|\tilde{D}|$, δ -factors and tilt diminishing factors (relative to the theoretical amplitude on a rigid earth), amplitude factors for strain (relative to the Wahr–Dehant Model [*Wahr, 1981; Dehant, 1987*]), phase leads κ with respect to the theoretical signal and the uncertainties σ_δ (estimation from SNR) of the ETERNA (version 3.0) tidal analysis of BFO digital data. Additionally the standard deviation (Stdv) of the residuals and the air pressure admittance factor determined by ETERNA are given.

Gravity	Wave	$ \tilde{D} [nm/s^2]$	δ -Factor	$\kappa [^\circ]$	σ_δ
	O ₁	353.8	1.14631	0.0564	0.00019
	P ₁	164.8	1.14756	0.2274	0.00041
	S ₁	4.3	1.26349	8.3113	0.01747
	K ₁	492.4	1.13442	0.2461	0.00013
	ψ_1	4.4	1.30456	-2.1076	0.01747
	ϕ_1	7.1	1.15273	0.2334	0.00959
	M ₂	393.3	1.18404	2.0090	0.00009
Stdv: $0.807 nm/s^2$ Air pressure admittance $\nu = -3.209 nm/s^2/hPa$					
Strain	Wave	$ \tilde{D} [10^{-9}]$	Amp-Factor	$\kappa [^\circ]$	σ_δ
	O ₁	6.328	0.97757	-4.1936	0.00319
	P ₁	2.830	0.93963	-4.9979	0.00686
	S ₁	0.130	1.82452	-50.5376	0.29037
	K ₁	7.349	0.80731	-7.1694	0.00227
	ψ_1	0.171	2.40561	14.7206	0.29038
	ϕ_1	0.173	1.33377	-0.1074	0.15956
	M ₂	6.963	1.25410	7.8668	0.00139
Stdv: $0.301 n\varepsilon$ Air pressure admittance: $\nu = -0.813 n\varepsilon/hPa$					
Tilt	Wave	$ \tilde{D} [nrad]$	Amp-Factor	$\kappa [^\circ]$	σ_δ
	O ₁	18.006	0.76334	-21.5181	0.00219
	P ₁	8.750	0.79741	-22.0880	0.00472
	S ₁	0.470	1.80443	-104.4383	0.19939
	K ₁	27.397	0.82591	-19.0252	0.00156
	ψ_1	0.238	0.90829	-57.4103	0.19940
	ϕ_1	0.389	0.82225	-31.3693	0.10956
	M ₂	40.482	0.79473	-15.6455	0.00044
Stdv: $0.799 nrad$ Air pressure admittance: $\nu = -1.732 nrad/hPa$					

conducting gravimeter [Zürn *et al.*, 1986] (Fig. 2.1) had a slightly larger standard deviation, namely $0.956 \text{ nm}/s^2$. The variance reduction for the strain data is 91.1 %. For the tilt data which show the smallest improvement, we still obtain a variance reduction of 88.7 %. In spite of the fact that at the frequency of O_1 the SNR of strain and tilt is only 1/20, respectively 1/17 of that of the gravity it makes sense to analyze the former signals too. The reason is that the response of the earth to the forcing tidal potential contributes only 14 % for gravity, but 43 % for tilt (Eq. 3.20 and 3.21) and 100 % for strain to the total tidal signal. These percentages describe the geophysical significance of the signal type. If we determine the product of this geophysical significance and the SNR of the data at the frequency of O_1 , we obtain for strain 36 %, and for tilt only 21 % of the gravity value. This product is a measure for the uncertainties of the resulting NDFW parameters. Therefore a priori higher uncertainties for the NDFW results of the tilt data than for the strain data are expected.

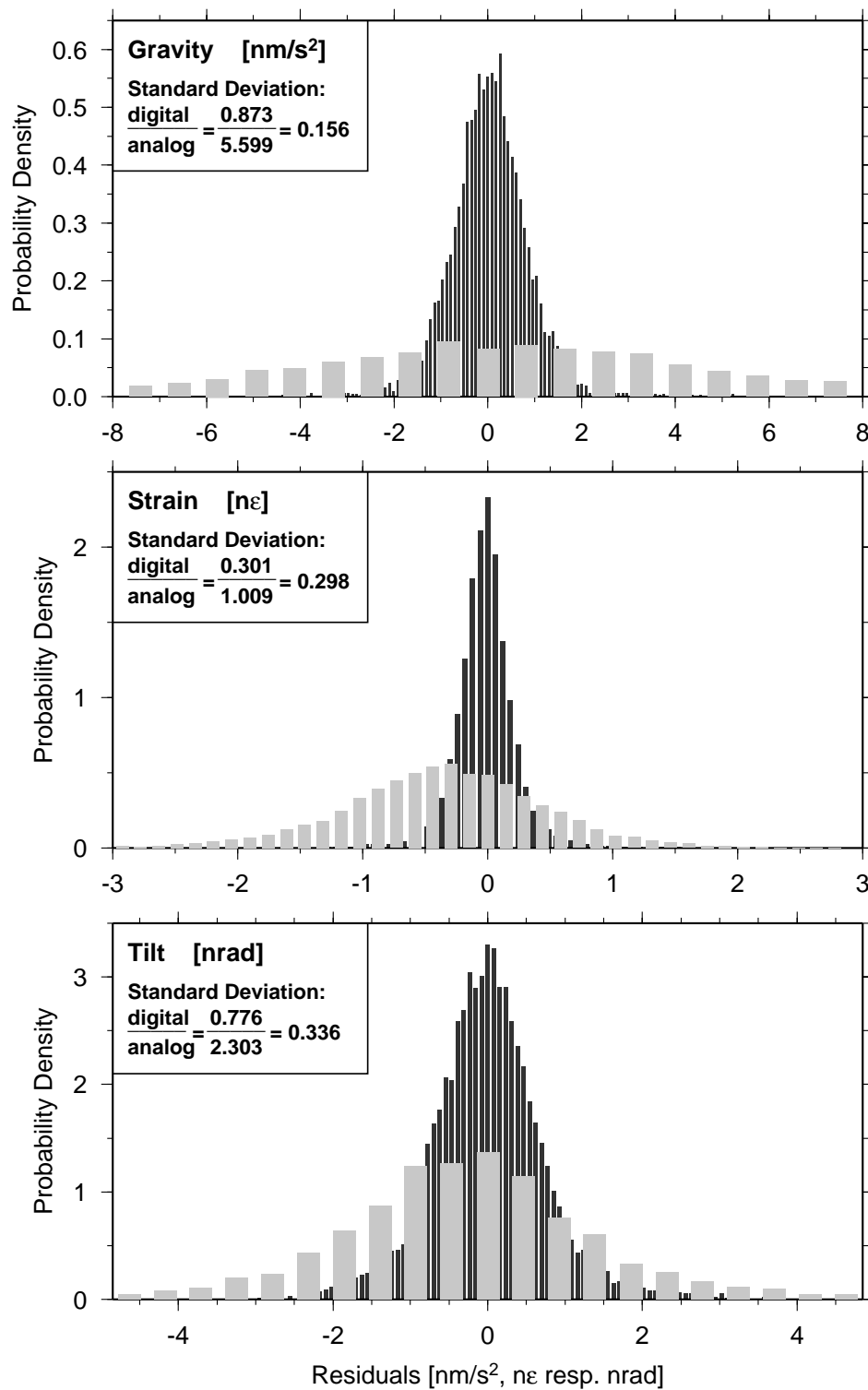


Figure 3.3: Residual histograms for gravity, strain and tilt. The light shaded bars represent the unexplained signal after tidal analysis of older analog data whereas the dark shaded bars belong to the digital data of this work. The bin width depends on the standard deviation of the residuals.

Chapter 4

Ocean and air pressure correction

Tidal forces not only act on the solid Earth but also on the world oceans and the surrounding atmosphere. In turn these two parts of the Earth affect the measurements of the solid earth tides. Whereas the response of the Earth are the quasi static body tides, the response of the oceans and the atmosphere is dynamic. The standard method to correct for their influences and to reduce the measurements to the body tide is, to fit the locally observed barometric pressure simultaneously with the theoretical tides in the tidal analysis. Afterwards the tidal admittances for individual tides are corrected with the help of ocean load computations. Both these corrections cannot be considered to be perfect.

4.1 Ocean load correction

The frequency dependent ocean effects on a gravimeter and tiltmeter consist of both the direct Newtonian attraction of the sensor mass and the effects of deformation of the Earth (free air effect and potential change) due to loading by the periodically shifting water masses. On the other hand horizontal strainmeters deployed on the ground do only register the deformations of the surface due to the loading.

To correct for the small but important influences of the world oceans the newest ocean load calculations from *Agnew* [1996] were applied. As input data for his new load model [*Agnew*, 1995] he used a combination of the new ocean tide model CSR 3.0 [*Eanes and Bettadpur*, 1995] and the purely hydrodynamical ocean tide model from *Le Provost et al.* [1994]. The latter model was obtained by finite–element modeling and includes many of the shelf areas. The CSR 3.0 model with a grid distance of $0.5^\circ \times 0.5^\circ$ is based upon TOPEX/POSEIDON altimeter data [*Le Provost et al.*, 1995] in the range of $66^\circ\text{N} - 66^\circ\text{S}$ (rectilinear grid in Fig. 4.1). For *Agnew's* new load model the loading Green functions (combining load Love numbers for spherical harmonics) of *Farrell* [1972] (Gutenberg–Bullen earth model) were convolved with the tide model described above using a station centered grid with a global grid

Table 4.1: Ocean signals \tilde{L} (relative to local potential; lead positive) of relevant constituents calculated by *Agnew* [1996] based on the Schwiderski and the CSR 3.0 ocean tide model for the location of BFO. Amplitudes are given in nm/s^2 (gravity), $n\varepsilon$ (strain) and $nrad$ (tilt), phases in degrees. The values in brackets are not provided by the models, but derived from the K_1 ocean signals by scaling with the amplitudes of the potential.

	Wave	Ocean Tide Model			
		Schwiderski		CSR 3.0	
		Amplitude	Phase	Amplitude	Phase
Gravity	O_1	1.40	171.0	1.517	179.65
	P_1	0.60	87.4	0.787	93.34
	K_1	1.50	68.4	2.287	86.28
	ψ_1	(0.01)	(68.4)	(0.017)	(86.28)
	ϕ_1	(0.02)	(68.4)	(0.032)	(86.28)
Strain	O_1	0.1002	50.40	0.1448	41.23
	P_1	0.0841	24.09	0.0883	16.39
	K_1	0.2524	23.28	0.2779	12.25
	ψ_1	(0.0019)	(23.28)	(0.0021)	(12.25)
	ϕ_1	(0.0036)	(23.28)	(0.0039)	(12.25)
Tilt	O_1	0.350	-146.9	0.3107	-146.69
	P_1	0.370	56.0	0.4515	51.57
	K_1	1.240	48.4	1.4431	44.44
	ψ_1	(0.049)	(48.4)	(0.0112)	(44.44)
	ϕ_1	(0.035)	(48.4)	(0.0205)	(44.44)

distance of $0.5^\circ \times 0.5^\circ$ (centered grid in Fig. 4.1). Since the mass-load Green's function has very large values in the vicinity of the point load the region near the station should be specially taken into account. Therefore a local grid with decreased cell size and interpolated ocean tide model data is used at distances less than 5° to the station. Cells with more than 50 % landmass are not taken into account.

In Table 4.1 the ocean load signals $\tilde{L}_{CSR3.0}$ based upon the CSR 3.0 tide model are compared to the ocean load signals $\tilde{L}_{Schwiderski}$ determined on the basis of the older *Schwiderski* [1980] tide model with a cell size of only $1^\circ \times 1^\circ$. For this tide model also the loading Green's functions of *Farrell* [1972] were used. In most cases the results agree to within better than 10 %. Only the gravity values for K_1 differ by more than 50 % in amplitude. However since the station BFO is located 456 km

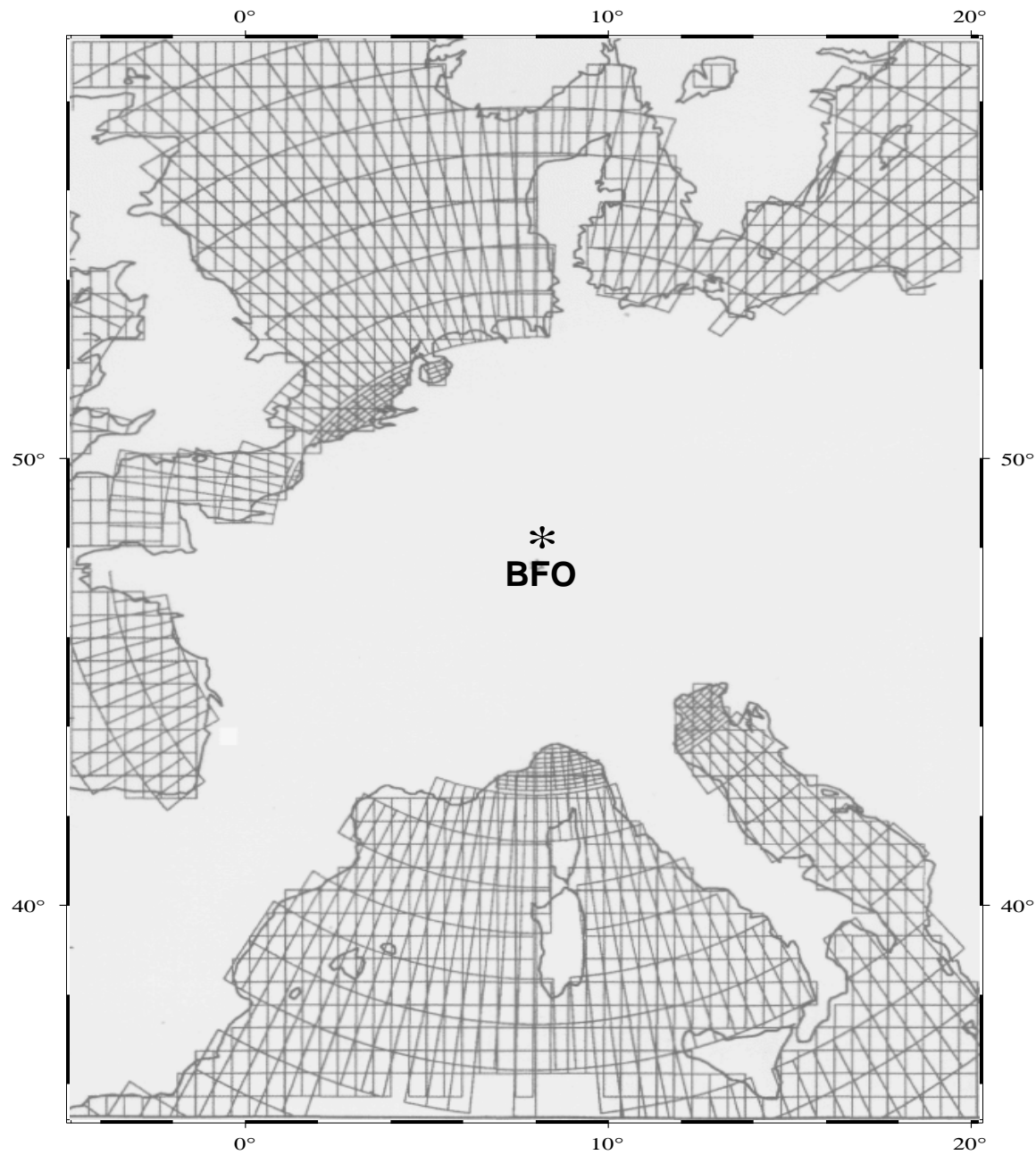


Figure 4.1: Sketch of the ocean model grids. The rectilinear grid represents the grid of the CSR 3.0 ocean tide model. The asterisk at the center marks the origin of the station-centered grid of the load calculations, i.e. the station BFO.

away from the sea the ocean signals amount only to several parts in hundred of the body tide (Table 3.1). The different ocean load calculations result in a difference in the NDFW period of less than 0.5%. (See also error estimation with Monte Carlo simulation, Chapter 7.3).

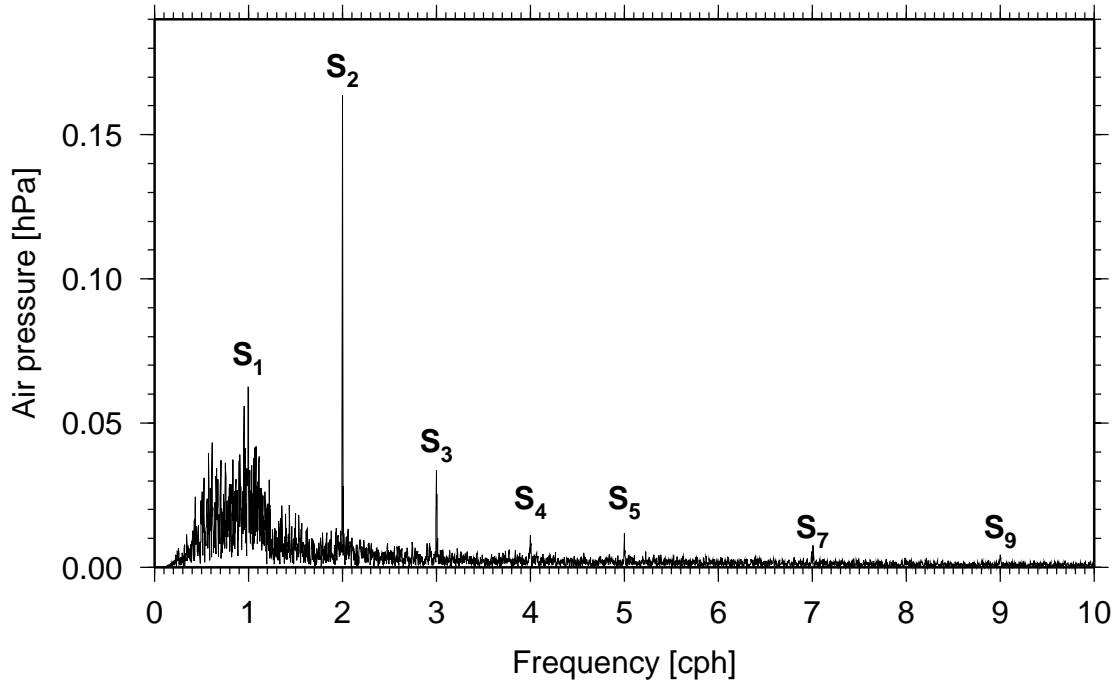


Figure 4.2: Spectrum of air pressure observations of about 13 month length at station BFO. Prominent are the sharp spectral lines due to the the daily heating of the earth surface and atmosphere. Whereas the harmonics of the solar day are a global phenomena, the broad-band underground is of local origin.

4.2 Air pressure correction

The gravitational reactions of the atmosphere to the tidal forces are rather small, but there are large tides in the atmosphere for solar constituents due to the radiational energy input from the Sun. The gravity, strain and tilt records are contaminated by broad-band noise of meteorological origin also due to density variations of air masses. Contributions to this noise are the direct attraction of the gravimeter mass by the changing air masses and the loading of the surface owing to atmospheric pressure changes. In the tidal analysis by ETERNA and all other least squares methods there is no difference being made between the broad-band noise and the solar harmonics (see air pressure spectrum Fig. 4.2). However, as *Warburton and Goodkind* [1977] have pointed out, the admittances of gravity with respect to atmospheric pressure are significantly different for the broad-band background on one hand and distinct solar harmonics on the other hand. One reason is the fact, that the background belongs to local effects whereas the solar harmonics in the atmosphere have large contributions from global wave phenomena [eg. *Volland*, 1988]. Recently other authors (see Chapter 8) have reconfirmed this admittance difference.

Several alternative methods have been developed to treat the barometric effects on

gravity recordings. *Crossley et al.* [1995] determine the admittance function between gravity and local air pressure in the frequency and time domain. They demonstrate again that the admittance for the solar harmonics is considerably different from the one for the broad-band meteorologic signal: for Cantley, Canada they found admittance factors of about $-1.7 \text{ nm/s}^2/\text{hPa}$ and $-2.3 \text{ nm/s}^2/\text{hPa}$ for the solar harmonics S_1 and S_3 , respectively, while their broad-band admittance is slowly rising with frequency and is about $-3.5 \text{ nm/s}^2/\text{hPa}$ in the vicinity of the diurnal tidal band. *Merriam* [1994] pointed out the importance of the seasonal modulations of the solar tides. Annual and semi-annual modulations of the thermal tide S_1 disturb the waves of P_1 , K_1 and π_1 , ψ_1 , respectively. The salient point is, that these tides except π_1 are used in the NDFW estimation.

Mukai et al. [1995] evaluated near station pressure effects on gravity by numerically integrating air masses. At the same time they took into account regional and global effects by spherical harmonic expansions of meteorological observations. All these efforts demonstrate how serious this problem is. Further below (Chapter 8) several experiments are described which have been performed to study this problem and its impact on NDFW analysis in more detail.

Chapter 5

Theoretical aspects of the wobble

Scientists of different fields use the term *nutaton* differently depending on their subject of investigation. In the classical sense of the word, a nutation is a nodding up and down motion of the figure axis of a rotating body. A physicist calls the motion of the figure axis of a rotating gyroscope around the vector of total angular momentum a nutation, no matter if an external torque is acting or not. If you want to describe the motion of eg. a spinning top in inertial space it is sensible to observe the figure axis. Astronomers denote as nutation the motion of the instantaneous rotation axis around the vector of total angular momentum caused by the varying components of the luni-solar tidal torque exerted on the Earth's equatorial bulge. This is because what they observe in the reference system of the fixed stars is the motion of the rotation axis of the Earth. Geophysicists observe a wobble on the Earth in a body-fixed reference system. They use the term nutation or *sway* [Chao, 1985] for the motion of the instantaneous rotation axis around the vector of total angular momentum that accompanies the wobble [Rochester *et al.*, 1974]. In this work the last definition is adopted.

5.1 A force free gyroscope

The theory of gyroscopes [Sommerfeld, 1964] provides the basic ideas for the description of the motions and deformations of the rotating elliptical Earth: the wobbles and the nutations. To understand the kinematic behavior of the Earth it is helpful to consider first a simple rigid gyroscope. Without external forcing for a so called free gyroscope the angular momentum must be conserved:

$$\frac{d \mathbf{H}}{dt} = \mathbf{0} \quad (5.1)$$

The total angular momentum \mathbf{H} is defined as the dot product of the tensor of inertia \mathbf{C} with the components C_{ij} (see Glossary) and the angular frequency $\boldsymbol{\omega}$:

$$\mathbf{H} = \mathbf{C} \cdot \boldsymbol{\omega} \quad (5.2)$$

The equilibrium (Equation 5.1) requires that the vector of total angular momentum stays fixed in space. Furthermore the kinetic energy T of the rotating body must remain constant:

$$2T = \boldsymbol{\omega} \cdot \mathbf{H} = \omega H \cos(\boldsymbol{\omega}, \mathbf{H}) = \text{const.} \quad (5.3)$$

The consequence is that the projection of $\boldsymbol{\omega}$ on \mathbf{H} is constant. This restriction only allows the $\boldsymbol{\omega}$ -vector to describe a cone around the vector of total angular momentum. Expressed otherwise the tip of the rotation vector of an axi-symmetric body traces a track in a plane perpendicular to the vector of total angular momentum. This plane is called invariable plane.

Substituting the angular momentum in Equation 5.1 for the implicit expression in Equation 5.3, the surface of an ellipsoid in the $\boldsymbol{\omega}$ -space is given by:

$$C_{11} \omega_1^2 + C_{22} \omega_2^2 + C_{33} \omega_3^2 + 2C_{12} \omega_1 \omega_2 + 2C_{13} \omega_1 \omega_3 + 2C_{23} \omega_2 \omega_3 = 2T \quad (5.4)$$

This energy ellipsoid is also called Poinsoot ellipsoid [eg. *Rochester et al.*, 1974]. Its principal axes are identical to those of the inertia ellipsoid (which represents the moments of inertia for arbitrary axes through the center of mass). The radii are different, they amount to $1/\sqrt{C_{ii}}$. For an axi-symmetric body the figure axis coincides with a principal axis of the Poinsoot ellipsoid. The surface of the Poinsoot ellipsoid then represents the area where the tip of the $\boldsymbol{\omega}$ -vector is restricted to move. This motion of the tip of the $\boldsymbol{\omega}$ -vector on the surface of the body-fixed Poinsoot ellipsoid on one hand and on the space-fixed invariable plane on the other hand is only compatible with the Poinsoot ellipsoid rolling on the invariable plane (see the Poinsoot representation in Fig. 5.1). Since the contact point of plane and ellipsoid is instantaneously in rest [*Greiner*, 1986], the rolling motion contains no slipping part. Drawing attention to the \mathbf{H} -vector, the $\boldsymbol{\omega}$ -vector and the figure axis it can be understood, that the rolling motion consists of the instantaneous rotation vector $\boldsymbol{\omega}$ describing one cone (body cone) around the figure axis and simultaneously a second cone (space cone) around the vector of total angular momentum (Fig. 5.2). For an oblate gyroscope which means an axi-symmetric body with $C_{33} > C_{11}$ this motion can be described by the body cone rolling inside the space cone without slipping. The body cone then represents the wobble and the space cone the nutation. At every moment the $\boldsymbol{\omega}$ -vector forms the contact line of the two cones. Equivalently expressed: the $\boldsymbol{\omega}$ -vector, the \mathbf{H} -vector and the figure axis are always coplanar. For an oblate gyroscope like the Earth the $\boldsymbol{\omega}$ -vector and the figure axis span a plane which slowly revolves around the vector of total angular momentum.

5.2 The Earth – a gyroscope

The theoretical fundamentals concerning the differential rotational motion of the Earth's core and mantle – namely the nearly diurnal wobble motion – shall be sketched in this section. Comprehensive treatment is found eg. in *Hinderer et al.* [1982]. The dynamical effects on a simple earth model can be obtained by taking

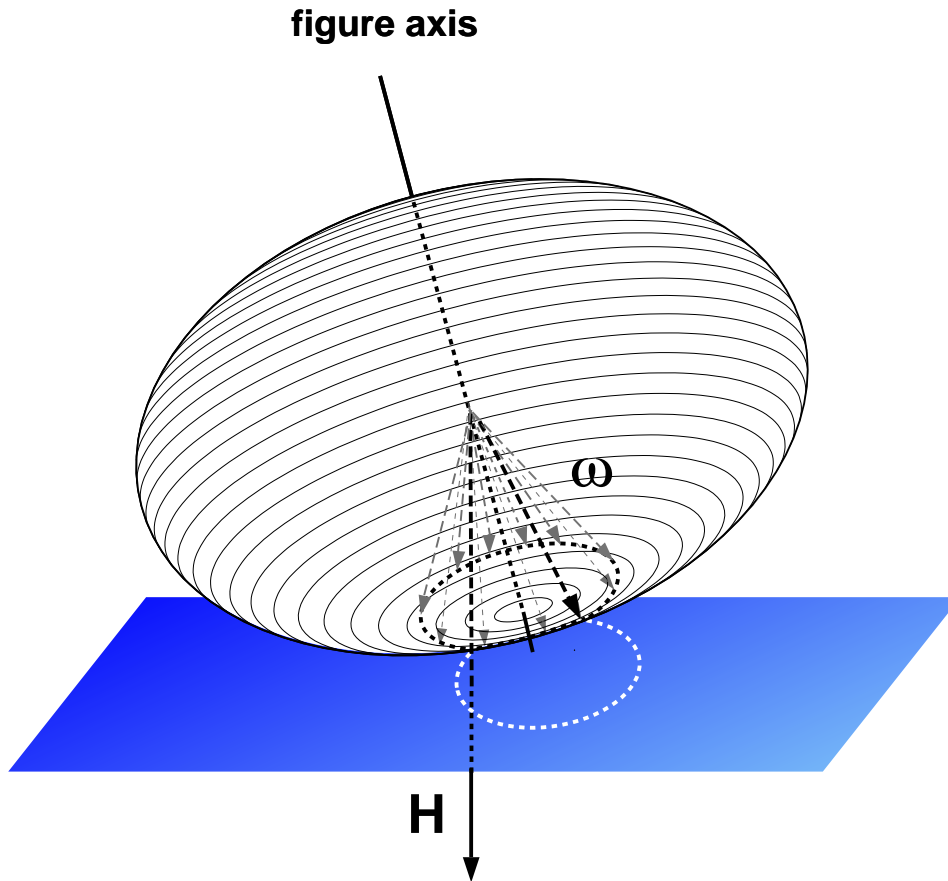


Figure 5.1: Poincaré representation [eg. *Sommerfeld*, 1964]: Poincaré ellipsoid of an oblate gyroscope rolling on the invariable plane. For an axi-symmetric body the tip of the ω -vector traces circles on both the Poincaré ellipsoid and the invariable plane. Additionally to the present rotation vector ω (in black color) its variation with time on the Poincaré ellipsoid is documented by the gray vectors (body cone).

into account the following conditions which are introduced in succession below. To the right of each arrow the consequence of the respective condition is listed:

- Balance of angular momentums for rotating rigid ellipsoid body → Euler wobble
- Elastic body → Time dependent quantities
- Small deviations → Perturbation theory can be applied
- 2-layer earth model → Separation of Liouville Equations
- Ellipsoid CMB and fluid core → Coupling torques between mantle and core → Additional eigenmode NDFW
- Coordinate transformation → Additional angular momentums vanish

The Euler equation describes the change of the angular momentum \mathbf{H} of a rigid body in the inertial system (index I), when the external torque \mathbf{L} is exerted on the

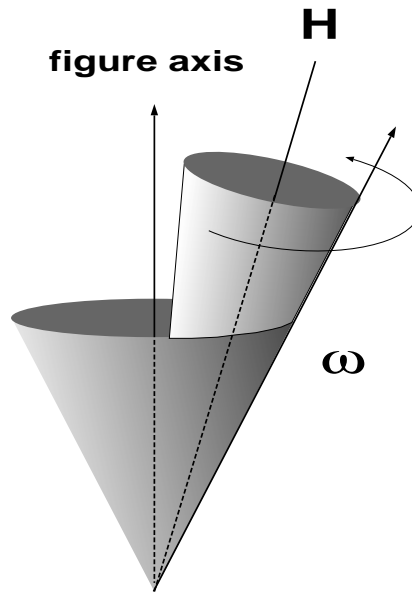


Figure 5.2: Body and space cones describing wobble and nutation of an oblate, homogeneous, axis-symmetric gyroscope. The angles of the cones represent the amplitudes of wobble and nutation.

body.

$$\dot{\mathbf{H}}_I = \mathbf{L} \quad (5.5)$$

Instead of considering a motion relative to an inertial system, it is often more convenient to express the motion relative to a system K , tied to the rotating body. If the system K is rotating with an angular frequency $\boldsymbol{\omega}$ relative to the inertial system I , then for a vector $\boldsymbol{\theta}$ the operator identity

$$\left(\frac{d\boldsymbol{\theta}}{dt}\right)_I = \left(\frac{d\boldsymbol{\theta}}{dt}\right)_K + \boldsymbol{\omega} \times \boldsymbol{\theta} \quad (5.6)$$

is valid. The Euler equation then becomes:

$$\dot{\mathbf{H}} + \boldsymbol{\omega} \times \mathbf{H} = \mathbf{L} \quad (5.7)$$

Solving this equation of motion for a homogeneous, axis-symmetric, rigid body results in a rotational eigenmode, the Eulerian wobble. If a body with elastic or anelastic rheology instead of a rigid one is considered, it has to be taken into account that each individual particle is accelerated relative to the body fixed system K . This causes the additional angular momenta \mathbf{h} . The total angular momentum of a deformable body is then given by:

$$\mathbf{H}(t) = \mathbf{C}(t) \cdot \boldsymbol{\omega}(t) + \mathbf{h}(t) \quad (5.8)$$

[*Munk and MacDonald, 1960*]. All quantities in this equation are time dependent. Substituting this expression for the total angular momentum \mathbf{H} in Equation 5.7

leads to the Liouville equation of motion

$$\frac{d}{dt}[\mathbf{C} \cdot \boldsymbol{\omega} + \mathbf{h}] + \boldsymbol{\omega} \times [\mathbf{C} \cdot \boldsymbol{\omega} + \mathbf{h}] = \mathbf{L} \quad (5.9)$$

If the deviations from the rigid Earth are small, then perturbation theory can be applied and so it is possible to linearize the equation of motion. Every property of the rigid Earth shall then be represented by a variable $\boldsymbol{\theta}_0$ and all time varying (elastic) terms are concentrated in the perturbation term $\Delta\boldsymbol{\theta}(t)$. Then for every variable of Equation 5.9 we can write:

$$\boldsymbol{\theta}(t) = \boldsymbol{\theta}_0 + \Delta\boldsymbol{\theta}(t) \quad (5.10)$$

with $\Delta\boldsymbol{\theta}(t) \ll \boldsymbol{\theta}_0$. For reasons of convenience the axes of the body-fixed coordinate system are chosen to be parallel to the principal axes of inertia. Then the time-dependent inertia tensor \mathbf{C} of the entire Earth relative to $\boldsymbol{\omega}$ is defined by

$$\mathbf{C} = \begin{bmatrix} A + c_{11} & c_{12} & c_{13} \\ c_{21} & A + c_{22} & c_{23} \\ c_{32} & c_{32} & C + c_{33} \end{bmatrix} \quad (5.11)$$

A and C being the equatorial, respectively polar moments of inertia of the undeformed Earth. Due to the elastic deformation of the mantle the time-varying perturbation terms c_{ij} are induced with $\{i, j\} = 1, \dots, 3$. The earth rotation vector $\boldsymbol{\omega}$ consists of the constant diurnal rotation of the figure axis with angular frequency Ω (with respect to the fixed star system) and much smaller deviations from it, namely ω_1 , ω_2 and ω_3 :

$$\boldsymbol{\omega} = \begin{bmatrix} \omega_1 \\ \omega_2 \\ \Omega + \omega_3 \end{bmatrix} \quad (5.12)$$

The equatorial components ω_1 and ω_2 point into the direction of the Greenwich meridian, respectively in a direction perpendicular to it (90° farther east). These components become finite for the rotational eigenmodes of the Earth (eg. the Eulerian wobble for a homogenous body) and are therefore of interest in this work. On the other hand the polar component of the rotation vector $\Omega + \omega_3$ is parallel to the figure axis and has therefore no effect on the wobble (see Figure 5.2). The polar term $2\pi/(\Omega + \omega_3)$ describes only the varying length of day (LOD), which is of no concern here.

In the next step an earth model with characteristics essential for differential rotation between mantle and core is introduced: a fluid core confined in an elliptical cavity given by the mantle¹. The differential rotation gives rise to a second rotational eigenmode, the nearly diurnal free wobble. The Liouville equation (5.9) can then be separated in one equation concerning the core (index C) and another one describing

¹The mantle is quasi the container of the fluid core.

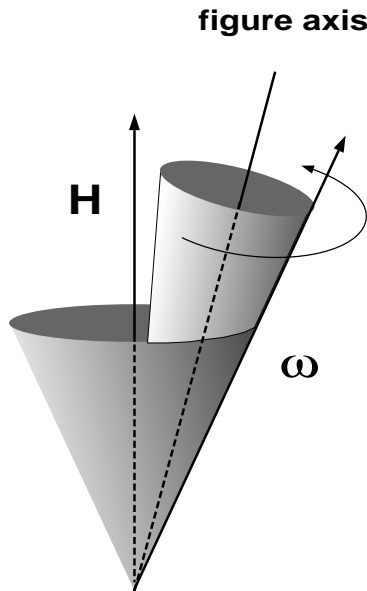


Figure 5.3: Body and space cones describing wobble and nutation of a fluid core confined in an elliptical cavity. The angles of the cones represent the amplitudes of wobble and nutation.

the mantle (index M):

$$\frac{d}{dt} [\mathbf{C}^C \cdot \boldsymbol{\omega} + \mathbf{h}^C] + \boldsymbol{\omega} \times [\mathbf{C}^C \cdot \boldsymbol{\omega} + \mathbf{h}^C] = \mathbf{L}^C + \mathbf{N} \quad (5.13)$$

$$\frac{d}{dt} [\mathbf{C}^M \cdot \boldsymbol{\omega} + \mathbf{h}^M] + \boldsymbol{\omega} \times [\mathbf{C}^M \cdot \boldsymbol{\omega} + \mathbf{h}^M] = \mathbf{L}^M - \mathbf{N} \quad (5.14)$$

(All variables except the rotation vector $\boldsymbol{\omega}$ and the coupling torque \mathbf{N} appear in the equations separately for the mantle and the core.) The moments of inertia must be defined individually for these two parts according to Equation 5.11. The coordinate system K can be fixed to the mantle in such a manner that the additional angular momentum \mathbf{h}^M vanish. The corresponding axes are known as Tisserand axes [*Hinderer et. al*, 1982].

Since core and mantle respond differently to the luni-solar force, there exists a differential rotation between mantle and core. If the CMB would be spherical and no coupling between core and mantle would exist, the motion of the core and mantle would be independent of each other. Then no resonant deformation of the CMB and no differential rotation of the mantle and core would take place. The coupling between mantle and core is represented by the torque \mathbf{N} . This variable can comprise torques of topographic, electromagnetic, viscous, gravitational and inertial origin. Considering the complete Earth, the coupling torques must vanish (Equation 5.9). In the following the influence of the different coupling mechanisms are discussed (see also Fig. 1.3). Topography of the CMB is not included in the calculation, since it has not been determined with significance so far [*Doornbos and Hilton*, 1989]. Only the diurnal tesseral components in the tidal potential V of the moon and sun contribute

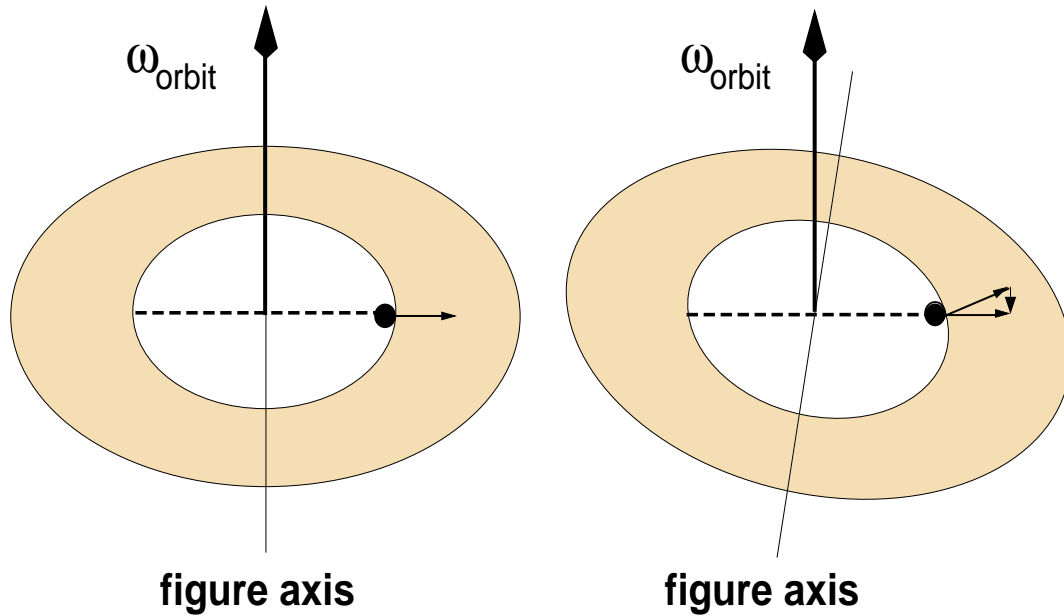


Figure 5.4: Left panel: in the unperturbed state all axes are parallel. Right panel: a torque has misaligned the figure axis of the container and the orbital rotation axis ω_{orbit} . The small arrows represent the force on the mantle exerted by the particle which orbits in the dashed plane.

to the *gravitational* torques exerted at the CMB. Turbulence and convection in the core are neglected. The appreciable part of the mutual influence between mantle and core is supposed to be due to inertial coupling. A simple model of inertial coupling transmitted via pressure is discussed eg. in *Toomre* [1974]:

Consider a frictionless particle sliding around an oblate ellipsoidal cavity free of gravity, initially following the equatorial plane. When the axis of the cavity is turned through a small angle the particle continues to orbit in the original plane, but as it is now inclined to the equator of the cavity the orbit has become slightly elliptical. Moreover, the cavity wall is no longer everywhere perpendicular to the plane of the orbit and since the particle is frictionless it only experiences a force normal to the cavity wall. This force has a component perpendicular to the plane of the orbit (see small vectors in Fig. 5.4). These forces set up at the cavity wall try to realign the figure axis of the cavity with the rotation vector of the particle. The result is a torque that causes the orbit to precess in a retrograde sense about the equator of the cavity.

This mechanism is a simplified analogue of the response of the fluid core motion to a change in orientation of the axis of the CMB. When the figure axis of the mantle and instantaneous rotation axis of the core become misaligned which is possible due to the tesseral tidal forcing then the mantle tries to impose its shape on the core. Restoring pressure torques arise at the CMB which try to realign the two

axes. The Earth reacts as a gyroscope with a wobble in the earth-fixed system and the associated nutation in the inertial system (5.3). The important simplification in this model of inertial coupling is neglect of the internal motion in the core² that is required to accommodate its shape to an ellipsoidal cavity misaligned with its own rotational axis. With the help of the Love number formalism the reaction of the CMB (changes in the inertia tensor) to the instantaneous elastic deformation is considered. Inertial coupling is non-dissipative. But viscous and electromagnetic coupling caused by tangential forces at the CMB do have a dissipative component. It is convenient to use only one parameter set to describe those totally different physical phenomena. The dissipative and the frictionless coupling coefficient K and K' describe viscous and electromagnetic effects. Their influence depends on the conductivity of the lower mantle, the radial component of the Earth's magnetic field, the constant of induction and the viscosity of the outer core. These effects are rather small.

The polar component of the rotation vector is decoupled in the equations and therefore is not relevant for rotational eigenmodes. Substituting the respective expressions of the moments of inertia, angular momentums and torques into Equations 5.9 and 5.13 the differential equation system for the equatorial components of the rotation vector for the whole Earth³ $\omega = \omega_1 + i \omega_2$ and the core $\omega^C = \omega_1^C + i \omega_2^C$ becomes [*Hinderer et al.*, 1982]:

$$\begin{aligned} \dot{\omega} \left(1 + \alpha \frac{k}{k_s} \right) - i\Omega\omega\alpha \left(1 - \frac{k}{k_s} \right) \\ + \left(\dot{\omega}^C + i\Omega\omega^C \right) \left(\frac{A^C}{A} - \frac{\alpha k'}{k_s} \right) = \frac{3\alpha k}{k_s R^2} \left(\dot{V} + iV \right) - \frac{3i\alpha V}{R^2} \end{aligned} \quad (5.15)$$

$$\begin{aligned} \dot{\omega} \left(1 + \frac{q_0 h^C}{2} \right) + \dot{\omega}^C \left(1 - \frac{q_0 {}^C h'}{2} \right) \\ + i\Omega\omega^C \left(1 + \alpha^C + K' - iK \right) = \frac{3q_0 h^C}{2R^2} \frac{\dot{V}}{\Omega} \end{aligned} \quad (5.16)$$

with the earth radius R . The Love numbers k and k_s describe the variation of potential due to perturbations at the actual frequency and infinitely slowly (secular). h^C and k' are Love numbers which describe the static deformation of the Earth exerted to body and normal forces (Chapter 3). The Love number ${}^C h'$ describes the reaction of the CMB-shape to the pressure field of the Poincaré flow. By $q_0 = \Omega^2 R/g$ the ratio of centrifugal force and gravity at the equator on the surface of the Earth is expressed. α and $\alpha^C = (C^C - A^C)/C^C$ denote the dynamical ellipticity of the whole Earth, respectively of the core. The latter variable is crucial for the interpretation with respect to the shape of the CMB (Chapter 9).

²the so called Poincaré flow

³This is almost identical to the mantle which is observed at the surface of the Earth.

5.2.1 Free Wobble

First the rotating Earth without periodic tidal forcing is discussed, since in this case the freely excited eigenmodes can be obtained. A possible exciting mechanism may be atmospheric winds exerting frictional and mountain torques on the surface of the planet. The atmosphere and the Earth's body are tightly coupled. In fact the strongest axial torques on the solid Earth are from the exchange of angular momentums with the atmosphere. The atmospheric torques are ten times larger than the core–mantle coupling torque [Merriam, 1990] at periods of a few days. *Herring and Dong* [1994] reported that there is more than enough power in the P_2^1 component of the atmospheric pressure field to randomly excite the NDFW rotational mode. Modeling the possible damping mechanisms may lead to a constraint on the viscosity of the outer core. One contribution in this work is the determination of the quality factor of the core resonance.

The homogeneous differential equation system 5.15 and 5.16 has two solutions. The first is again the Eulerian wobble, which leads for a realistic earth model to the Chandler wobble with the angular eigenfrequency

$$\omega_{CW} = \Omega \frac{A}{AM} \alpha \left(1 - \frac{k}{k_s} \right) \quad (5.17)$$

The frequency is equivalent to a period of 435 d . This prograde eigenmode is the only rotational mode a rotating *rigid* body with an ellipsoid surface would support. For a rigid earth model the eigenperiod would only be $T_{rigid} = 305 d$.

The second solution is a retrograde mode, the Nearly Diurnal Free Wobble which is the topic of this work. Its angular eigenfrequency for our simple model is determined by

$$\omega_{NDFW} = -\Omega \left[1 + \frac{A}{AM} \left(\alpha^C - \frac{q_0 {}^C h'}{2} + K' - iK \right) \right]. \quad (5.18)$$

The angular frequency is slightly larger than the Earth's rotation Ω , since the second term in angular brackets is small compared to 1. The dynamical ellipticity for an earth in hydrostatic equilibrium is $\approx 2.5 \cdot 10^{-3}$. The term with the Love number ${}^C h'$ describes the change of the dynamical ellipticity due to the instantaneous elastic deformation of the CMB caused by the NDFW. This term is not small. *Sasao et al.* [1980] claim it is 25 % of the leading term α^C . The terms describing the visco-elastic coupling have probably no perceptible influence on the eigenfrequency, since the coupling constants K and K' are expected to lie both in the range of 10^{-7} .

Connected to each wobble is a nutation in inertial space. The nutation and the wobble are two manifestations of the same rotational eigenmode. An observer on the Earth can perceive the wobble part of the mode relative to the earth–fixed system in variations of latitude. The isolated nutation part of the mode can only be observed in space relative to fixed stars. It can be verified by variations in the declination of stars. An observer on the Earth with the reference system of the fixed stars (see VLBI in Chapter 9) will always perceive a combination of the nutation and the much smaller wobble (the motion of the rotation axis in space combined with the deformation of the surface).

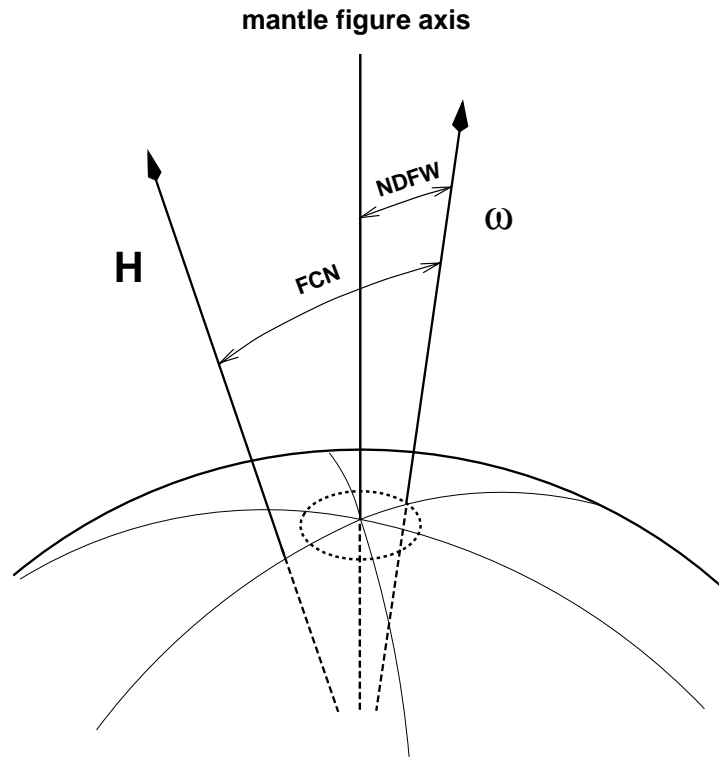


Figure 5.5: Axes describing wobble and nutation. All three axes intersect with each other at the center of the Earth. The circle on the surface traces the motion of the ω -axis. The amplitudes (exaggerated in this sketch) of the wobble and nutation are indicated by double arrows.

Wahr [1981] theoretically determined a period of the FCN of 460 sidereal days (*sid. d.*). Recent numerical calculations of Jiang [1993] with the finite element method and full consideration of the Coriolis term resulted in a FCN period of 448.6 *sid. d.* Modern observational estimates of the FCN period (see chapter 6.1) are systematically shorter. Since the moments of inertia of the mantle respectively of the whole Earth are known with high accuracy, the dynamical ellipticity α^C is the only parameter which can be changed to fit a theoretical model. Excess flattening of the CMB could be explained with a non-hydrostatically pre-stressed Earth and would allow to reconcile theoretical and observational estimates of the wobble frequency. The movement of the Earth's rotation axis around the figure axis of the mantle describes a cone with the tip at the center of the Earth: the wobble. Simultaneously the rotation axis moves around the axis of the total angular momentum also describing a cone: the nutation. The rotational eigenmode as a whole fits the description of two cones rolling in each other without slipping (discussed in section 5.1). Since the wobble and the nutation are two realizations of one eigenmode it is understandable from the geometric conditions above that between wobble and nutation frequency there exists a relation:

$$\omega_{wobble} = \omega_{nutations} - \Omega. \quad (5.19)$$

with Ω being the angular frequency of the rotation with respect to the fixed star system. Furthermore in approximation of small amplitudes a relation between the amplitudes and frequencies of wobble and nutation holds:

$$\frac{\omega_{nutation}}{\omega_{wobble}} = \frac{a_{wobble}}{a_{nutation}} \quad (5.20)$$

Fig. 5.5 shows schematically the relative position of the axes at the surface at a certain moment in time. The amplitude of the nutation exceeds the wobble amplitude by far. In reality the differences in amplitude is more conspicuous. For modern earth models the ratio of the amplitudes is about 1/460. Since *Herring and Dong*, [1994] found an amplitude of 0.844 nrad (equals 5.38 mm at the surface of the Earth for the freely excited FCN from VLBI (see Chapter 9.1) measurements, this implies an amplitude of the NDFW of 0.002 nrad ($11.7 \mu\text{m}$ at the surface of the Earth).

The situation for the Chandler wobble is reverse: a large wobble is accompanied by a smaller nutation. Fig. 5.2 resembles this constellation. The Chandler wobble will not be discussed any further.

A similar eigenmode will be obtained if the boundary between inner core and outer core is elliptical as well. The resulting inner core wobble is discussed in *Wahr and De Vries*, [1991] and *Mathews et al.*, [1991]. According to their calculations the inner core mode should have only a negligible influence on the earth tide response and small effects on the nutation amplitude.

5.2.2 Forced Wobble

When a periodic forcing mechanism exists (see Fig. 1.2) the Earth responds with forced motions instead of free oscillations. The diurnal tesseral tidal potential V_{21} has the appropriate temporal and spatial distribution to excite the NDFW. Due to the diurnal tesseral tides the orientation of the principal axes of inertia is affected. In Equation 5.15 and Equation 5.16 the periodic potential $V_{21} = V_0 e^{i\omega t}$ is substituted for V . Then the response of the Earth becomes with respect to the equatorial components of the rotations $\omega = \omega_1 + i\omega_2 = \omega_0 e^{i\omega t}$, respectively, $\omega^c = \omega_1^c + i\omega_2^c = \omega_0^c e^{i\omega t}$ of the whole Earth and the core [*Hinderer et al.*, 1982]:

$$\omega_0 = \frac{(\omega + \Omega) \left(1 - \frac{A^c q_0 h^c}{2\alpha A}\right) + \Omega \left(\alpha^c + \frac{q_0' h^c}{2}\right)}{\omega - \tilde{\omega}_{NDFW}} \frac{A}{A^M} \frac{3\alpha V_0}{\Omega R^2} \quad (5.21)$$

and

$$\omega_0^c = \frac{1 - \frac{q_0 h^c}{2\alpha}}{\omega - \tilde{\omega}_{NDFW}} \frac{A}{A^M} \frac{3\alpha V_0}{R^2} \quad (5.22)$$

These are the amplitudes of the differential rotation of the whole Earth and the core. The term $(\omega - \tilde{\omega}_{NDFW})^{-1}$ indicates a resonant behavior in the rotations (due to the presence of the eigenmode) for a given angular frequency ω and potential amplitude V_0 near the complex angular frequency $\tilde{\omega}_{NDFW}$. The predominant core rotation ω_0^c leads to a fluid overpressure at the CMB and consequently to a deformation. This

elastic deformation results in a resonant tidal gravity change which is described for example by a frequency dependent δ -factor [*Hinderer et. al*, 1991]:

$$\delta = 1 + h - \frac{3}{2}k + \Omega \frac{A}{A^M} \frac{\left(h' - \frac{3}{2}k'\right) \left(\alpha - \frac{g_0 h^C}{2}\right)}{\omega - \tilde{\omega}_{NDFW}} \quad (5.23)$$

The first three terms correspond to the δ -factor of a spherical Earth (Equation 3.11). For frequencies far from the resonance (eg. near tide O_1) the fourth term almost vanishes. For the real Earth the the complex tidal admittances \tilde{D} (i.e. the δ -factor for gravity, the amplitude of linear strain and the tilt-diminishing factor *eta*) can thus be splitted into the component \tilde{D}_{SNREI} representing the spherical Earth (no frequency dependence) and the resonant component \tilde{R} , so that

$$\tilde{D} = \tilde{D}_{SNREI} + \tilde{R} \quad (5.24)$$

The resonance part \tilde{R} can be isolated and interpreted analogously to a classical harmonic oscillator with eigenfrequency, quality factor and complex resonance strength.

5.3 The model of the classical harmonic oscillator

In the following the complex tidal admittances as provided by ETERNA after the ocean load correction are used. For the NDFW fit the tides O_1 , P_1 , K_1 , ψ_1 and ϕ_1 are used. The last four waves are strongly influenced by the resonance. In order to isolate the contribution \tilde{R} of the resonance the tide O_1 is used as a reference tide. Therefore the complex tidal admittance of O_1 is subtracted from the complex tidal admittances of the other tides:

$$\tilde{R}(\omega_i) = \tilde{D}(\omega_i) - \tilde{D}(\omega_{O_1}) \quad (5.25)$$

Proceeding in this way at the same time all frequency independent effects are eliminated and the influence of systematic calibration errors (and cavity effects on strain and tilt) is reduced. In the vicinity of the resonance frequency there is also the purely solar tide S_1 . This tide is not included in the NDFW analysis because its SNR is very low and this tide is heavily corrupted by meteorological effects (Chapter 8). The functional model for the resonance is the same as used by *Neuberg et al.* [1987] and several other authors: a harmonic oscillator with eigenfrequency ω_{NDFW} , damping factor γ and complex resonance strength $\tilde{A} = A + iB$ with real part A , imaginary part B and $i = \sqrt{-1}$. The model function \tilde{M} is given by:

$$\tilde{M}(\omega) = \frac{\tilde{A}}{\omega_{NDFW}^2 - \omega^2 + i\gamma\omega} - \frac{\tilde{A}}{\omega_{NDFW}^2 - \omega_{O_1}^2 + i\gamma\omega_{O_1}} \quad (5.26)$$

The unknowns are combined in the parameter vector $\boldsymbol{\theta} = (\omega_{NDFW}, \gamma, A, B)$ with $\gamma = \omega_{NDFW}/Q$ and the quality factor Q . In the calculations the near-resonance

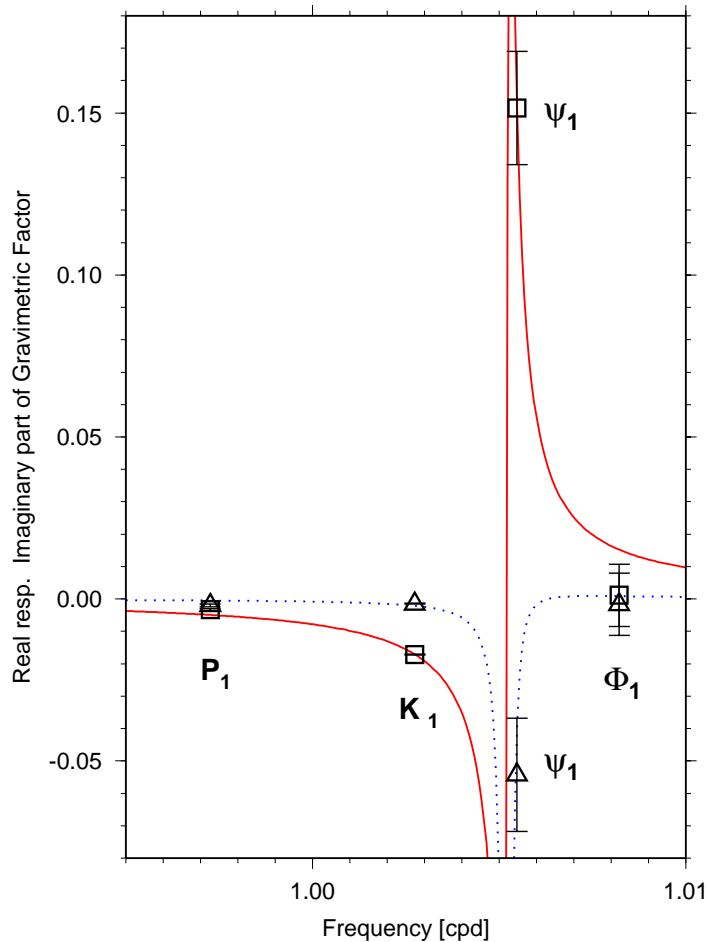


Figure 5.6: Resonant components of the gravimetric factor in BFO gravity data: the symbols square and triangle belong to the real and the imaginary parts respectively. The inverted model is represented by the real part (solid line) and the imaginary part (dotted line) on the basis of the solution vector $\boldsymbol{\theta} = (1.005211 \text{ cpd})$ (corresponding to $T_{FNC} = 405.5 \text{ sid.d}$), $\omega_{NDFW}/(-5360)$, $-0.58 \cdot 10^{-3}$, $-0.50 \cdot 10^{-4}$). Additionally the tidal constituents used in the inversion are indicated. The error bars are derived from standard deviations of the tidal analysis with ETERNA. The error contribution of ocean–tide loading corrections are neglected here.

approximation represented in real and imaginary part

$$\tilde{M}(\omega) \approx \frac{(\omega - \omega_{O_1}) [A (\omega_{NDFW} - \omega) + B\gamma]}{(\omega_{NDFW} - \omega)^2 + \gamma^2} + \mathbf{i} \frac{(\omega - \omega_{O_1}) [B (\omega_{NDFW} - \omega) - A\gamma]}{(\omega_{NDFW} - \omega)^2 + \gamma^2} \quad (5.27)$$

[Neuberg *et. al*, 1987] is used. An example of the harmonic oscillator model is shown in Fig. 5.6 in the complex representation of the gravimetric factors. In Fig. 6.1 the influence of the quality factor on amplitude and phase of the gravimetric factor is illustrated at higher frequency resolution. The discussion follows in Chapter 6.4.

Chapter 6

Estimation of the NDFW Parameters

The inversion problem in this application is the following: determine 4 unknowns out of 8 data in the case of individual data set inversion. In the stack of gravity, strain and tilt data the situation is a little improved with 24 data and 8 unknowns. This is a very poor data basis with a very low number of degrees of freedom, but the data used are restricted to tides which are significantly affected by the resonance. The problems to solve are overdetermined in the sense that the number of data exceeds the number of model parameters. This means no unambiguous analytical solution exists and therefore the data have to be fitted to the model. The function to be minimized in multiple dimensions is χ^2 , the misfit between model and data

$$\chi^2(\boldsymbol{\theta}) = \sum_{i=1}^n \frac{1}{\sigma_i^2} [\tilde{M}(\omega_i, \boldsymbol{\theta}) - \tilde{R}(\omega_i, \boldsymbol{\theta})]^2 \quad (6.1)$$

sampled at the angular frequencies ω_i . To take into account the data quality which increases with amplitude, the data are weighted with the reciprocal standard deviation σ_i of the i th tidal constituent. Because of the highly non-linear functional model (Equation 5.26) it appears useful to compare different optimization strategies. The minimization problem is solved iteratively with local methods in the two following sections. On one hand an iterated linearized least squares inversion scheme is performed with singular value decomposition. On the other hand a downhill simplex method is applied, which only requires function evaluations, but not derivatives. The iteration demands an initial model. For this purpose the results of a previous study [Neuberg, 1987] are chosen. Additionally joint inversions for more than one data set are performed. In that case the admittances are inverted together for a common resonance frequency and damping factor but individual resonance strengths pertaining to the different tidal signals. For a stack the solution vector becomes $\boldsymbol{\theta} = (\omega_{NDFW}, \gamma, A_1, \dots, A_l, B_1, \dots, B_l)$ for l data sets.

In one special inversion series the quality factor is held fixed at infinity. This is realized by constraining γ to zero. The justification is that a very high NDFW Q-factor

is commonly expected. With fixed Q only $2l + 1$ parameters have to be determined, this increases the number of degrees of freedom and will result in smaller formal error bars.

Even in the case of three data sets we have not an exuberant data basis for statistical conclusions. Therefore emphasis is put on the estimation of the uncertainties of the parameters in Chapter 7.

6.1 Linearized least squares method

Minimizing the residuals (Equation 6.1) is obtained by setting the partial derivatives with respect to the parameters θ_j identical zero [Draper and Smith, 1966]:

$$\frac{\partial \chi^2}{\partial \theta_j} = 0 \quad (6.2)$$

In the following the \sim symbol for complex variables is omitted for the sake of convenience. To be able to obtain a least squares solution the non-linear model function 5.27 must be linearized. For this purpose a Taylor series expansion of $M(\boldsymbol{\theta})$ about the point $\boldsymbol{\theta}_0$ is carried out. When the expansion is curtailed at the first derivative, then

$$M(\boldsymbol{\theta}) \approx M(\boldsymbol{\theta}_0) + \sum_{j=1}^m \left(\left. \frac{\partial M}{\partial \theta_j} \right|_{\boldsymbol{\theta}_0} \Delta \theta_j \right) \quad (6.3)$$

With the initial value $\boldsymbol{\theta}_0$ being close to the solution $\boldsymbol{\theta}$, Equation 6.3 is a reasonable approximation for $M(\boldsymbol{\theta})$. Then the so called normal equations result from Equation 6.2 :

$$\left(\mathbf{H}^T \mathbf{W} \mathbf{H} \right) \Delta \boldsymbol{\theta} = \mathbf{H}^T \mathbf{b} \quad (6.4)$$

with the components of the data kernel matrix

$$H_{ij} = \left. \frac{\partial M_i}{\partial \theta_j} \right|_{\boldsymbol{\theta}_0} \quad (6.5)$$

the data vector \mathbf{b} consisting of the components

$$b_i = W_{ii} (R_i - M_i) \quad (6.6)$$

the improvements of parameters $\Delta \boldsymbol{\theta}$ and finally the weights stored in the diagonal matrix \mathbf{W} with the non-vanishing elements $W_{ii} = 1/\sigma_i^2$. In matrix formulation the linear system of equations to be solved can be stated by:

$$\Delta \boldsymbol{\theta} = \mathbf{G}^{-1} \mathbf{z} \quad (6.7)$$

with

$$\mathbf{G} = \mathbf{H}^T \mathbf{W} \mathbf{H} \quad (6.8)$$

and

$$\mathbf{z} = \mathbf{H}^T \mathbf{b} \quad (6.9)$$

To solve the equation system iteratively a singular value decomposition is used. The initial parameter values have to be improved upon by the vector of model improvements $\Delta\boldsymbol{\theta}$ and then the resulting $\boldsymbol{\theta}$ have to replace the initial values in the subsequent iteration step:

$$\boldsymbol{\theta} = \boldsymbol{\theta}_0 + \Delta\boldsymbol{\theta}. \quad (6.10)$$

This iterative process has to be repeated until the solution converges, i.e. until in successive iterations k and $k + 1$:

$$\left| \frac{\Delta\boldsymbol{\theta}_{k+1}}{\Delta\boldsymbol{\theta}_k} - 1 \right| < \epsilon$$

with $\epsilon = 10^{-6}$. For the uncertainty $\sigma_{\Delta\theta_j}$ of a parameter $\Delta\theta_j$ determined out of n data R_i applies in general [Bevington, 1969]

$$\sigma_{\Delta\theta_j} = \sqrt{\sum_{i=1}^n \sigma_i^2 \left(\frac{\partial \Delta\theta_j}{\partial R_i} \right)^2} \quad (6.11)$$

A detailed discussion follows in Chapter 7.

6.2 Singular value decomposition (SVD)

Although least squares problems can be formally overdetermined it is possible that they are underdetermined in the sense that ambiguous parameter combinations exist [Press *et al.*, 1992]. In SVD routines combinations of basis functions irrelevant to the fit will be driven down. SVD finds solutions when other methods fail. Another criterion to use this algorithm for matrix inversion is that it dispenses with inverting the symmetric form $\mathbf{G}^T \mathbf{G}$ and therefore one source of numerical uncertainty is avoided.

Any $n \times m$ matrix \mathbf{G} (rows $n \geq$ columns m) can be expressed as the product of a column-orthogonal $n \times m$ matrix \mathbf{U} , a positive definite $m \times m$ diagonal matrix $\boldsymbol{\Lambda}$ and an orthogonal $m \times m$ matrix \mathbf{V} [Press *et al.*, 1992]:

$$\mathbf{G} = \mathbf{U} \cdot \begin{bmatrix} \lambda_1 & & & \\ & \lambda_2 & & \\ & & \dots & \\ & & & \lambda_m \end{bmatrix} \cdot \mathbf{V}^T \quad (6.12)$$

The elements of $\boldsymbol{\Lambda}$, the λ_j are the non-negative roots of the eigenvalues of $\mathbf{G}^T \mathbf{G}$. They are called singular values. The inverse of \mathbf{G} is represented by:

$$\mathbf{G}^{-1} = \mathbf{V} \cdot \begin{bmatrix} 1/\lambda_1 & & & \\ & 1/\lambda_2 & & \\ & & \dots & \\ & & & 1/\lambda_m \end{bmatrix} \cdot \mathbf{U}^T \quad (6.13)$$

For the decomposition first the matrix \mathbf{G} has to be transformed with the help of Householder algorithm into upper bidiagonal form, and then the actual decomposition with a QR procedure is performed [Wilkinson and Reinsch, 1971].

This decomposition can always be done even when the matrix is singular. Numerical instabilities can arise when the condition number which is formally defined as the ratio of largest singular value to the smallest one becomes too large. This is the case when there are very small but nonzero singular values. Then the matrix is ill-conditioned. In order to avoid this problem the reciprocals of singular values are set to zero when the corresponding condition number becomes larger than 10^3 . This means deleting $n - p$ equations of the equation system which are corrupted by roundoff errors. In doing so no useful information gets lost. The SVD solution

$$\Delta\boldsymbol{\theta} = \mathbf{V}_p \boldsymbol{\Lambda}_p^{-1} \mathbf{U}_p^T \mathbf{z} \quad (6.14)$$

is better in the sense of smaller residuals than those gained by many other methods.

6.3 Nelder–Mead simplex method

Also a simplex method [Nelder and Mead, 1965] for minimizing the multi-dimensional function 6.1 is applied. This iteration algorithm should not be confused with the simplex algorithm of linear optimization. This method may converge slowly, but has the advantage of only requiring function evaluations. No partial derivatives with the connected numerical inaccuracies resulting from the linearized functional dependence between data and model have to be evaluated. Also the data has not to be weighted for reasonable results. For numerical calculations the FORTRAN routine AMOEBA [Press et al., 1992] was implemented. The name of the used routine is characteristic for its proceeding: a geometric figure, the *simplex*, 'flows' (moves like an amoeba) in the m -dimensional model space to the functional minimum by assimilating to the topography of the environment.

A simplex consists of $m + 1$ vertices in m dimensions plus all their interconnecting line segments and faces enclosing a m -dimensional volume. In two dimensions a non-degenerate simplex is given by a triangle, in three dimensions by a tetrahedron. In this context degeneration means that a simplex confines a vanishing volume.

The function minimum (here the minimum of misfit) is found after a series of geometric transformations. The vertex with the largest function value is reflected at the subspace of the remaining vertices. So the vertex reaches a place of lower niveau. Simultaneously to the reflections elongations and contractions are possible. In doing so the simplex assimilates step by step to the topography of the m -dimensional space. In the 3-dimensional vector space possible transformations comprise: elongation of the simplex along inclined planes, reversion of the direction of motion, when the simplex runs perpendicularly into a valley and contraction of the volume in the vicinity of a minimum. These transformations lead the simplex downhill into the minimum of the χ^2 -plane.

The parameters of Neuberg [1987] make up one vertex of the initial simplex. The

other m vertices of this simplex can be constructed by:

$$\boldsymbol{\theta}_k = \boldsymbol{\theta}_0 + \boldsymbol{\epsilon}_k \quad \text{with } \boldsymbol{\epsilon}_k \ll 1$$

Although anticipating the parameter results, it must be mentioned that in the Nelder–Mead method a positivity constraint for the quality factor has been incorporated to suppress negative values. The reason is that a negative quality factor does not match the physical model of a damped harmonic oscillator. But on the other hand a high negative $Q = \omega/\gamma$ corresponds to a damping factor in the vicinity of zero. Within the error bars a distinction of the sign may then not be possible. This constraint is only applied to secure the reliability of the results. It is carried out by putting a penalty on negative Q during the iteration. Every time the function value for a parameter vector with negative Q shall be evaluated, the penalization means assigning to the misfit (Equation 6.1) an a priori high value.

It is well known that local methods are not able to distinguish between local and global minima. The least what can be done is to restart the procedure with one vertex being the claimed minimum to make sure that it returns to this point.

6.4 Inversion results

In the case of SVD the model fit is weighted by the standard deviations of the tidal parameters from the tidal analysis. It must be mentioned that the influence of uncertainties in the ocean corrections and the O_1 error influences are not taken into account here (this will be accomplished in the next chapter). In the simplex inversion no weighting of the tidal parameters at all is performed.

The results for the NDFW parameters of different inversions and their formal errors from the least squares estimation are listed in Table 6.1. In all cases the starting values for the parameters were the solutions of *Neuberg* [1987]. The information on the kind of inversion is found in the first column: the abbreviation of the data type, positivity constraint applied (*) or not, Q fixed (†) or not. The resonance periods T_{FCN} determined in this work are all considerably smaller than theoretical predictions and results from most other data sets. The gravimeter data which have the highest quality lead to the smallest resonance period, whereas the largest resonance period of the different inversions is reached by the least significant tilt data set. The resonance periods of this work span a range of 403 – 420 sidereal days. A selection of important published NDFW results is listed in Table 6.2 where the FCN periods vary only in the interval 430 – 437 sidereal days. The theoretic calculations even predict a resonance period between 449 – 474 sidereal days. The significance of these theoretically determined parameters is discussed in Chapter 9. The resonance period for the stack of the three data sets with unconstrained Q happens to be coincidentally the arithmetic mean of the three individual periods. Nevertheless for this case the influence of the tilt data seems to be negligible, since the NDFW parameter results are similar to the stack of gravity and strain alone. In general it

Table 6.1: Resonance parameters and their standard deviations. G, S and T are abbreviations for gravity, strain and tilt, respectively. The * symbolizes the application of a positivity constraint in the Nelder–Mead simplex method. Whereas all the other analyses are calculated by the SVD algorithm. Additionally the † symbol indicates an inversion with fixed infinite Q .

	T_{FCN} [sid.d]	$\gamma \cdot 10^{-3}$ [d^{-1}]	Q	$A \cdot 10^{-3}$	$B \cdot 10^{-3}$
G	405.5 ± 13.6	-1.17 ± 1.03	-5360 ± 4720	-0.58 ± 0.02	-0.03 ± 0.02
G*	413.4	0.00041	$1.6 \cdot 10^7$	-0.58	-0.05
G†	410.0 ± 10.4	0	∞	-3.43 ± 0.31	0.04 ± 6.57
S	410.6 ± 7.0	1.24 ± 0.52	5070 ± 2150	-6.13 ± 0.12	0.85 ± 0.12
T	420.2 ± 54.1	0.89 ± 3.85	7100 ± 30750	1.01 ± 0.27	1.85 ± 0.27
Stacks					
G S	412.3 ± 10.6	-0.61 ± 0.78	-10293 ± 13200	-0.57 ± 0.02 -6.14 ± 0.22	-0.04 ± 0.02 -0.50 ± 0.22
G* S	403.4	0.24	25980	-0.41 -6.25	0.13 -0.67
G† S	412.9 ± 8.7	0	∞	-3.41 ± 0.21 -36.74 ± 2.39	0.04 ± 4.19 -0.88 ± 4.19
G S T	412.7 ± 9.7	-0.53 ± 0.72	-11900 ± 16000	-0.57 ± 0.02 -6.13 ± 0.21 1.10 ± 0.12	-0.04 ± 0.02 -0.51 ± 0.21 1.73 ± 0.12
G* S T	407.6	0.44	14200	-0.42 -6.74 1.03	-0.14 -0.05 1.77

cannot be expected that the stack results are the mean value of the individual results with reduced parameter uncertainties, since the underlying inversion in those two cases is totally different: the number of parameters varies, the correlation between the parameters is different (see Section 7.1) and last but not least, the inversion problem additionally is non-linear. In the discussion of the confidence regions in the next chapter parameter correlation is also a topic.

The high quality gravity data demand a negative damping factor γ in the vicinity

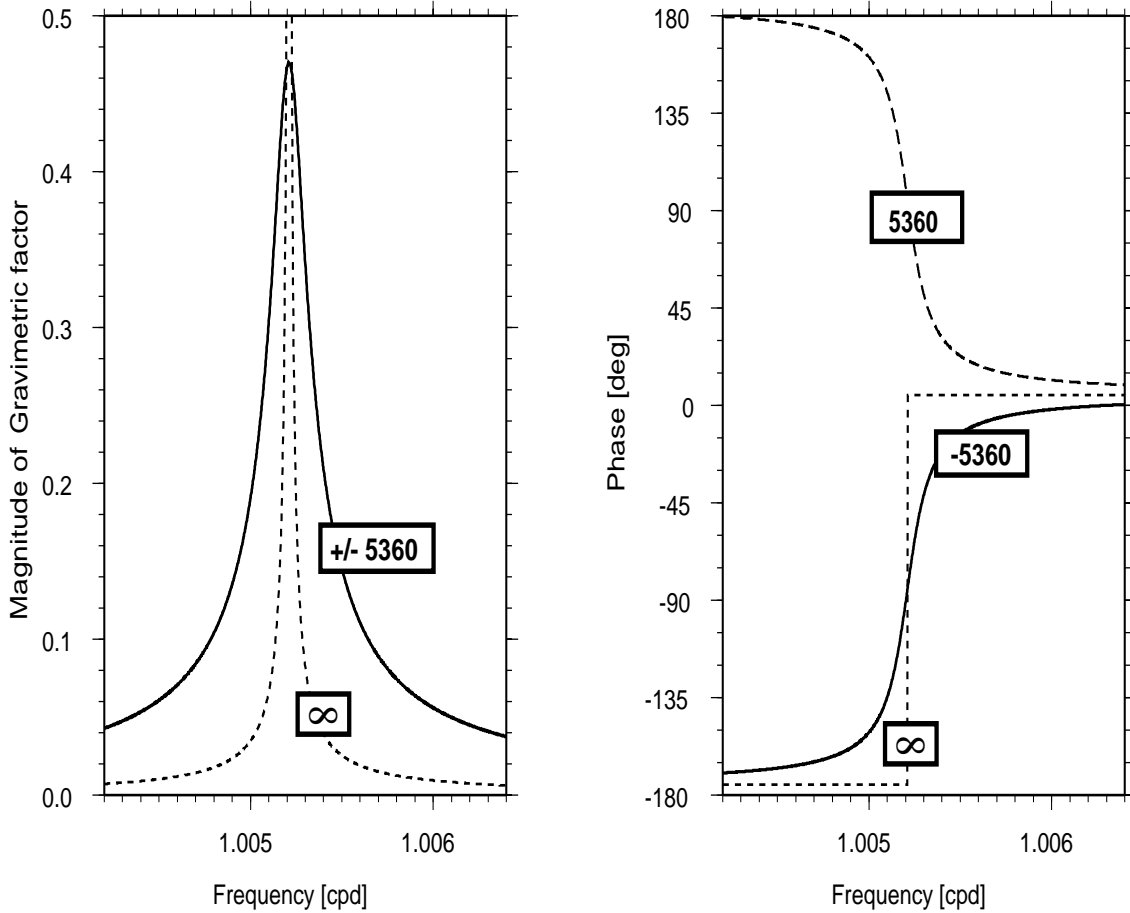


Figure 6.1: Different models of the reduced complex tidal admittance (resonant component of the complex gravimetric factor) in magnitude and phase representation. The limits of the phase variations do not reach 0 and 180 degrees, because the underlying formula is a near-resonance approximation with reference to tide O_1 . The graphs correspond to the parameter vectors $\theta = (1.005211 \text{ cpd}$ (corresponding to $T_{FNC} = 405.5 \text{ sid.d}$), ω_{NDFW}/Q , $-0.58 \cdot 10^{-3}$, $-0.50 \cdot 10^{-4}$) with Q -values as indicated in the boxes.

of zero. With 2σ error bars the sign of this γ is not significant. Physically a negative γ or Q is not reasonable, since no amplification mechanism can be assumed for the harmonic oscillator model of the last chapter. In general the information on the sign of Q is only inherent in the phase of the tidal parameters. The amplitude is not sensitive to the sign of Q (see Fig. 6.1). The sign of Q is mainly controlled by the tide ψ_1 and its uncertainties. This tidal constituent is closest to the resonance (see Fig. 5.6) and therefore fixes the phase of the oscillator and hence the sign of Q . The influence of the sign of Q on the amplitude factors can be seen in Fig. 6.1. The sign of the derivative of the phase with respect to frequency is inverse to the sign of the Q for finite Q values. In the fit an *a priori* infinite Q leads to higher resonance strengths (Table 6.1). This can be explained as follows. An oscillation with a high quality factor corresponds to a sharp spectral line whereas with a smaller Q its spectral

Table 6.2: Published NDFW results. The first three rows of the table belong to theoretical calculations, whereas the other parameters correspond to gravity, strain and nutation observations. In brackets the confidence region of the respective parameter is given. (This table also serves as legend to Fig. 7.14.)

Abbr.	T_{FCN} [sid. d]	Q	Publications
W	466.9		Wahr [1981]
WB	473.8	78100	Wahr & Bergen [1986]
J	448.5	∞	Jiang [1993]
NHZ	431.0 (425.0 – 437.0)	2758 (2222 – 3249)	Neuberg et al. [1987]
RZ	431.2 (427.6 – 433.8)	3120 (2797 – 3443)	Richter & Zürn [1988]
GH	433.2 (431.2 – 435.2)	16129 (12195 – 23809)	Gwinn et al. [1986]
S	432.9 (421.9 – 444.4)	5200 (2700 – 7700)	Sato [1991]
CW	437.0 (422.7 – 452.2)	5722 (3035 – 49869)	Cummins & Wahr [1993]
ST	436.7 (422.2 – 452.3)	6000 (3240 – ∞)	Sato et al. [1994]
M	430.0 (427.0 – 434.0)	7000 (5500 – 10000)	Merriam [1994]
F	430.7 (429.7 – 431.7)	2080 (1640 – 2520)	Florsch et al. [1994]
DDH	433.9 (433.2 – 434.6)	33000 (27000 – 43000)	Defraigne et al. [1995]
JS	431.0 (425.5 – 436.0)	2000 (1900 – 2100)	Jiang & Smylie [1995]

representation is a broad spectral peak with increased amplitudes at the flanks. The resonance strengths are fitted to compensate for this amplitude difference. The amplitude and consequently the SNR of ψ_1 is low and since the uncertainty is determined from the SNR the uncertainty has to be high. The disturbances of this tidal constituent are suspected to be of oceanic or meteorologic origin. As can be seen in Chapter 8 the barometric influence is not as high as expected. Consequently the main influence is due to the ocean. But the ocean correction has only been done with a scaling of the amplitudes in correspondence to the K_1 ocean correction. This is certainly wrong, but for ψ_1 and ϕ_1 no individual ocean correction calculations were available for this work. In the future also ocean corrections for small tides should be determined individually from ocean surface observations. When Q is kept constant, the formal errors of the resonance periods decrease as expected. In conclusion the quality factors determined in this work range between -11000 and -5000 respectively 5000 and $+\infty$. Independent of the sign of the quality factor the real and imaginary part of the resonance strength are negative and the imaginary part is about one order of magnitude smaller than the real part in the unconstrained cases.

Other authors, eg. *Neuberg et al.* [1987]; *Cummins and Wahr* [1993] as well as *Merriam* [1994] found also a real part of the resonance strength about $6 \cdot 10^{-4}$ and an imaginary part of 10^{-5} or less. The strain resonance strength of $(-0.00723 + i 0.82) \cdot 10^{-3}$ from *Neuberg et al.* [1987] is similar to the one of this work. *Sato's* [1991]

real part of the resonance strength is a factor 20 smaller than the one of this work and the imaginary part even more so.

Due to the appreciable differences in the resonance periods between the result of this work and other publications in the next chapter the confidence intervals of the parameters are investigated thoroughly. The judging of the different results are also postponed to the next chapter.

Chapter 7

Confidence intervals for the NDFW parameters

In the inversion of an individual data set 4 unknowns are estimated from 8 data, while in the stack the situation is a little improved with 8 unknowns being estimated from 24 data. This is not exuberant for statistical conclusions. However, formally under the condition of uncorrelated and normally distributed measurement errors, the estimated uncertainties $\sigma_{\Delta\theta_j}$ of the parameters can be calculated from the covariance matrix \mathbf{C} [Press *et al.*, 1992] composed of

$$C_{jk} = \mathbf{cov}(\Delta\theta_j, \Delta\theta_k) = G_{jj}^{-1} \quad (7.1)$$

(see system of linear equations 6.13). The uncertainty of parameter θ_j is given by the diagonal element C_{jj} of the least squares solution in the final iteration [Press *et al.*, 1992]:

$$\sigma_{\Delta\theta_j} = \sqrt{C_{jj}} \quad (7.2)$$

These uncertainties are very strongly dependent on the final misfit. Their values are given in Table 6.1. For the χ^2 fit by singular value decomposition the formal errors can be extracted from the matrix \mathbf{V} (see Equation 6.12) and the singular values λ_i [Press *et al.*, 1992]

$$C_{jk} = \sum_{i=1}^p \frac{V_{ji} V_{ki}}{\lambda_i^2} \quad (7.3)$$

The columns of \mathbf{V} represent vectors which coincide with the principal axes of the error ellipsoid of the estimated parameters $\boldsymbol{\theta}$. The length of the semi-axes of the error ellipsoid in p dimensions is given by the reciprocal singular values. Eq. 7.3 is only strictly valid if the measurement errors are normally distributed and uncorrelated. The normality assumption cannot be verified with a small number of 8 or at most 24 data points. The non-linear functional dependence between tidal admittances and resonance parameters implies that the error ellipsoids are only a linear approximation valid in some vicinity of the solution. The break-down of the linear approximation (Eq. 6.3) is characterized by the deviation of the contour

lines from their elliptic shape what can be seen in Fig. 7.1. Furthermore the non-linearity of the problem makes it difficult to analytically propagate the exact form of the noise distribution in the measurements¹ into confidence intervals for the resonance parameters. While the standard error of the tidal measurements may be normally distributed (Fig. 3.3) the uncertainties of the estimates of the resonance parameters do not necessarily have to show this property as well. The confidence regions for a certain error probability α cannot be determined exactly, but only as an *approximation*.

Additionally there surely exists a correlation between wobble frequency (the nutation period T_{FCN} respectively) and real part of the resonance strength A as well as between the damping term γ and the imaginary part of the resonance strength B whereas resonance frequency and damping term are found to be not correlated [Zürn and Rydelek, 1991]. This is verified in the next section by determining the misfit (Eq. 6.1) for each parameter combination in a restricted area in the parameter space in the vicinity of the least squares solution.

Since the amount of data is so small in the two subsequent sections a large number of synthetic data sets are simulated by adding deterministic and random errors to the tidal parameters, respectively, the load corrections. For each of these synthetic data sets the same procedure of NDFW parameter estimation is performed. From these simulated parameters statistical properties for the *true* data set could be derived.

7.1 Variances from F-statistics

There is a simple method to find the resonance parameters and improved uncertainties (over formal errors) *without* any linearization. A limited volume of the p -dimensional parameter space can be scanned for every parameter combination $\boldsymbol{\theta}$ which represents a resonance model. From the misfit $\chi^2(\boldsymbol{\theta})$ according to (2) an F-statistic can be computed, although F-tests are not strictly valid in the non-linear situation:

$$F(\boldsymbol{\theta}) \approx \frac{n-p}{p} \cdot \frac{\chi^2(\boldsymbol{\theta}) - \chi^2(\boldsymbol{\theta}_{min})}{\chi^2(\boldsymbol{\theta}_{min})}, \quad (7.4)$$

with n being the number of data, p the number of parameters and $\boldsymbol{\theta}_{min}$ the parameter vector pertaining to the least squares minimum. From the statistical F-distribution [eg. Abramowitz and Stegun, 1968] we can determine $F(p, n-p, 1-\alpha)$ for an error probability α , respectively an $(1-\alpha) \cdot 100\%$ approximate confidence region. The contours are correct confidence contours, and it is only the probability level which is approximate. Comparing F-values as functions of α with the empirical ones for different parameter combinations allows to obtain the confidence regions for $F(\boldsymbol{\theta}) = \text{const.}$ in the parameter space. The corresponding contour lines can be

¹here, uncertainties of tidal estimates

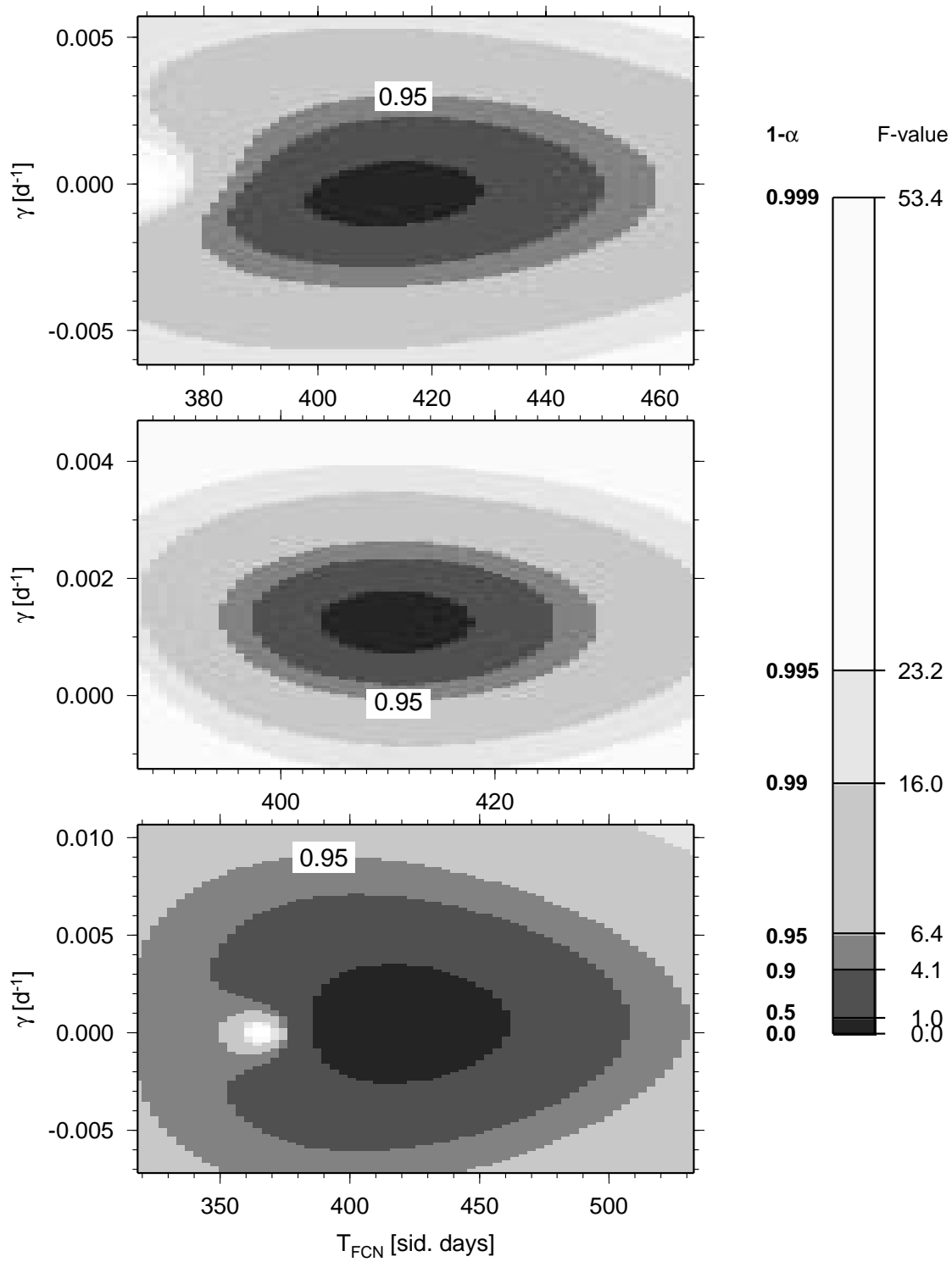


Figure 7.1: Projection of the approximate F-values resp. confidence regions onto the resonance period versus damping factor plane for gravity (upper panel), strain (middle panel) and tilt (lower panel). The F-values belong to the $F(4, 4, 1 - \alpha)$ - distribution. In the plot the 95% confidence contours are labeled.

Table 7.1: 95% approximate confidence intervals determined by F–statistics $F(4, 4, 1 - 0.95)$ [Abramowitz and Stegun, 1968] from Fig. 7.1.

	$\Delta_{T_{FCN}}$ [sid.d]	$\Delta_{\gamma} \cdot 10^{-3}$ [d^{-1}]
Gravity	$\pm 40.$	± 3.2
Strain	$\pm 17.$	± 1.4
Tilt	$\pm 107.$	± 8.5

found by projecting the extremal values of their contour lines from the 4D–parameter space onto the subspace of interest, eg. onto the γ – T_{FCN} –plane [Zürn and Rydelek, 1991]. Fig. 7.1 shows these contours for selected F–values for the three data sets of gravity, strain and tilt. The 95% confidence bounds found in these planes for T_{FCN} and γ are listed in Table 7.1. In contrast to linear models with their error ellipses, the confidence level contours in the non–linear case, beyond the region in the parameter space where the Taylor series approximation is valid, may be very complicated: eg. the confidence regions based on gravity data for small error probabilities α become kidney–shaped (Fig. 7.1 *top*). Consistent with the standard errors of the last section, we find the smallest bounds for strain (Fig. 7.1 *center*), namely $\Delta_{T_{FCN}} = \pm 17d$ and $\Delta_{\gamma} = \pm 1.4 \cdot 10^{-3}d^{-1}$. For all data sets the contours are approximately concentric ellipses which are for gravity and tilt aligned with the axes. Alignment of the contours to the coordinate axes is an indication for uncorrelated parameters. Only very slight correlation in the strain data is visible (very weak functional dependence of γ on T_{FCN} or vice versa). The smaller the correlation the more realistic the estimated parameter values should be. The largest uncertainties are again found for the estimated parameters for tilt data (Fig. 7.1 *bottom*). Their 90% confidence contour is deformed due to a misfit maximum at $T_{FCN} = 365d$. In the joint inversion (stack) the parameter space is different to individual inversions, since more unknowns have to be determined. The increased number of parameters in the joint inversion has the drawback that different parameter dependencies may exist and that parameters may be correlated differently. Defraigne et al. [1994] found a reduced parameter correlation in the case of stacked data sets with respect to individual data sets. In the following the parameter correlation for individual and joint data sets is compared. As an example the subspace spanned by T_{FCN} and resonance strength A is considered. In Fig. 7.2 the F–values for gravity and strain in this parameter plane are depicted. The elongated asymmetric contours show a slope relative to the coordinate axes. This implies a correlation between T_{FCN} and resonance strength A for both gravity (upper panel) and strain (lower panel). Correlation means that the parameters cannot be estimated independently [Draper and Smith, 1966]. The oblique, elongated² confidence contours of the individual data sets

²not closed in the range given

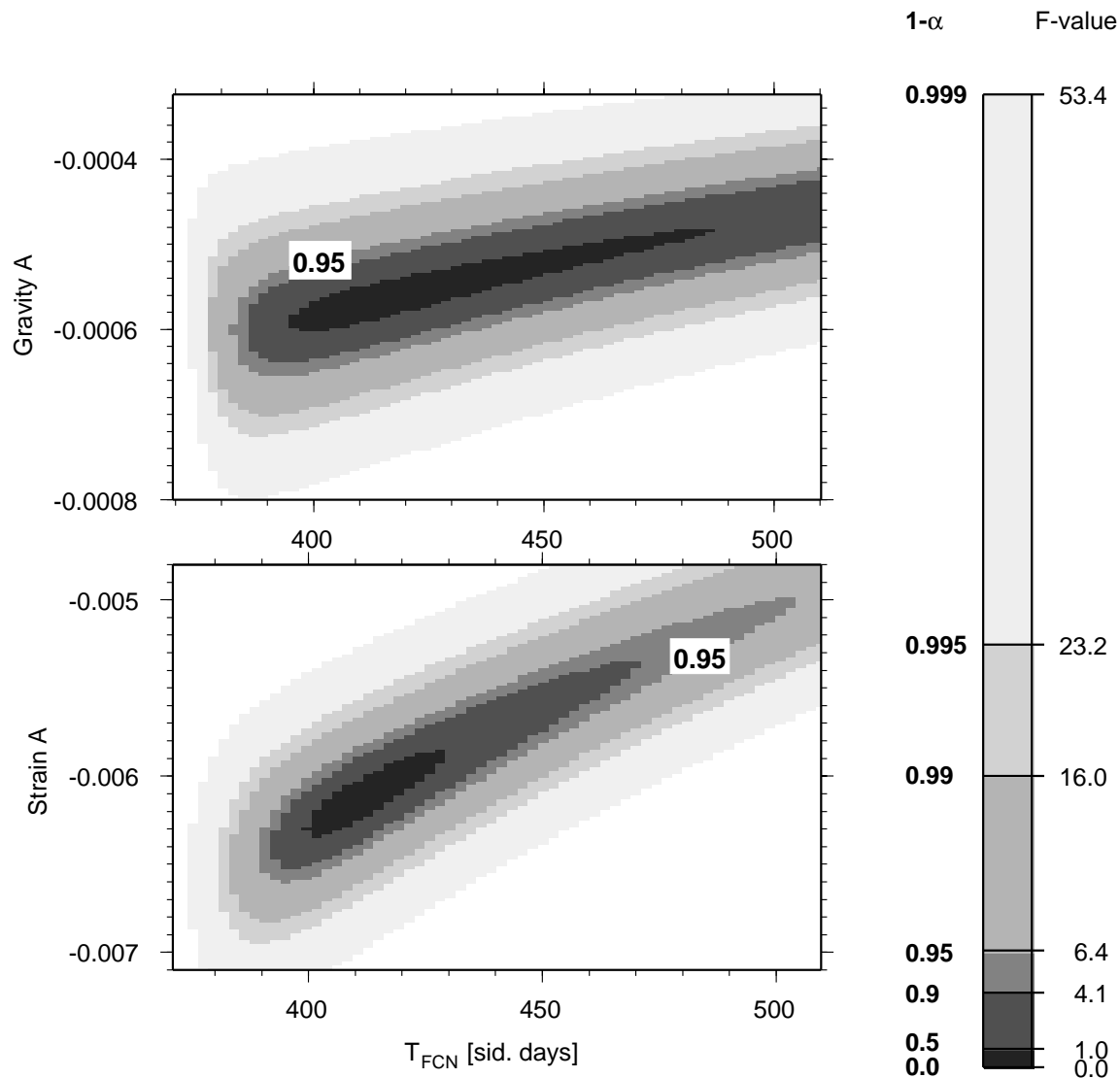


Figure 7.2: Confidence regions in terms of F -values projected onto the resonance period versus resonance strength A plane. The F -values belong to the $F(4, 4, 1-\alpha)$ -distribution. In the upper panel the situation is shown for gravity, in the lower panel for strain.

deform into closed contours resembling leaves in the stack of gravity and strain data (Fig. 7.3 *lower panel*). So the confidence region for the resonance period becomes smaller in the stack of both gravity and strain data. Their confidence contours look similar, although the ranges differ. The stack of gravity and strain leads to a visible reduction of the correlation between the strain resonance strength A and the resonance period (Fig. 7.3 *lower panel*). The minimum of the misfit surface in the $A - T_{FCN}$ parameter space seems to be flatter since the contour corresponding to the error probability of 50 % is not resolved.

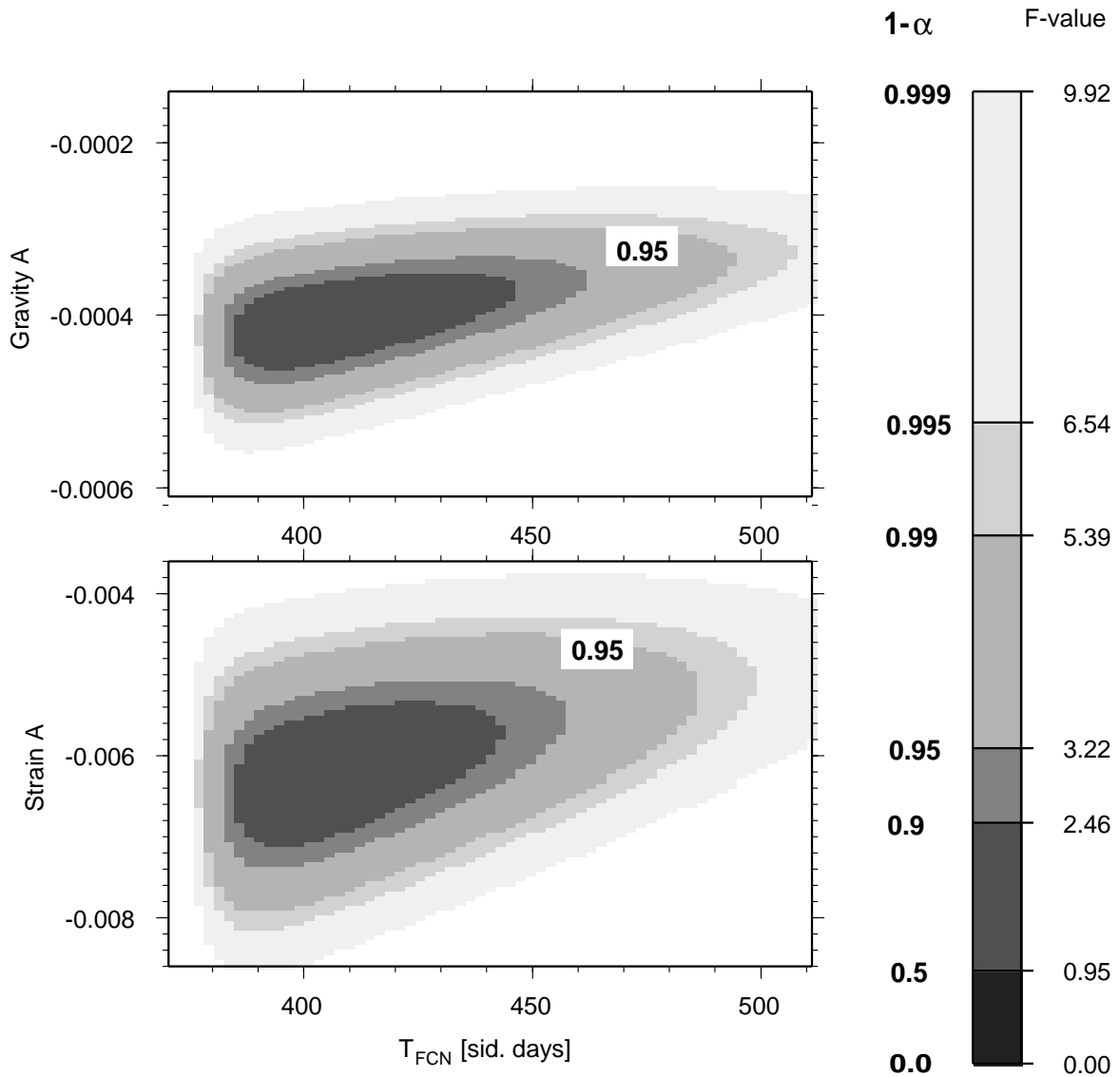


Figure 7.3: Confidence regions for the gravity–strain stack in terms of F–values. Illustrated is the projection onto the resonance period versus resonance strength A plane for gravity A in the upper panel and for strain A in the lower panel. The F–values belong to the $F(16, 10, 1 - \alpha)$ – distribution. The colours refer to the same probabilities $1 - \alpha$ as in the previous figures.

7.2 Propagation of deterministic errors

In the work of most other authors uncertainties in the resonance parameters are determined from the covariance matrix of the final iteration in the linearized least squares NDFW analysis. These uncertainties are very strongly dependent on the final misfit. The only way, by which the formal uncertainties (a measure of SNR) of the tidal parameters enter such an analysis is by the weights used in the inversions for NDFW parameters [eg. *Neuberg, 1987*]. If, say some data with low SNR happen to

have a very small misfit in the NDFW solutions, this low SNR would not be reflected in the uncertainties of the NDFW parameters, while data with high SNR could have a larger misfit and therefore would look inferior in the NDFW estimation. *Neuberg et al.* [1987] used a Monte Carlo method to assess the error propagation from the poorly known errors in ocean load corrections into the NDFW parameters. In the following the propagation of errors in the tidal analysis into the NDFW solutions is studied in similar ways. The approach will be to add an error term to the observed reduced complex tidal admittances \tilde{R} (defined by 5.25) and investigate the changes in the NDFW results. In this section this is done in a systematic manner and in the next section a statistical method, namely the Monte Carlo method is applied.

Here a deterministic complex error is added to the complex tidal admittance $\tilde{R}(\omega_i)$ of each tide. The magnitude is always one standard deviation σ of the admittance determined by ETERNA, but the phase is varied in 60° steps (0° , 60° , 120° , 180° , 240° , 300°). The unperturbed value is used as well. The disturbed admittances line out hexagons for each tide in the complex plane. All combinations for the five tides make up 7^5 experiments. With this method a volume in the NDFW-parameter space which results from the propagation of 1σ errors in the tidal estimates is defined. Another aim is to identify, which tidal constituent of each physical observable causes the largest deviations from the unperturbed solutions. Figs. 7.4 – 7.6 show the results of these computations in the $T_{FCN} - \gamma$ plane for gravity, strain and tilt. Each symbol in Figs. 7.4 a, 7.5 a and 7.6 a identifies the solution found for a certain combination of perturbations. For all three data sets the results split into 7 distinct groups (the 7th group in the case of tilt lies outside the range of the diagram). The pattern in each group is very dense with a fairly sharp elliptical to slightly hexagonal boundary. In order to better understand these patterns 30 cases are run, where only one tide was perturbed at a time. Figs. 7.4 b, 7.5 b, 7.6 b and 7.4 c, 7.5 c and 7.6 c show the results of these computations at different resolutions. The perturbed tide is identified in each case by its symbol (O, P, K, ψ , ϕ). The asterisk marks the solution for the unperturbed case. The parameter range of Figs. 7.4 c, 7.5 c and 7.6 c is identified by a rectangle in Figs. 7.4 b, 7.5 b and 7.6 b. Figs. 7.4 d, 7.5 d and 7.6 d show the reduced complex tidal admittances $\tilde{R}(\omega_i)$ with the standard errors from the ETERNA analysis and the determined resonance model $\tilde{M}(\omega)$ (defined by 5.27).

First the gravity and strain data are discussed (Figs. 7.4 a – 7.5 d). Obviously the separation into distinct groups is caused by the perturbation of ψ_1 . ψ_1 is also responsible for the asymmetry in the locations and the different sizes of the clouds. This is not surprising regarding \tilde{R} in the complex plane (Figs. 7.4 d and 7.5 d). The resonance model $\tilde{M}(\omega)$ in the complex presentation appears as circle through the origin [Goodkind, 1983]. Every point on the circle corresponds to a distinct frequency. Since $\tilde{M}(\omega)$ has O_1 as reference tide (Equation 5.27), the origin of the circle represents the frequency of O_1 . ψ_1 has the largest standard deviation and if the admittance is displaced in the complex plane by a phasor of length one σ this has a significant influence even though its weight is small. In connection with the sign of the damping factor for gravity it must be remarked here the following: if the

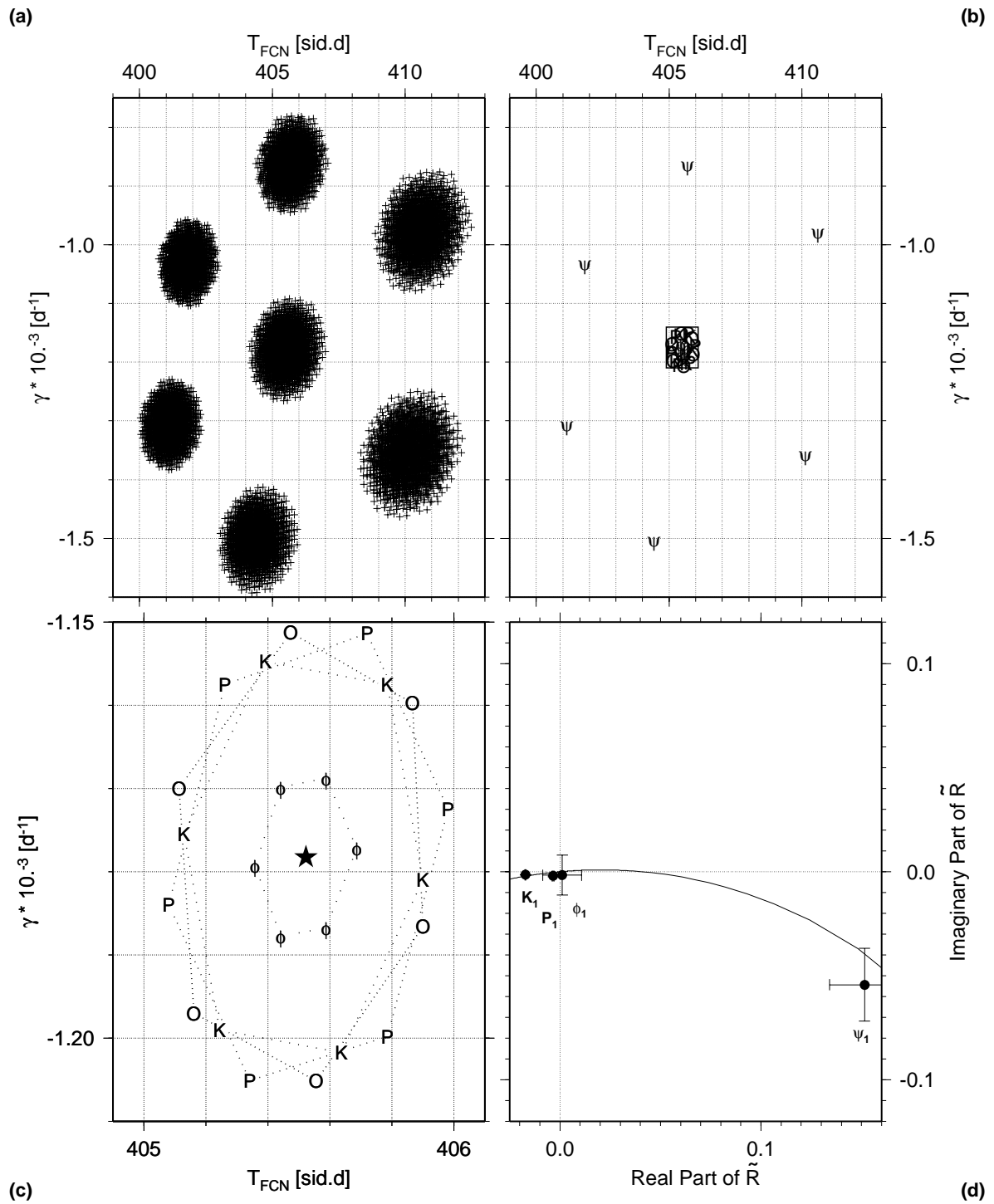


Figure 7.4: (a) – (c) NDFW-solutions in the T_{FCN} – γ parameter plane with deterministic error perturbations on the gravimetric factor. Each plus sign, each letter and the asterisk symbolize an individual solution. (d) shows the observed reduced complex tidal admittances \tilde{R} at the frequencies of the tides P_1 , K_1 , ψ_1 and ϕ_1 and reduced complex tidal admittances $\tilde{M}(\omega)$ for continuous frequency ω pertaining to the parameters of the unconstrained least squares solution in Table 6.1.

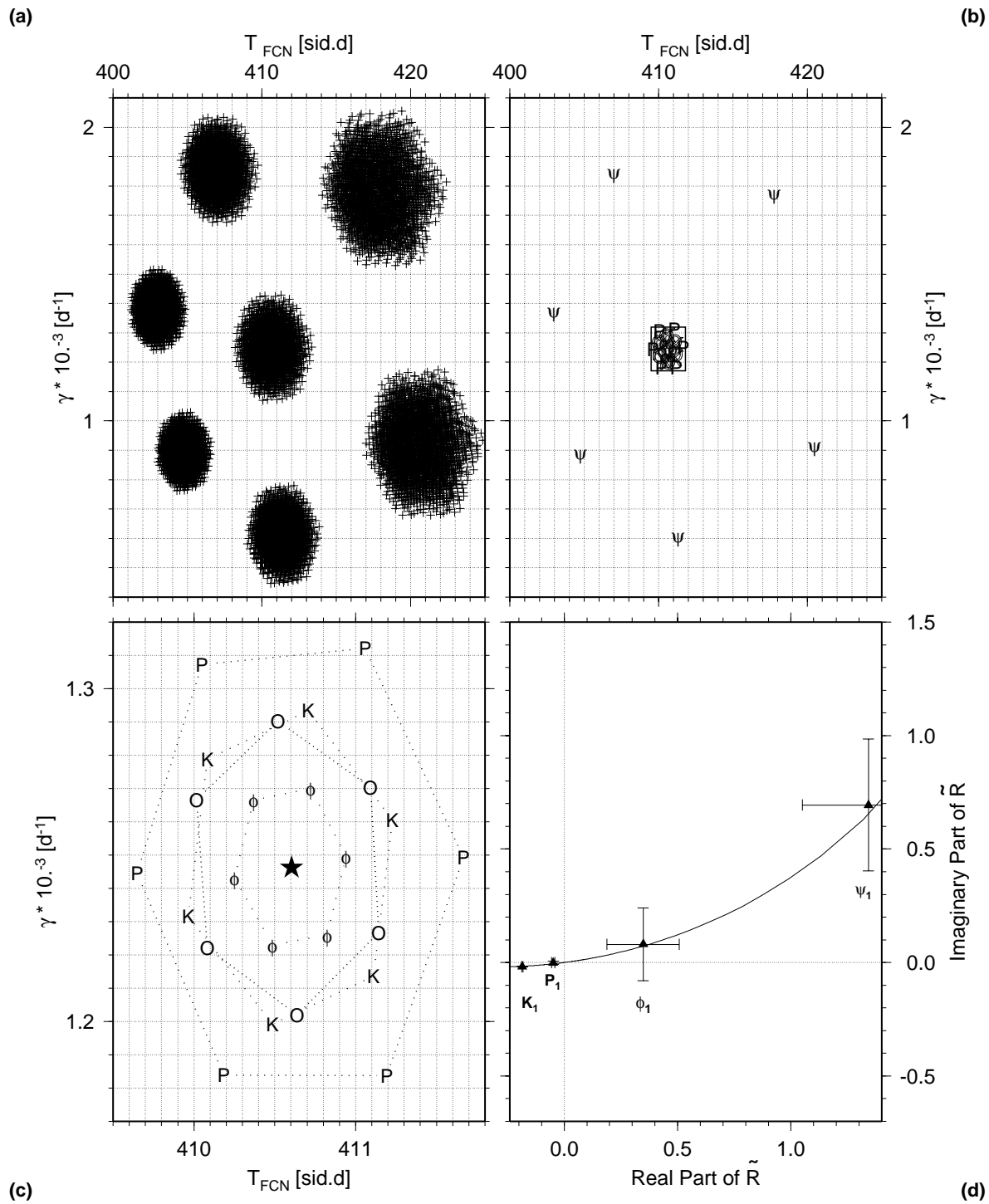


Figure 7.5: (a) – (c) NDFW-solutions in the T_{FCN} - γ parameter plane with deterministic error perturbations on the strain amplitude factor. Each plus sign, each letter and the asterisk symbolize an individual solution. (d) shows the observed reduced complex tidal admittances \tilde{R} at the frequencies of P_1 , K_1 , ψ_1 and ϕ_1 and the reduced complex tidal admittances $\tilde{M}(\omega)$ for continuous frequency ω pertaining to the parameters of the least squares solution in Table 6.1.

ψ_1 -admittance is shifted three standard deviations it can reach the first quadrant. Hence it is understandable that the resonance fit then leads to a larger resonance circle which is reflected at the real axis. This in turn corresponds to a smaller, positive damping factor.

Although ϕ_1 is closer to the resonance frequency than P_1 and has the second largest uncertainty, it apparently has a minor influence on the spread in the solution space. The tide P_1 has the second largest influence in the case of gravity. The influence of a tide appears to be determined by proximity to the resonance frequency and its uncertainty or weight. As the differences between gravity and strain results here show, the distributions of the reduced tidal admittances in the complex plane have a strong influence on the sensitivity and stability of the results for the NDFW parameters. The maximum uncertainties resulting from these perturbations are summarized in Table 7.2. In contrast to our previous estimates, here the gravity data have the smallest error bounds. The explanation is, that although the gravity fit is worse than the strain fit, the spread in the solution space is less, since the standard deviations of the δ -factors are smaller than for the strain admittances.

From Fig. 7.6 it is obvious that the situation is strikingly different for the tilt data. It was expected that these data despite their good quality will be less useful for the NDFW analysis because of their lower (compared to gravity and strain data) geophysical significance. This has been clearly verified here. The tilt data incorporate a rather large cavity effect [Neuberg, 1987] as can be seen from the reduced complex tidal admittances $\tilde{M}(\omega_i)$ in Fig. 7.6 *d*. However, this should not have any influence on the NDFW parameters T_{FCN} and γ , since only the resonance strength should be affected [Neuberg and Zürn, 1986; Zürn *et al.*, 1988], unless the ocean corrections are erroneous. This data set is also discussed in the analysis here to demonstrate the consequences for slightly inferior data. Fig. 7.7 *a* shows an extended range of the parameter space compared to Fig. 7.6. The transformation of Fig. 7.7 *a* into the frequency domain is represented in Fig. 7.7 *B*. In the f_{NDFW} - γ plane there are two distinct groups each containing close to one half of the total 7^5 solutions. The unperturbed case lies in the group with small spread (also, but not fully shown in Fig. 7.6 *a*), which is close to the solutions from my other data sets. The other group shows extremely large spread and is very far away from the expected values for T_{FCN} and γ . It consists of a number of hexagonal patterns with different sizes superimposed on each other. This second group splits into two in the T_{FCN} - γ plane, due to the relation between T_{FCN} and f_{NDFW} :

$$T_{FCN} = \frac{1}{f_{FCN}} = \frac{1}{f_{NDFW} - \Omega}$$

with Ω being the Earth's rotation rate in cycles per sidereal day. The solutions spread out enormously in the FCN period, while $T_{FCN} = 0$ is obviously not reached. The separation into two groups is here caused by disturbing ψ_1 and P_1 , as is suggested by Figs. 7.6 *b* and 7.6 *c* and which was verified by additional checks. The location of the unperturbed P_1 in the complex plane (Fig. 7.6 *d*) is so unfavourable that in adding perturbations two different classes of solutions of about the same size are created.

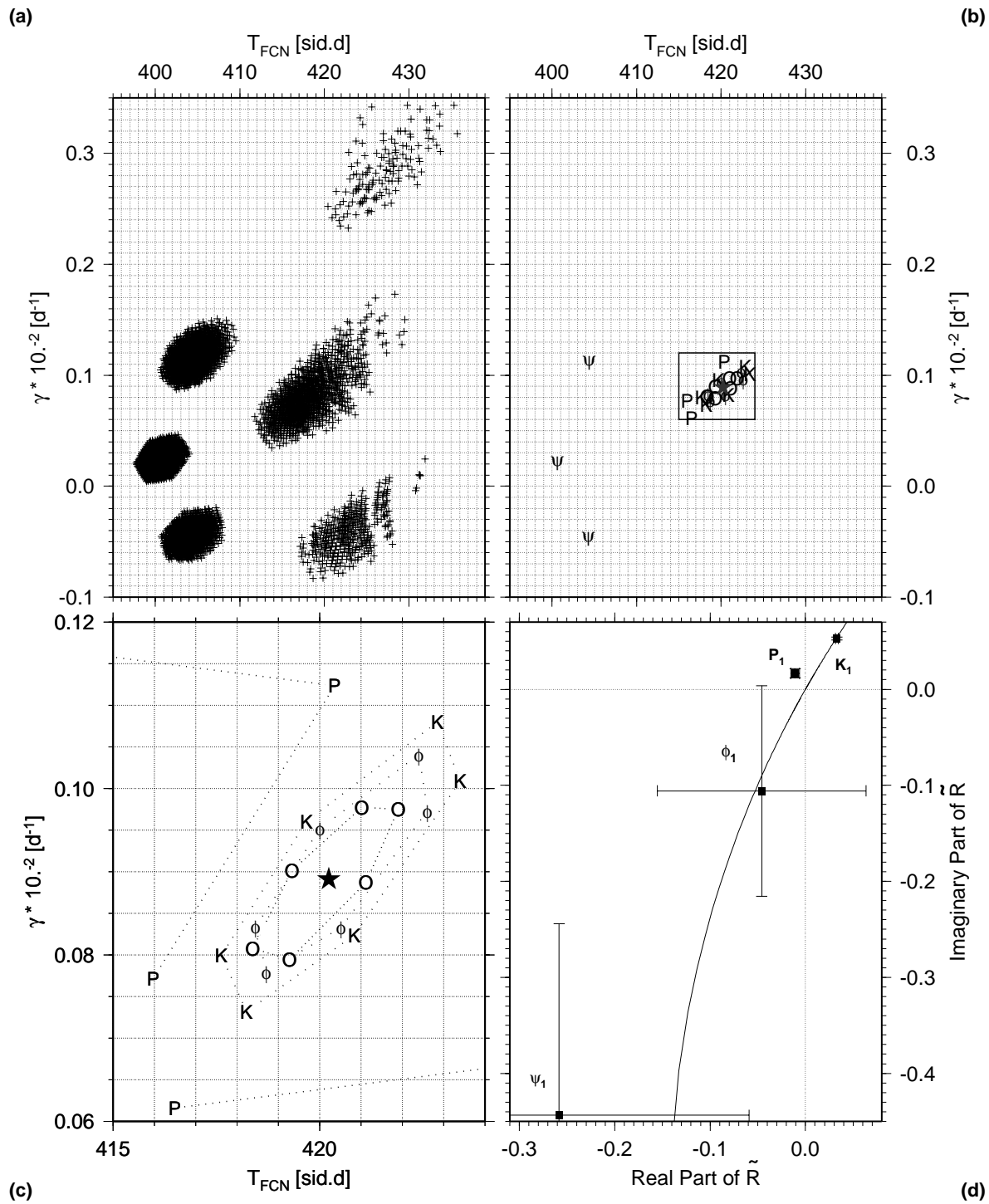


Figure 7.6: (a) – (c) NDFW-solutions in the T_{FCN} - γ parameter plane with deterministic error perturbations on the tilt diminishing factor. Each plus sign, each letter and the asterisk symbolize an individual solution. (d) shows the observed reduced complex tidal admittances \tilde{R} at the frequencies of P_1 , K_1 , ψ_1 and ϕ_1 and the reduced complex tidal admittances $\tilde{M}(\omega)$ for continuous frequency ω pertaining to the parameters of the least squares solution in Table 6.1.

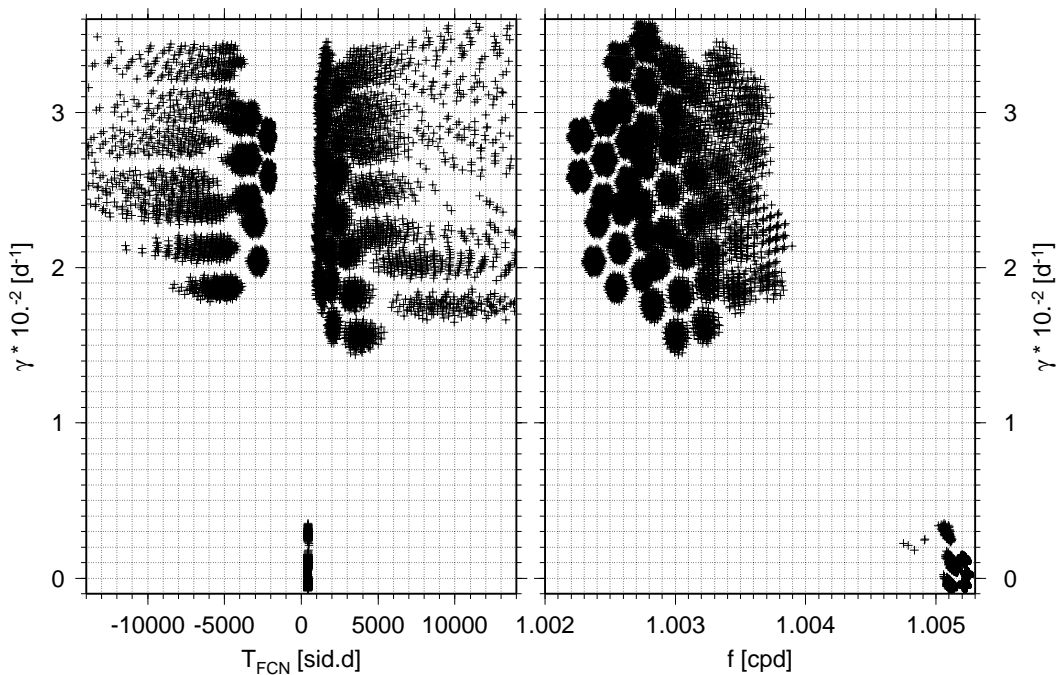


Figure 7.7: NDFW-solutions with deterministic error perturbations on the tilt diminishing factor: (a) sector of T_{FCN} - γ plane and (b) total range of f_{NDFW} - γ plane. Each plus sign symbolizes an individual solution.

Table 7.2: Resonance parameters and uncertainties from the estimation with deterministic errors (tilt: only one half of the solutions is considered).

	\bar{T}_{FCN} [sid.d]	ΔT_{FCN} [sid.d]	$\bar{\gamma} \cdot 10^{-3}$ [d^{-1}]	$\Delta\gamma \cdot 10^{-3}$ [d^{-1}]
Gravity	405.6	-5.5, + 7.0	-1.17	± 0.4
Strain	410.7	-10.0, + 14.0	1.24	± 0.8
Tilt	406.7	-9.0, + 29.0	0.45	-1.2, +2.8

The resonance circles of one class have a resonance frequency near 1.0029 *cpd* (cycles per solar day) and a small radius that corresponds to a large damping factor. These circles do not approach ψ_1 . The other class contains circles which have resonance frequencies near 1.005 *cpd*, large radii, or respectively small damping factors and lie in the vicinity of the admittance of ψ_1 . In Table 7.2 only the solutions of the latter class are mentioned, since those of the first class are not meaningful at all.

7.3 The Monte Carlo simulation

Estimating parameters means to determine parameters close to the *true* parameter set hidden from the experimenter. The experimenter only knows one realization of the parameter set, say θ^e which is corrupted by random measurement errors³ (deterministic errors are neglected here for simplification, they are discussed in section 7.2). We can also put it that way: The parameter set θ^e is only one member drawn from a probability distribution in the m -dimensional space of all possible parameter sets θ^* . Additionally to the actual data set synthetic data sets are simulated. The *true* parameter set is statistically realized with different random measurement errors (here: uncertainties of tidal parameters).

With the knowledge of the actual distribution law of the measurement errors a large number of data sets can be Monte Carlo simulated from a particular model (the least squares fit solution). These synthetic data can then be subjected to the actual fitting procedure, so as to determine both, the parameter probability distribution (Figs. 7.11, 7.12 and 7.13) and the accuracy with which the model parameters are reproduced by the fit.

Since the actual distribution law of the measurement errors is not known, it is assumed that the noise on the tidal estimates and load corrections can be described as independent complex random variables ϵ_{Tide} and ϵ_{Load} with a given probability distribution.

The general procedure of a Monte Carlo simulation can be divided into three steps. Transferred to the specific problem of this work this means:

1. Construct a distribution function for the error terms ϵ_{Tide} and ϵ_{Load} as follows: Let $\tilde{\epsilon}_{Tide}(\omega_i)$ be a realization of ϵ_{Tide} with normally distributed amplitudes, zero mean, the known variance σ_j^2 from the tidal analysis and uniformly distributed phase. The random variable ϵ_{Load} with its realizations $\tilde{\epsilon}_{Load}(\omega_i)$ is chosen to have uniformly distributed amplitudes as well as phases. The amplitudes amount at maximum to 10 %, 20 % and 40 % of the load corrections (see dimensionless load factors in Table 7.3).
2. Add to the observed reduced complex admittance $\tilde{R}(\omega_i)$ (defined by Equation 5.25) of each tidal wave a complex error term with the probability distribution mentioned in (1) :

$$\tilde{R}_{MC}(\omega_i) = \tilde{R}(\omega_i) + \tilde{\epsilon}_{Tide}(\omega_i) \quad (7.5)$$

respectively, add to each complex ocean load correction $\tilde{L}(\omega_i)$ (see Table 4.1 CSR 3.0) the corresponding error term:

$$\tilde{L}_{MC}(\omega_i) = \tilde{L}(\omega_i) + \tilde{\epsilon}_{Load}(\omega_i) \quad (7.6)$$

³to avoid confusion and to distinguish between the estimation of tidal and NDFW parameters, the estimated tidal parameters are in this section considered as ‘measurements’ and their uncertainties are therefore called ‘measurement errors’.

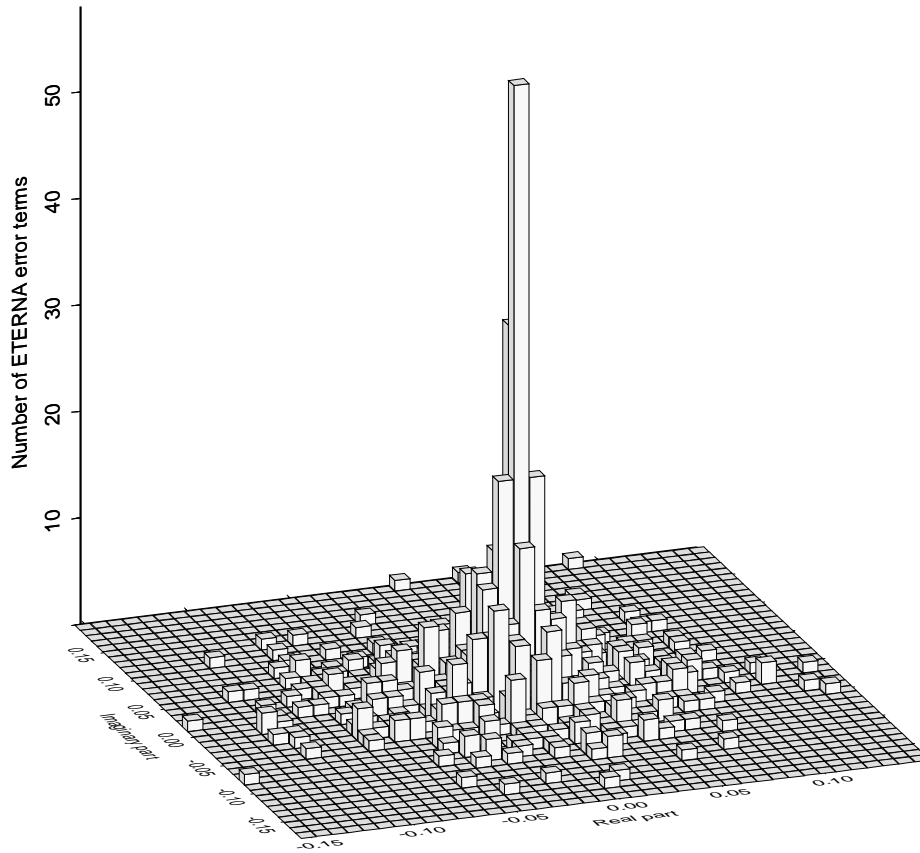


Figure 7.8: Histogram of the distribution of random generated K_1 ETERNA errors $\tilde{\varepsilon}_{Tide}$ for the constituent K_1 in the complex plane as input to the Monte Carlo simulations.

with $i = 1, \dots, 5$.

3. Repeat the second step a 1000 times and subsequently determine the NDFW parameters (Equations 6.7 and 6.14) and compute from this random sample the Monte Carlo means \bar{T}_{FNC} and $\bar{\gamma}$ and variances β_T and β_γ .

Under the assumption of high SNR⁴ the synthetic constructed ETERNA errors follow a 2-dimensional normal distribution (Fig. 7.8). Since nothing is known about the accuracy of the ocean load correction, the error distribution described under item (1.) is one reasonable possibility among others. This distribution (Fig. 7.9) is a compromise between a normal and an uniform distribution. Here the extremal error is varied, whereas *Neuberg et al.* [1987] only used the pessimistic value of 40 % of the load correction.

It must be mentioned that the ocean corrections for the small amplitude tides

⁴this requirement is surely met for every tidal constituent used, although there are large differences in the signal amplitudes of eg. K_1 and ψ_1

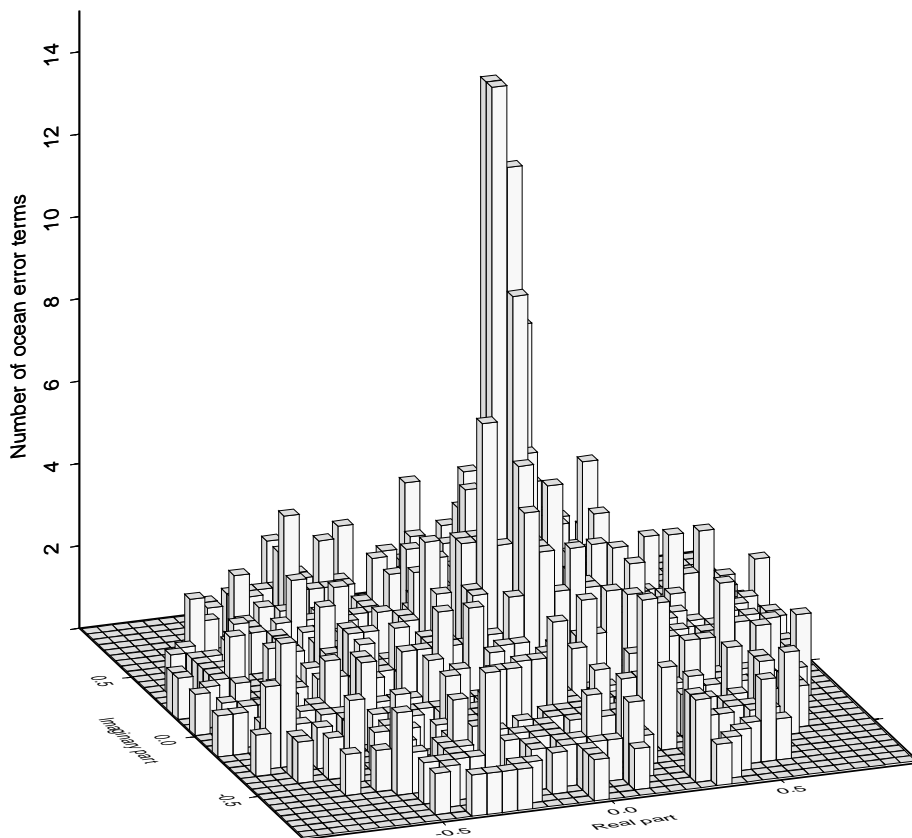


Figure 7.9: Histogram of the distribution of random generated K_1 ocean load errors $\tilde{\varepsilon}_{Load}$ (40 %) for the constituent K_1 in the complex plane as input to the Monte Carlo simulations.

ψ_1 and ϕ_1 are derived from the tide K_1 , because no individual models are available for them for BFO. Therefore the corrections for K_1 are scaled with the amplitude of the ψ_1 , respectively, ϕ_1 constituent. Equivalent scaling was performed to simulate the random ocean load errors. Due to the larger amplitudes, the synthetic ocean errors for the constituents P_1 and K_1 are about a factor of 100 larger than the corresponding errors for the tides ψ_1 and ϕ_1 (examples for K_1 and ψ_1 on the lower panel of Fig. 7.10). The random ETERNA error is scaled relative to the uncertainty from the tidal analysis, which is represented by the mean SNR in the diurnal tidal band. Expressed in admittances (eg. δ -factors) this would result in larger values for the tides ψ_1 and ϕ_1 compared to the tides P_1 and K_1 . But the tidal amplitudes of all the errors are the same for the respective constituent. This means that the least confident constituent ψ_1 has the same weight in the error analysis like the tide with the highest SNR, namely K_1 . This is important, since ψ_1 , the constituent closest to the resonance frequency has an important influence in the parameter fit (shown in the last section).

Since the influences of uncertainties of the tidal admittances and ocean load

Table 7.3: Resonance period T_{FCN} , damping factor γ and their uncertainties from Monte Carlo perturbations on tidal admittances and ocean load corrections are listed. The symbol † marks an inversion with fixed $Q = \infty$.

Type of signal	ETERNA perturb. [σ]	Load factor perturb.	\bar{T}_{FCN} [sid.d]	β_T [sid.d]	$\bar{\gamma} \cdot 10^{-3}$ [d^{-1}]	$\beta_\gamma \cdot 10^{-3}$ [d^{-1}]
Gravity		0.1	405.6	0.8	-1.2	0.1
		0.2	405.6	1.6	-1.2	0.1
		0.4	405.5	3.3	-1.2	0.2
	1		405.6	3.8	-1.1	0.2
	1	0.1	405.8	4.2	-1.1	0.2
	1	0.2	405.8	4.2	-1.2	0.2
Strain		0.1	410.6	0.4	1.2	0.0
		0.2	410.7	0.9	1.2	0.0
		0.4	410.7	1.8	1.2	0.1
	1		410.6	6.3	1.2	0.5
	1	0.1	410.7	6.3	1.2	0.5
	1	0.2	410.6	6.3	1.2	0.5
Tilt		0.1	484.	190.	3.	8.
		0.2	620.	456.	8.	12.
		0.4	812.	944.	10.	12.
	1		1320.	1900.	18.	11.
	1	0.1	1330.	2000.	18.	12.
	1	0.2	1360.	2165.	18.	13.
Gravity and Strain		0.1	412.3	0.6	-0.6	0.1
		0.2	412.4	1.2	-0.6	0.1
		0.4	412.7	1.5	-0.6	0.2
	1		412.4	3.9	-0.6	0.2
	1	0.1	412.5	4.0	-0.6	0.3
	1	0.2	412.6	4.2	-0.6	0.3
Gravity †	1		410.2	3.6	0	
	1		413.2	3.9	0	

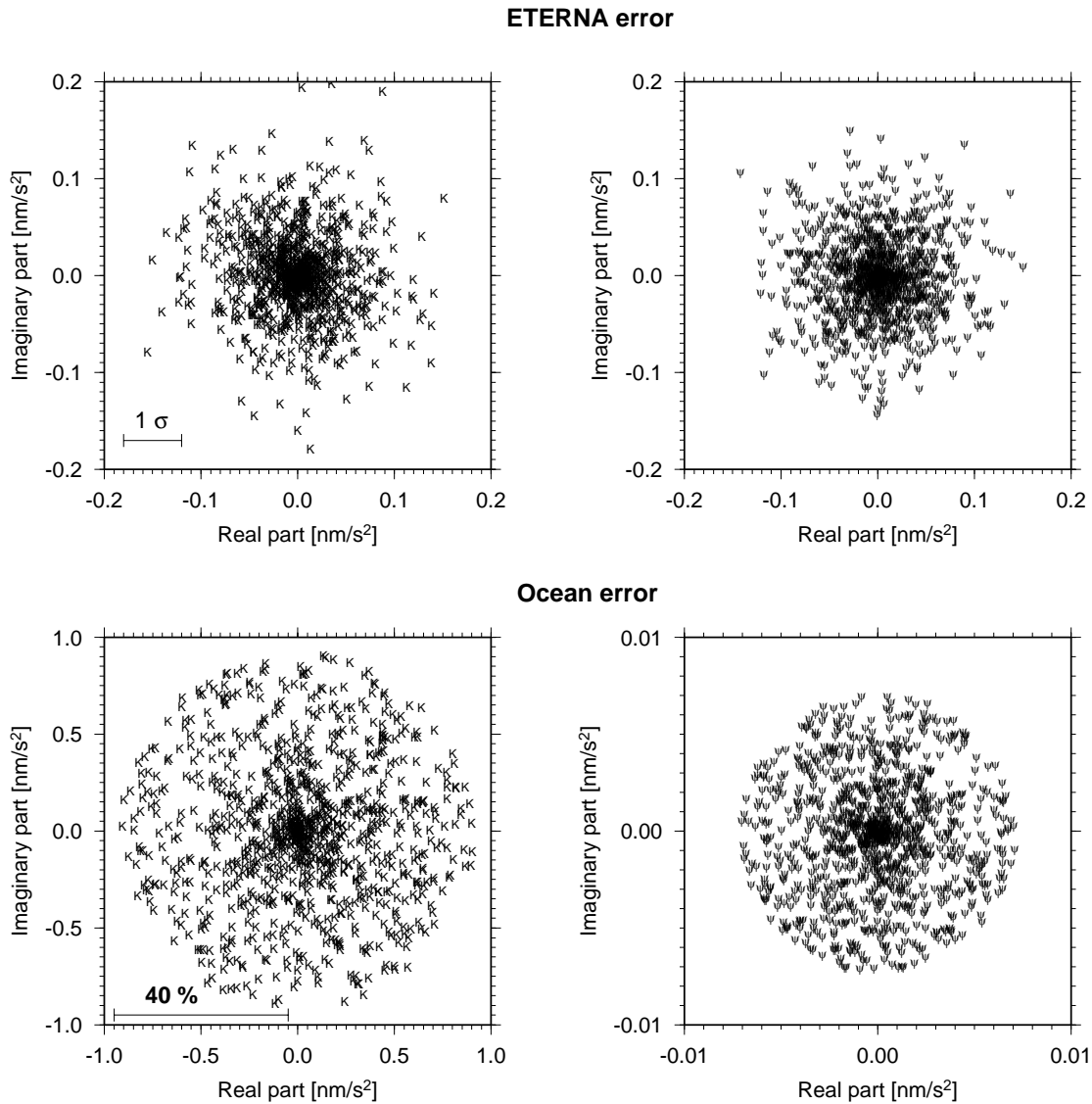


Figure 7.10: Comparison of random generated (ETERNA and ocean load) errors $\tilde{\varepsilon}_{Tide}$ and $\tilde{\varepsilon}_{Load}$ of tides K_1 to ψ_1 in the complex plane as input to the Monte Carlo simulations.

corrections should be investigated, it seems efficient to perform three separate simulations. These are: adding an error term to the tidal constituents, adding an error term to the load corrections and a combination of both perturbations. This means each individual data set is run through 7 different Monte Carlo simulations. Additionally this method is applied for stacks of gravity and strain data. From the results listed in Table 7.3 it is found that the uncertainties which are due to the load corrections are small compared to the influences of the error estimation for the tidal parameters (which are based on SNR of tidal measurements). This is a new result, because these errors have so far not been considered correctly by previous investigations (eg. see Table 6.2) analyzing for NDFW parameters. A similar analysis on

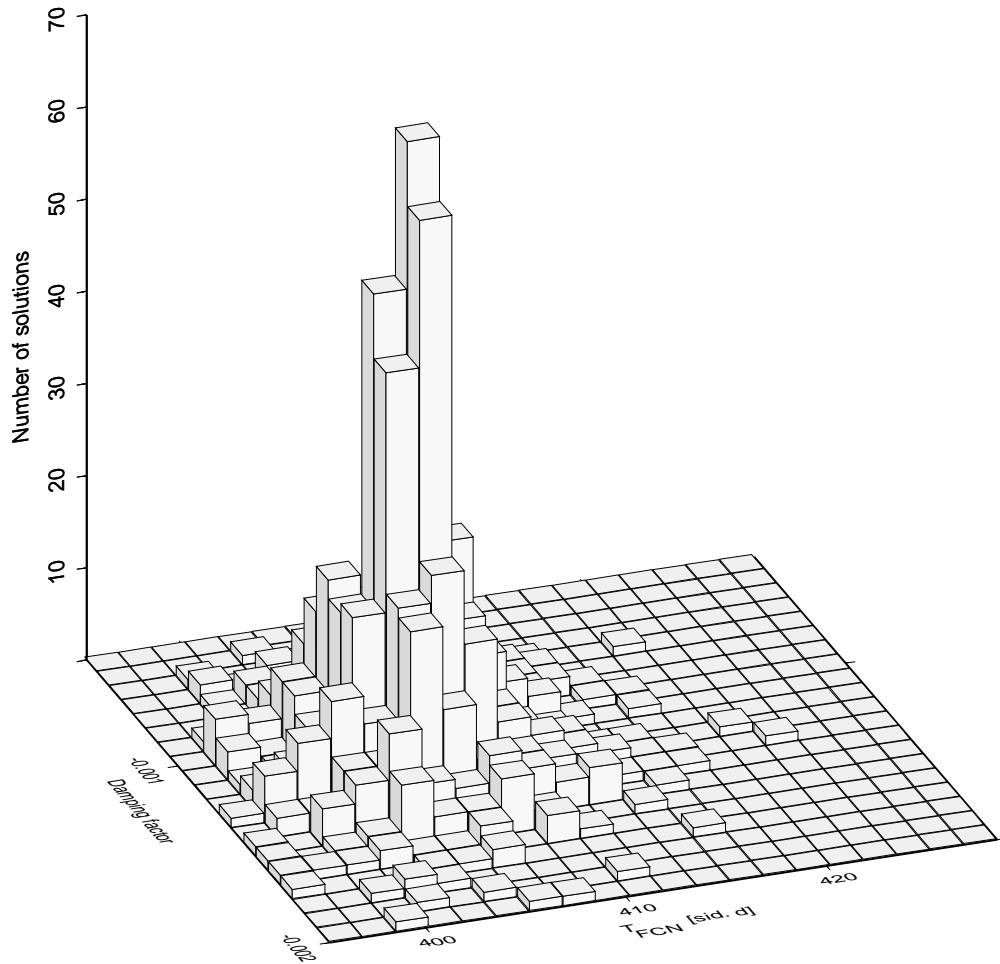


Figure 7.11: Histogram of NDFW gravity results in the damping factor – resonance period plane from Monte Carlo simulations ($\tilde{\epsilon}_{Tide} = 1\sigma$ and $\tilde{\epsilon}_{Load} = 0$).

nutations results would therefore be extremely interesting. The results of the previous section can be confirmed: There exists an asymmetry in the distribution of the obtained resonance parameters (Figs. 7.11, 7.12 and 7.13). The Monte Carlo results of gravity and strain and their stack are in good agreement with the unperturbed least squares solution. The tilt parameter estimates confirm the results of the last section. No reasonable, significant solution can be found. Even the smallest perturbation results in a parameter set far off the least squares solution in the parameter space.

The stack with a priori infinite Q leads to almost identical resonance periods as the inversions with free Q , whereas in the individual inversions for gravity in this two cases a difference of 4.6 *sid. d* in the resonance period is found. Results of this section together with the results of other authors are depicted in Fig. 7.14 in the $T_{FCN} - \gamma$ plane.

For reasons of comparison and in order to show the significance of the Monte

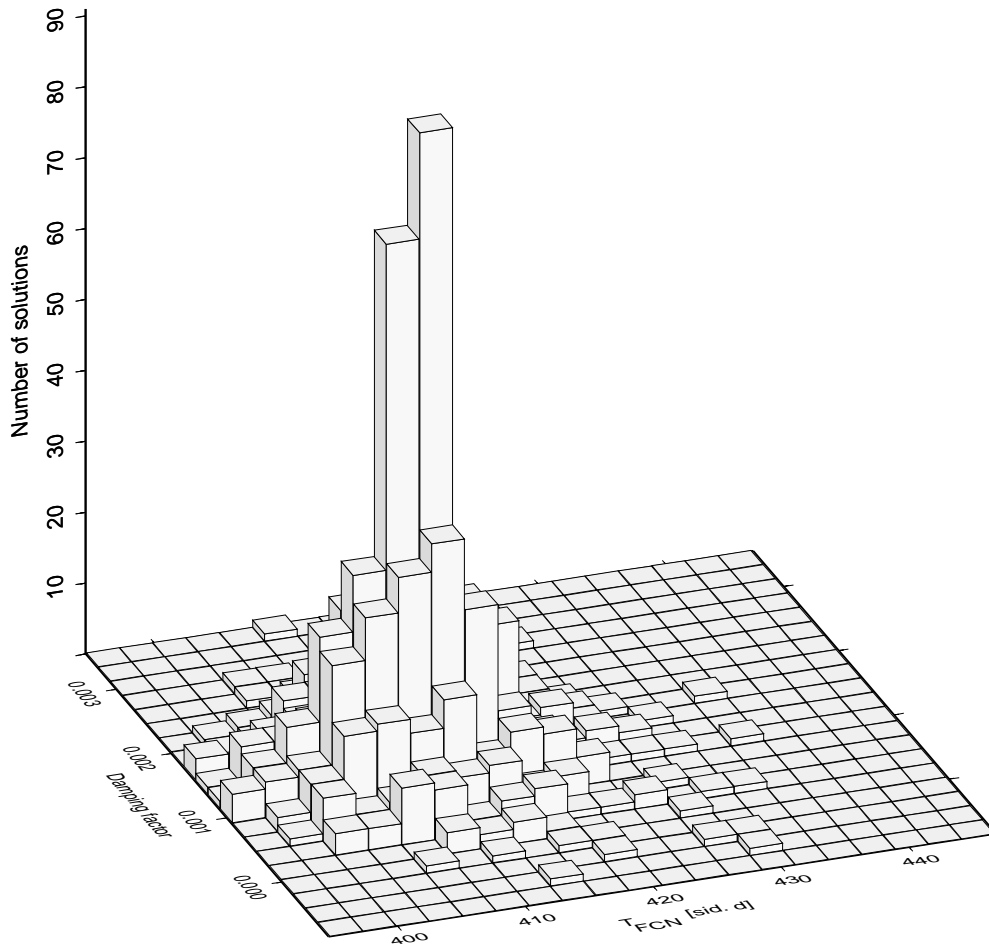


Figure 7.12: Histogram of NDFW strain results in the damping factor – resonance period plane from Monte Carlo simulations ($\tilde{\epsilon}_{Tide} = 1\sigma$ and $\tilde{\epsilon}_{Load} = 0$).

Carlo simulations a Monte Carlo analysis with the Bad Homburg gravity data [Zürn *et al.*, 1986] is also performed. With a period of the FCN of 437.0 ± 7.4 sidereal days and a Q-factor of 6300 ± 2200 the uncertainties are approximately twice respectively 18 times the BFO ones. This implies that the BFO data fit better to a NDFW model than the Bad Homburg data. It must be mentioned here that in the limited diurnal band the noise in the BFO gravity data is higher than in this Bad Homburg record, while the overall standard deviation of the BFO gravity residuals is smaller than the one of the Bad Homburg data. Furthermore the Monte Carlo uncertainty of the Bad Homburg resonance period is more than twice as large as the uncertainty from the least squares fit.

The correlation of parameters (but not the correlation of observations) is implicitly considered in the Monte Carlo simulations, since with the statistic perturbations, all solutions in the total m -dimensional parameter space are included for the Monte Carlo estimates. The projection of the solutions onto the $T_{FCN-\gamma}$ space is found in

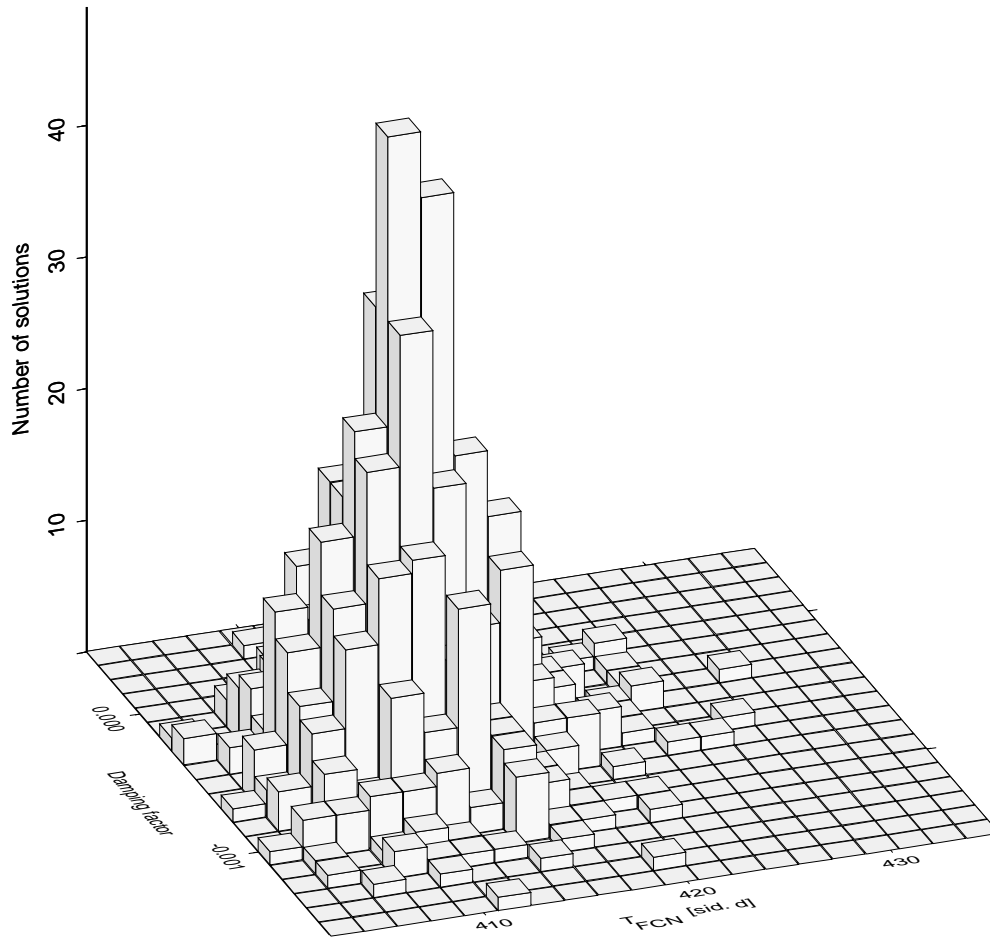


Figure 7.13: Histogram of a stack of gravity and strain of NDFW results in the damping factor – resonance period plane from Monte Carlo simulations ($\tilde{\epsilon}_{Tide} = 1\sigma$ and $\tilde{\epsilon}_{Load} = 0$).

Fig. 7.14.

The Q -factor depends heavily on the tidal constituent closest to the resonance which unfortunately happens to be also the smallest (least SNR) constituent (Fig. 5.6). The estimated Q is negative (and distinguishable from positive values) and since there is no physical explanation for a negative Q , systematic and/or random error influences could be responsible. The uncertainty of the phase of the tide ψ_1 together with the ψ_1 ocean correction which is only very poorly estimated is suspected to be the systematic error source. The inversion with fixed infinite Q shows that the amount of the Q -factor can be changed unlimited to higher values. This will be compensated by higher values of the resonance strength in the fit, so that the resonance period and its uncertainty remain almost unchanged with respect to the unconstrained inversion. In conclusion the Monte Carlo method does not allow to find a significant Q -value different from infinity and consequently a γ which is

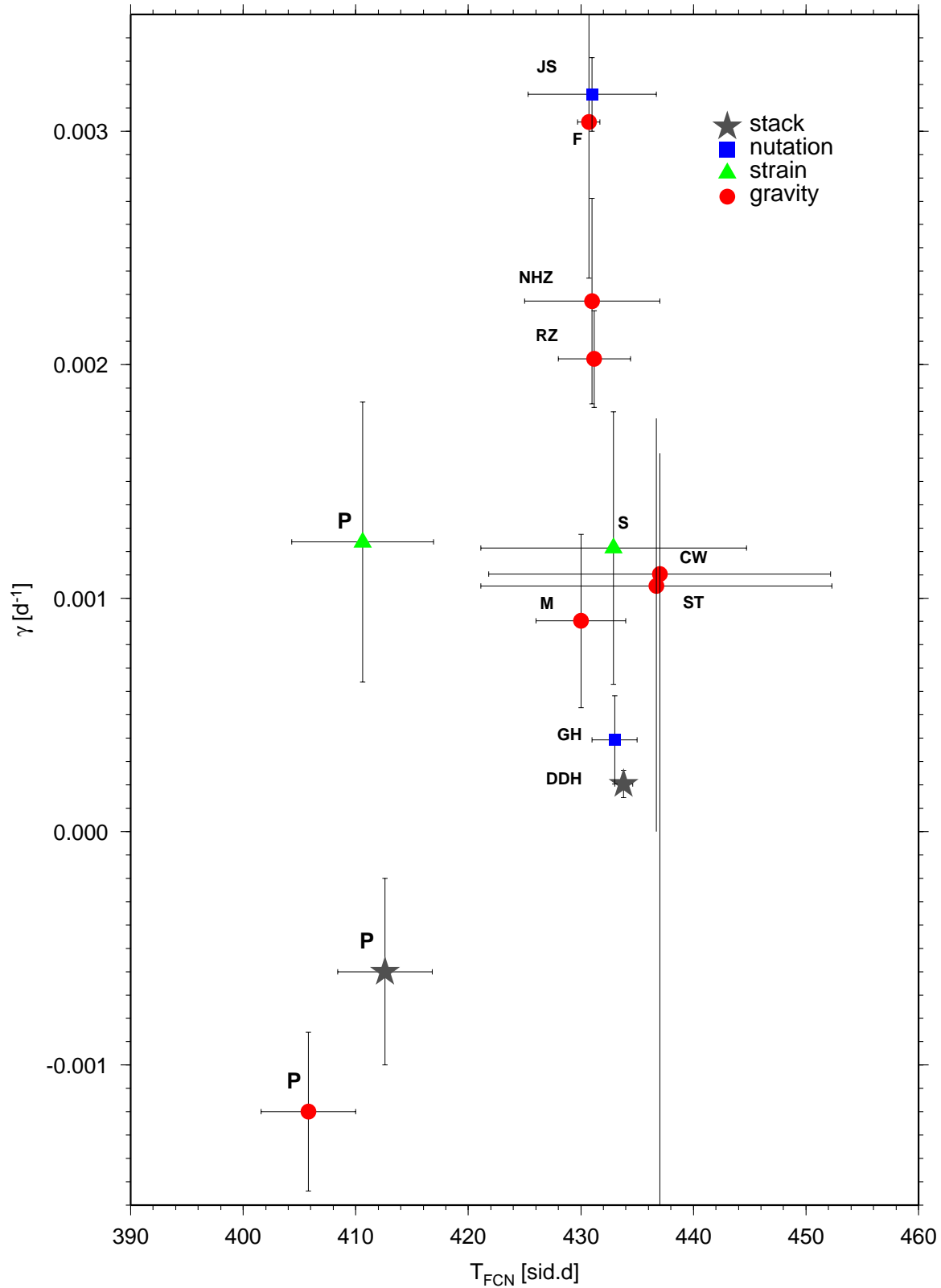


Figure 7.14: Resonance parameters T_{FCN} and γ determined in this work (labeled with **P**) and from other authors. The **P**-results are obtained by Monte Carlo simulation (section 7.3, $\tilde{\epsilon}_{Tide} = 1\sigma$ and maximum $\tilde{\epsilon}_{Load} = 0.2\tilde{L}$). The **P**-stack consists of gravity and strain data. In Table 6.2 the other used abbreviations are assigned to the underlying publications.

significantly different from 0.

Chapter 8

Investigations of air pressure

The following investigations are restricted to gravity data. The standard procedure, at least with gravity data, to take meteorologic effects into account is to simultaneously fit in the time domain the tidal model and the local air pressure to the data. This leads to a constant real regression coefficient for the entire frequency range. The gravity data contain two contributions at the S_1 -frequency and its neighbourhood: the S_1 gravity tide, which is rather small and the effect of air pressure at S_1 (see air pressure spectrum Fig. 4.2) which, with high probability, is seasonally modulated. In addition other daily influences could be present. The minimum measure to avoid contamination of the tides P_1 , K_1 , ψ_1 and ϕ_1 by unmodeled effects in S_1 is to assign to S_1 a separate group in ETERNA. To this mixture the harmonic theoretical tide S_1 and the overall air pressure is fitted. If, firstly the modulation of the S_1 in air pressure and its effect on gravity would be identical and if secondly the broad-band regression coefficient would be equal to the one for S_1 , no problem would arise. However, if one or both of these conditions are violated, leakage to the neighbouring lines relevant for NDFW analyses will occur. From previous work [eg. *Crossley et al.*, 1995] it is clear that the second condition is violated, while we do not know much about the modulations.

Below the behaviour of S_1 in air pressure is investigated, but first the dependence of the resonance parameters on the admittance between gravity and air pressure is studied.

8.1 Air pressure–gravity admittance

The local air pressure record multiplied by a priori admittance factors is subtracted and the resulting series are submitted to the tidal analysis without air pressure as additional input. Afterwards ocean corrections have been applied and the NDFW analysis have been performed in each case.

Fig. 8.1 shows the variation of the resulting δ -factors as functions of these a priori

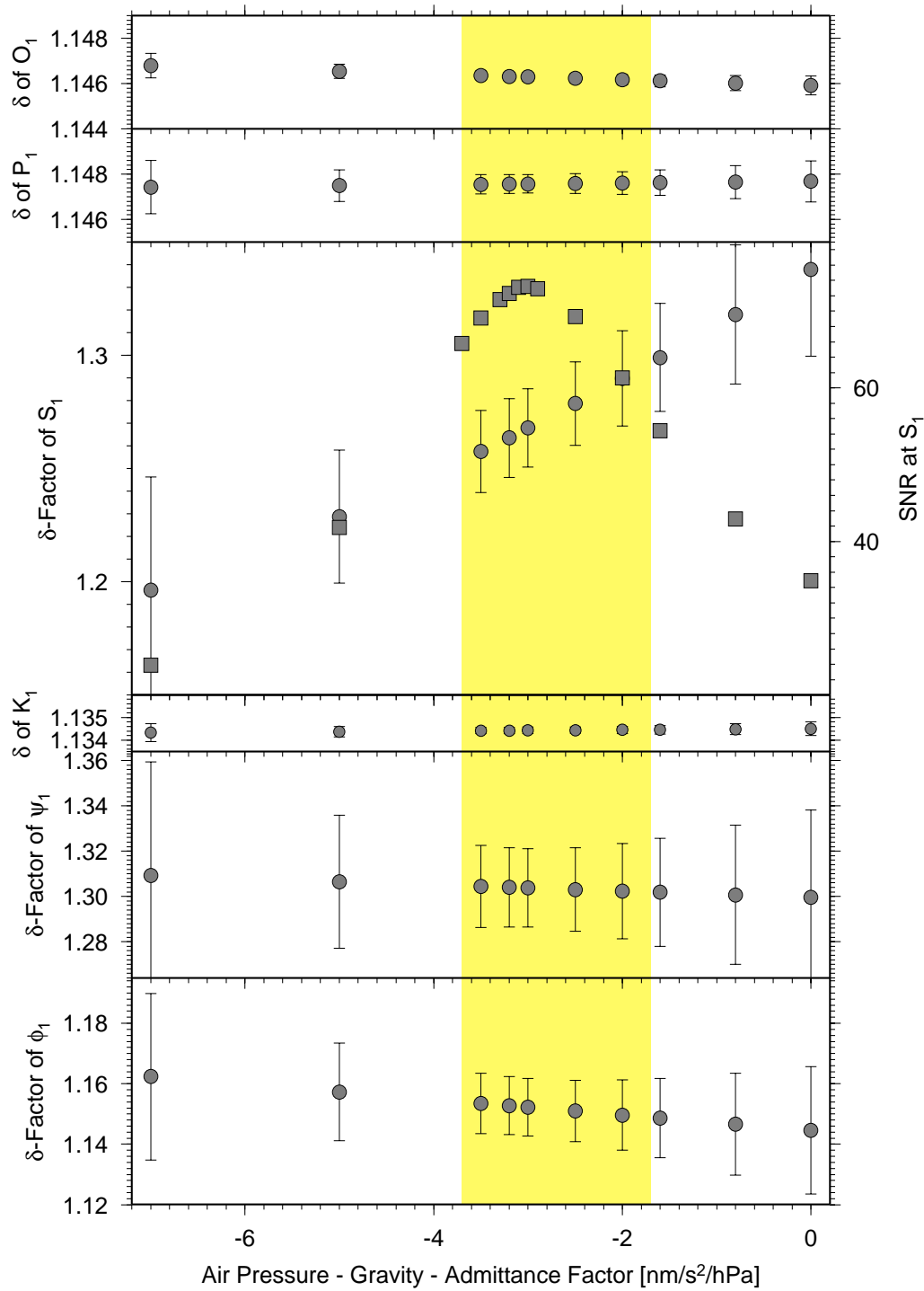


Figure 8.1: Influence of a priori air pressure–gravity admittance factors on the δ -factors of O_1 , P_1 , S_1 , K_1 , ψ_1 and ϕ_1 (before ocean load correction). The range of the admittance–factor found by *Crossley et al.* [1995] is shown as shaded area. In the third panel additionally the respective SNR of S_1 is depicted by squares.

admittances in the interval between $-7.$ and $0 \text{ nm/s}^2/\text{hPa}$. In order to reveal even faint features, the interval is chosen that large. All relevant δ -factors show nearly linear trends with the admittances. The maximum variations are: 0.08% for O_1 , 0.02% for P_1 , 11.85% for S_1 , 0.02% for K_1 , 0.73% for ψ_1 and 1.55% for ϕ_1 . According to *Merriam* [1994] these tidal constituents could all be strongly influenced by the barometric pressure due to seasonal modulations in the S_1 air pressure variations and because of that their δ -factors could be influenced by the simplified barometric pressure corrections. These effects are not as dramatic as expected, except for S_1 . However, surprisingly enough O_1 is influenced by almost 0.1%. The upper panel of Fig. 8.2 shows for the same range of air pressure–gravity admittances the FCN period obtained with both constrained and unconstrained Q . If a positivity constraint for the quality factor (+ symbols) is applied, the period of the FCN varies with the admittance by about 4.2 sid.d (Fig. 8.2 *lower panel*). Without constraint (– symbols) the range of the period variation is similar. But whereas with decreasing magnitude of the admittance factor the period of the FCN becomes longer for positive Q , for negative Q the behaviour of the FCN period is in the opposite way. When the admittance is limited to the interval $[-3.5, -1.7] \text{ nm/s}^2/\text{hPa}$ (shaded area), which is indicated by *Crossley et al.* [1995] (for the local broadband background, whereas the the effective admittance of the large-scale harmonics of the solar heating tide are between -1 and $-3 \text{ nm/s}^2/\text{hPa}$), the difference in period amounts only to 1.5 sid.d in both cases. All tidal constituents used in the NDFW analysis have their minimal errors demonstrated by the SNR at about $-3.0 \text{ nm/s}^2/\text{hPa}$. As a proxy for all waves, the SNR is shown for S_1 (Fig. 8.1 *second panel*). The minimum of the root mean square (rms) of the postfit residuals by ETERNA is located at a regression coefficient of $-3.2 \pm 0.01 \text{ nm/s}^2/\text{hPa}$ (Fig. 8.2 *upper panel*). This is a mean value in the frequency range from 0.5 to 12 cpd and therefore does not necessarily have to be the minimum of the diurnal band. But in the case here the two values coincide.

In the middle panel of Fig. 8.2 the variance reduction achieved by the NDFW fit is shown. It is calculated in terms of the resonant part of the δ -factors \tilde{R} in the following way :

$$\left(1 - \frac{\text{residual sum of squares (with reference to NDFW solution)}}{\text{total sum of squares}} \right) \cdot 100 \%$$

Two types of variance reductions are compared, the ‘weighted’ and the ‘unweighted’ variance reduction. ‘Weighted’ means that each residual is weighted with the inverse of one standard deviation of the respective tidal constituent (from tidal analysis). The trend in the δ -factors leads to higher ‘unweighted’ variance reductions (light shaded square in Fig. 8.2 *middle panel*) for increasing magnitude of the air pressure–gravity admittances. But unfortunately the larger the difference to the rms–admittance, the smaller is the SNR. The ‘weighted’ variance reductions (dark shaded square) vary only negligibly (notice the different scaling). The signal to noise ratio of the tidal analysis seems to be the only criterion to judge the different admittances. Of course, we cannot be certain, that the true admittance is included in the range of these models. But on the other hand the investigation unexpectedly

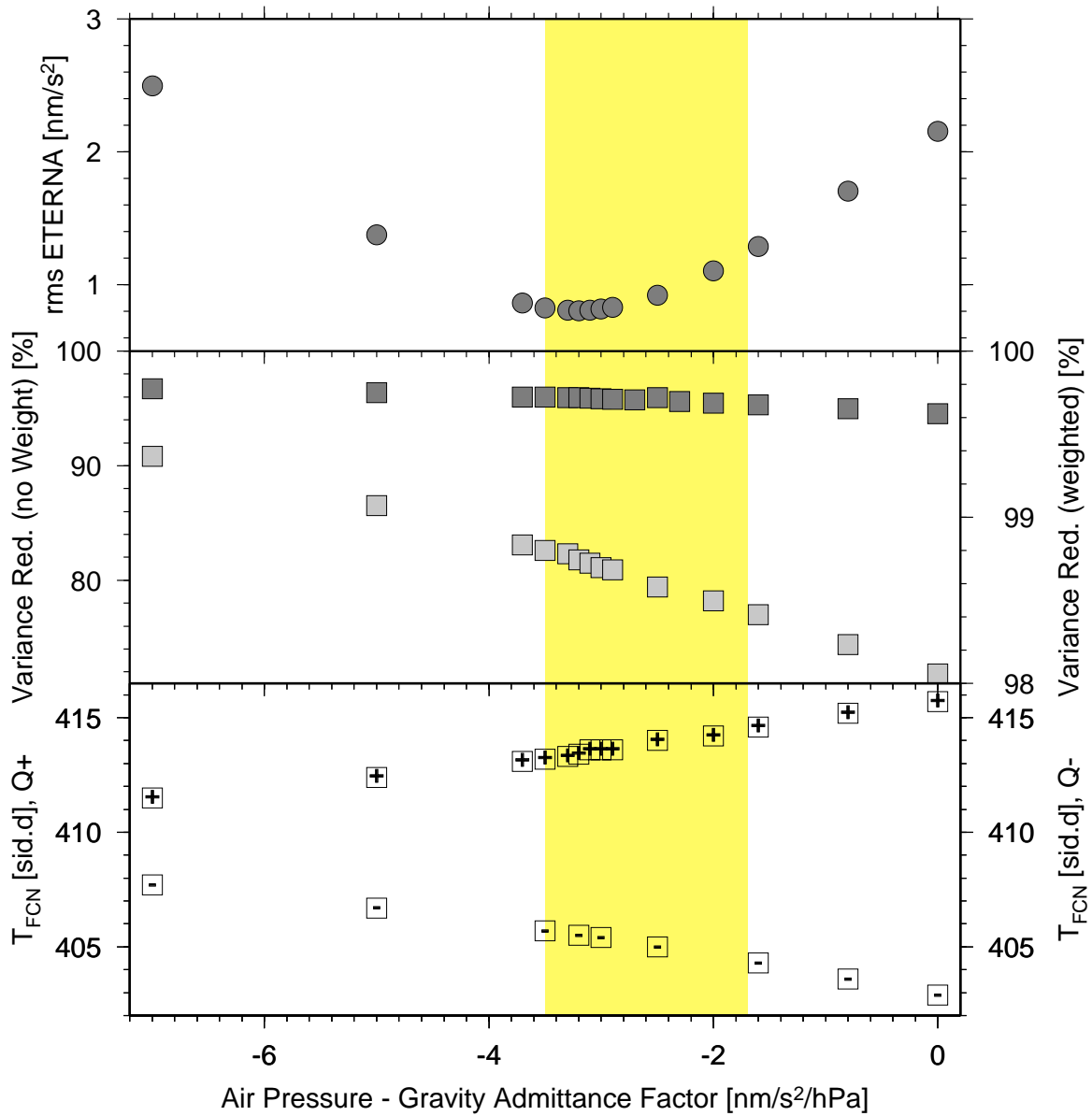


Figure 8.2: Upper panel: root mean square value of the tidal residuals from ETERNA, middle panel: ‘weighted’ (dark shaded square) and ‘unweighted’ (light shaded square) variance reduction by the NDFW analysis; lower panel: Influence of a priori air pressure–gravity admittance factors on the period of the FCN. The signs plus and minus indicate the usage of the constraint for Q (see text).

has revealed that the influence of the air pressure–gravity admittance is less than the influence of perturbations of the tidal constituents (Chapters 7.2 and 7.3). In the same context the behaviour of S_3 has been investigated in the next section.

8.2 Possible modulations of S_1

In the ter-diurnal band the nearest tidal gravity wave M_3 is sufficiently far away from S_3 . So the transfer of a harmonic pressure signal to gravity can be studied without disturbing interactions from other constituents. To reveal the properties of a harmonic signal the graphical representation of the discrete Fourier transform is used for a specific test-frequency in the complex plane, also known as ‘phasor walkout’ [Zürn *et al.*, 1995; Zürn and Rydelek, 1994]: Each individual contribution to the transform can be understood as a vector in the complex plane. The graphical summation of these individual vectors uncovers the temporal evolution of their contribution to the Fourier transform at the test-frequency. A continuing propagation of the vectors into a certain direction indicates a phase-coherent harmonic signal.

Phasor walkouts with the frequency of S_3 for our air pressure data (Fig. 8.3 *a*) and gravity residuals for different air pressure-gravity admittance factors (Fig. 8.3 *b*) have been performed. As earlier in this section to obtain the residuals for the diurnal tides the local air pressure record multiplied by a priori admittance factors has been subtracted and a tidal analysis without air pressure as additional input has been performed. Prominent are the phase reversals in April 1989 and about half a year later in the air pressure and some of the gravity residual walkouts. These reversals can be simulated easily by modeling the diurnal, seasonally modulated heating of the atmosphere due to the radiational energy input from the Sun. The synthetic time series of air pressure then consists during the winter season of short periods of low amplitude which are continuously increasing in length and amplitude towards the summer season. During night time the pressure is assumed to remain constant. A phasor walkout with the described time series subjected to a test frequency of 3 cpd shows the prominent phase reversals (Fig. 8.4). Already *Chapman and Lindzen* [1970] found a decreasing amplitude of S_3 in air pressure at the equinoxes with connected phase reversals. These phase reversals of S_3 in air pressure could also be traced to gravity. In Fig. 8.3 *b* the walkouts in gravity residuals with the corresponding air pressure-gravity admittance are depicted. The starting points are moved for reasons of presentation. The best estimate for the admittance is reached when no coherent signal is left in the residuals. Then the walkout degenerates to ‘random walk’. This is the case for an admittance factor of $2 \pm 0.25 \text{ nm/s}^2/\text{hPa}$. For higher negative factors the barometric effect is over-corrected and the air pressure signal dominates the gravity residuals. We do not know, if there is a physical justification to transfer this admittance to the diurnal band and especially to S_1 . If so, a S_1 corrected for meteorologic effects could be used as another input tide in the resonance fit. The admittance factor of 2 is not in conflict with the Crossley values and would result in a FCN period of 414.2 sid. d. Further below it is shown, that the modulation of S_1 in air pressure differs strongly from the modulation of S_3 and its modulation cannot easily be traced in the gravity data.

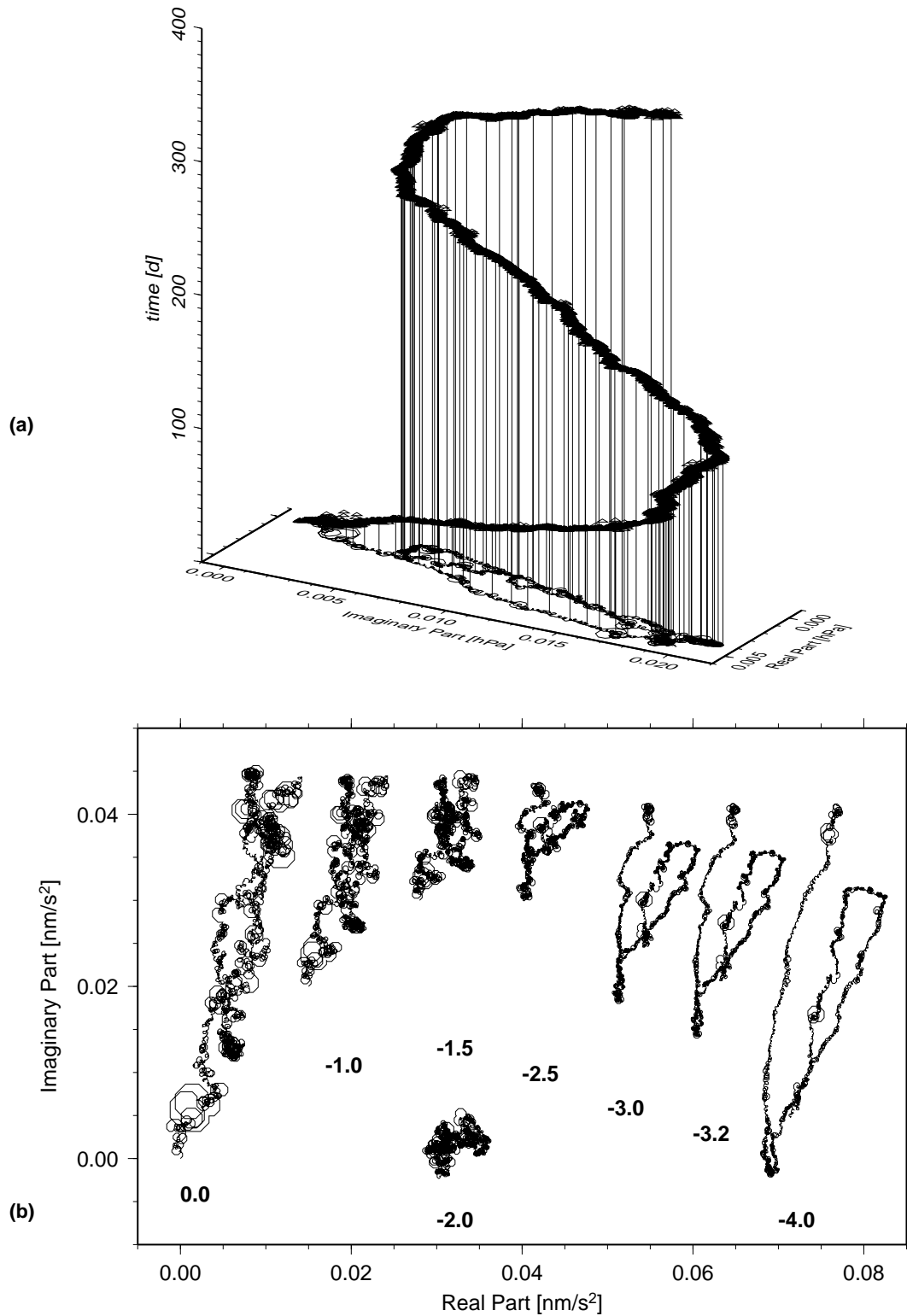


Figure 8.3: Phasor walkouts for a test-frequency of 3 *cpd* for (a) air pressure records (vertical axis: time elapsed after start) and (b) ETERNA gravity residuals with a priori air pressure-gravity admittance factors as indicated.

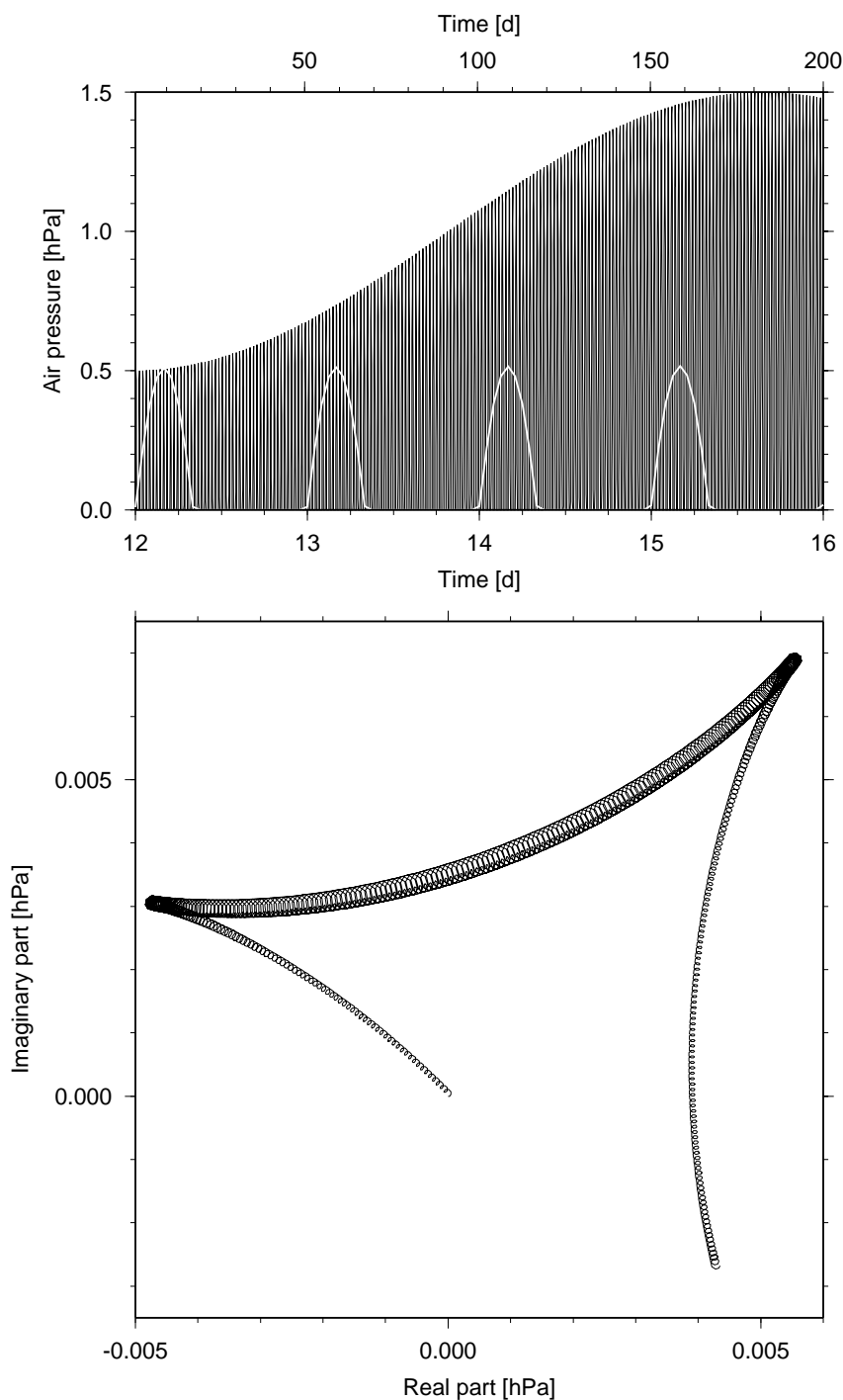


Figure 8.4: Simple model for the thermal induced pressure variations due to the radiational energy input from the Sun. The upper panel shows in white a detail of the air pressure time series in higher resolution and in black about half the series length with seasonal modulation visible. Lower panel: the phasor walkout resulting from the synthetic time series above (extended to 13 month length) subjected to a test frequency of 3 *cpd* with the starting point at the coordinate origin.

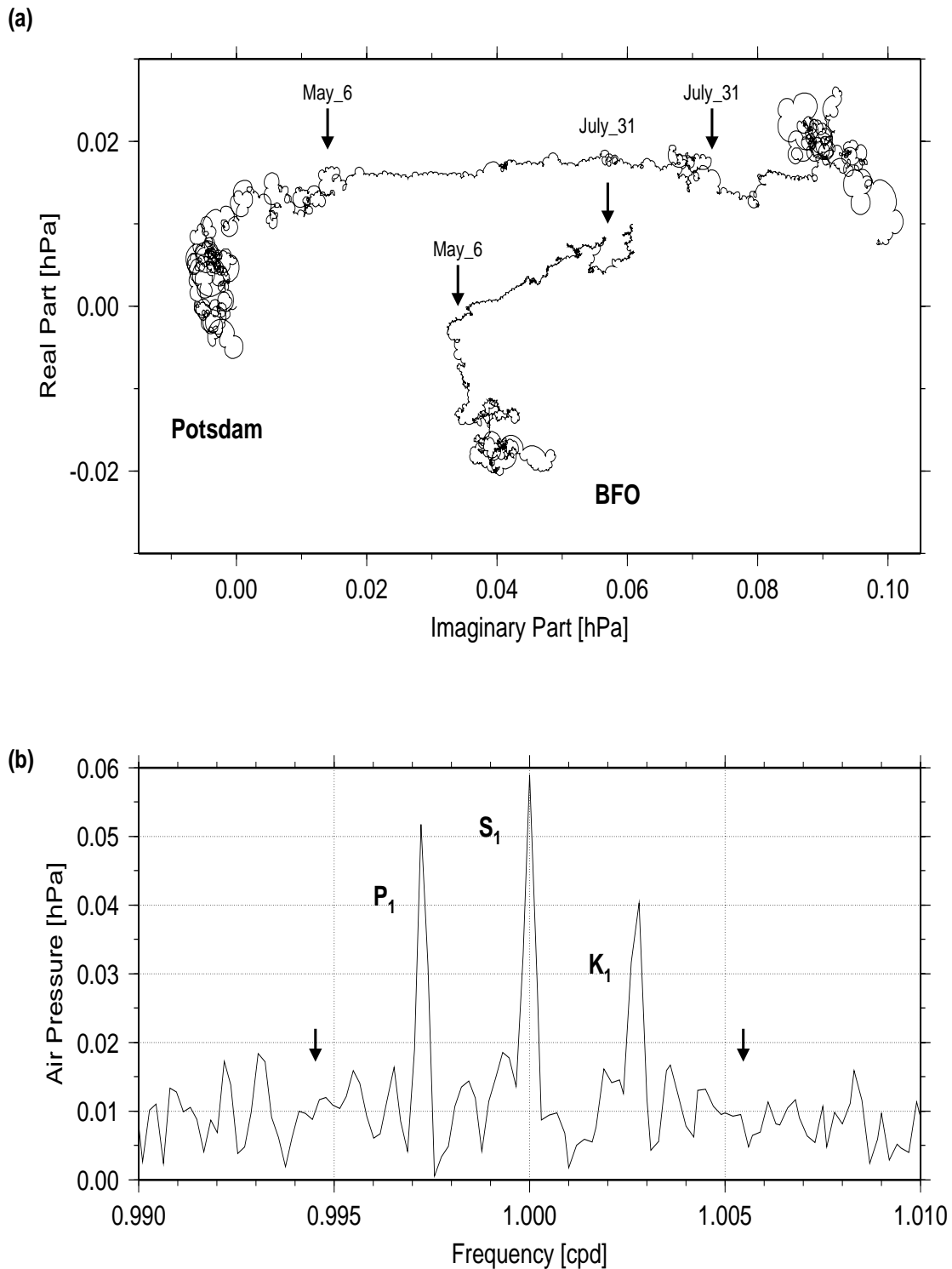


Figure 8.5: (a) Phasor walkout for S_1 in air pressure records from BFO and Potsdam for a 398 days period. The origin for BFO was moved to $(0.04, -0.02)$ hPa for better presentation. The small arrows on both phasors mark the coherent period which begins on May 6, 1989 and lasts for 86 days. (b) Amplitude spectrum of an air pressure time series from Potsdam with 16 years length, beginning on September 1, 1974. The small arrows mark the frequencies of the constituents π_1 (0.99452 cpd) and ψ_1 (1.00547 cpd).

To study the behaviour of S_1 phasor walkouts for its frequency have also been performed. In Fig. 8.5 the walkouts for S_1 for air pressure records at BFO and Potsdam (52.381°N, 13.068°E, 81 m elevation) are compared. Both walkouts clearly demonstrate that the S_1 oscillation is not excited all the time or that its phase varies frequently with time. There is only a 86 days period from May 6, 1989 to July 31, 1989 when S_1 is dominant and has relatively constant phase. *Siebert* [1961] found a latitude dependent amplitude of the global solar tide S_1 in air pressure measured on the ground. According to his results the amplitude of S_1 at Potsdam should be 79% of the one at BFO. But a S_1 amplitude for the 398 days series at Potsdam (0.1635 *hPa*) is found which is 2.65 times the one at BFO (0.0617 *hPa*). This can also be seen in the phasor walkouts. The magnitude of the Fourier transform in this presentation is the vector from the origin of the walkout to the end point. But when meteorological quantities from two stations are compared also the different latitude, altitude and environment have to be taken into account. The topographic setting of the two station is totally different, BFO is located in a mountain range of South-West-Germany, whereas the station Potsdam is situated in the northern German plains (Fig. 2.1).

For better resolution of the diurnal tidal band also air pressure readings of 16 years length from Potsdam have been Fourier transformed. In this times series the 398 days period (Fig. 8.5*b*) is included. In the 16 years series the S_1 amplitude is estimated to 0.059 *hPa* which is close to the BFO value. The phasor walkout for S_1 reveals that in the short time period S_1 is more dominant than in the long series on average. The annual modulations of S_1 at the frequencies of P_1 and K_1 attain 5/6 respectively 2/3 of the amplitude of the diurnal carrier frequency, whereas semi-annual modulations at the frequencies of π_1 und ψ_1 do not emerge from the background noise.

Summarizing, the S_1 in air pressure behaves strongly non-harmonic, and could be additionally annually modulated like the S_1 at Potsdam. But the behaviour of the S_1 signal in gravity does not have to be equal to the signal in air pressure. Nevertheless it appears that the influence of air pressure on the FCN period is less than the influences resulting from the uncertainties of the tidal parameters.

Chapter 9

Interpretation with respect to CMB ellipticity

With the results of the NDFW analysis of the last two chapters at hand the final step is to interpret the obtained parameters. The resonance frequency determined in this work and the publications in Table 6.2 have a prominent, but differing NDFW frequency shift in common (corresponding to 60 *sid. d* at most and 30 *sid. d* respectively), which leads to higher frequencies compared to an earth model in hydrostatic equilibrium [Wahr, 1981; Dehant, 1987]. The figure of hydrostatic equilibrium is represented by surfaces of uniform density and uniform elastic properties, given by balancing gravitational and centrifugal forces in the absence of external forcing. This results in a difference of the polar and equatorial radius of the fluid core of about 9 km (moments of inertia from Dickey [1995], see Glossary) on the basis of a mean fluid core radius of 3480 km (PREM [Yoder, 1995]). Neuberg *et al.*, [1990] investigated the relative importance of the terms in equation 5.18 with regard to the frequency shift. The individual terms have the following implications:

- A higher dynamic ellipticity of the CMB with respect to the hydrostatic case would lead to stronger inertial coupling and consequently to a higher NDFW frequency. With excess flattening of the CMB by a few hundred meters it is possible to explain the total amount of the frequency shift.
- The effect of elasticity of the mantle (compared to rigid behaviour) is the instantaneous elastic reaction of the shape of the CMB to the pressure field due to the NDFW. The small uncertainty in the average of the seismologically determined elasticity of the mantle can only explain approximately 1/10 of the frequency shift. Anelasticity of the mantle would even decrease the NDFW frequency.
- Although core viscosity is only poorly constrained no value within the extreme estimates can explain more than a small fraction of the frequency shift.

- Substituting one extreme estimate of the electromagnetic coupling by the other extreme shows only negligible effects on the resonance frequency.

In conclusion they found that the shift in the NDFW frequency can most easily be explained with excess ellipticity of the CMB. For an Earth in hydrostatic equilibrium the decrease of the ellipticity of the Earth's stratification with depth is a consequence of increasing density. So the dynamical ellipticity under the equilibrium assumption is about 1/299 for the free surface, whereas at the CMB it is reduced to about 1/389 [Dickey, 1995]. Flattening of the CMB beyond the hydrostatic equilibrium figure provides important constraints for viscosity in the mantle and thus mantle convection [Forte *et al.*, 1994]. The core resonance is not influenced by possibly existing topography (where the term topography is here restricted to structure of harmonic degree higher than $l = 2$), what implies in turn that topography cannot be deduced from NDFW data. Effects of all other possibilities listed above are neglected in the following. Then from equation 5.18 follows:

$$\Delta\sigma_{NDFW} = -\Omega \frac{A}{A^M} \Delta\alpha^C \quad (9.1)$$

The excess flattening $\Delta\alpha^C$ can be expressed in terms of moments of inertia:

$$\Delta\alpha^C = \frac{\Delta C^C}{A^C} - \frac{C^C \Delta A^C}{(A^C)^2} \approx \frac{\Delta C^C - \Delta A^C}{A^C} \quad (9.2)$$

A deviation from the hydrostatic figure of the core represented by $R_0(\theta)$ results in the following corresponding perturbations in the moments of inertia:

$$\Delta C^C = \int_{\lambda=0}^{2\pi} \int_{\theta=0}^{\pi} \rho_0 R_0^4(\theta) \Delta R^C \sin^3 \theta d\theta d\lambda \quad (9.3)$$

$$\Delta A^C = \int_{\lambda=0}^{2\pi} \int_{\theta=0}^{\pi} \rho_0 \left[R_0^4(\theta) - R_0^4(\theta) \sin^2 \theta \cos^2(\lambda - \lambda_0) \right] \cdot \sin \theta \Delta R^C d\theta d\lambda \quad (9.4)$$

with θ and λ being co-latitude and longitude. The dynamical flattening is thus dependent on the density ρ_0 of the core at the CMB and the aspherical or non-hydrostatic figure of the core represented by the function $\Delta R^C(\theta, \lambda)$ which can be described by spherical harmonics $\bar{P}_l^m(\theta)$:

$$\Delta R^C(\theta, \lambda) = \sum_{l=0}^L \sum_{m=0}^l [C_l^m \cos m\lambda + S_l^m \sin m\lambda] \bar{P}_l^m(\theta) \quad (9.5)$$

with the coefficients of the spherical harmonic expansion C_l^m and S_l^m and the normalization

$$\bar{P}_l^m(\theta) = \left[(2 - \delta_{m0}) (2l + 1) \frac{(l - m)!}{(l + m)!} \right]^{\frac{1}{2}} P_l^m(\cos \theta) \quad (9.6)$$

The deviation of the polar radius from an earth model in hydrostatic equilibrium is then represented by $\Delta R^C(\theta = 0^\circ, \lambda)$. It can be shown that the coefficient C_2^0 is the most sensitive with respect to CMB ellipticity [Neuberg, 1987]. The relevant part of $\Delta R^C(\theta, \lambda)$ reduces then to

$$\Delta R^C(\theta) = C_2^0 \bar{P}_2^0(\theta) \quad (9.7)$$

Neuberg [1987] found a perturbation of the polar core radius $\Delta R^C(\theta = 0^\circ)$ of -250 and -350 m for an elastic and anelastic mantle respectively. This was achieved by forward modelling. For a constant density ρ_0 (valid for the core at the CMB) and variable C_2^0 Equation 9.3 and subsequently Equation 9.2 were solved and the obtained α^C were compared to the result from the NDFW analysis. Since the frequency shift of this work is about twice as large, as the one of Neuberg [1987], under equivalent prerequisites a value for $\Delta R^C(\theta = 0^\circ)$ of -500 to -700 m must be expected.

9.1 CMB ellipticity from other geophysical data

Other observations which allow to constrain the ellipticity of the CMB come from three main areas:

- Nutation observations. As is explained in Chapter 5.2 the core resonance has two manifestations the wobble and the nutation. NDFW and FCN are two aspects of the same rotational mode of the Earth. The nutation of the rotation axis in space can be verified by astronomical measurements with VLBI (explained in the box below) [eg. Herring et al., 1991]. Gwinn et al. [1986] determined a resonance period of 433.2 sid.d with small error bars of 2 sid.d which they interpreted as $\Delta R^C(\theta = 0^\circ) = -328 \pm 76$ m.
- Travel-time residuals of seismic body-waves that have interacted with the CMB. Morelli and Dziewonski [1987] investigated phases of waves reflected at the core (PcP) as well as waves refracted through the CMB (PKP). Their insignificant results suggest a diminished ellipticity of the CMB. Doornbos and Hilton [1989] additionally used reflections from the bottom side of the core (PKKP phases), this resulted in reduced topography relative to the former, but a $\Delta R^C(\theta = 0^\circ)$ of -1480 m. Travel-times of body-waves are mostly suited to constrain CMB topography at intermediate and short wavelengths (equivalent to harmonic degree $l > 2$) due primarily to the highly uneven sampling of the CMB by the associated ray-paths. This implies a potential for aliasing of short wavelength topography into estimates of long wavelength topography. The most important point is that the observable phase with the shortest wavelength is at least an order of magnitude larger than the expected reduction of the polar core radius.

- Splitting of seismic free oscillations as summarized with so called structure coefficients are best suited to constrain long wavelength structure ($l = 2$). One reason is that normal modes are standing waves which involve the entire globe. The components of a multiplet with low harmonic degree l is influenced by the whole earth structure and not just by the structure underneath the great circle connecting source and receiver as with body-waves and high-frequency surface waves. A detailed examination follows in the next section.

A possible explanation for the excess ellipticity of the core could be dynamic stresses exerted on the CMB by the thermal convective flow of the mantle. Under this assumption *Forte et al.* [1994] have performed viscous flow calculations to determine the CMB topography. Combining data sets of different origin may compensate the deficiencies of systematic effects in individual data sets. Their basis was a 3-dimensional elastic structure derived from seismic data, including normal mode splitting estimates and geodynamic data consisting of long-wavelength free-air gravity anomalies and FCN periods. Excess flattening of the CMB equivalent to $\Delta R^C(\theta = 0^\circ) = 190\text{ m}$ is consistent with their data.

Very Long Baseline (Radio) Interferometry (VLBI)

With very long baseline interferometry the temporal behavior in orientation of terrestrial baselines relative to extragalactic sources of radiowaves can be investigated.

Radio interferometry demands precise timing of radio signals from distant stellar sources at widely spaced earth-bound receivers. The observed data, dual-frequency-band interferometric group delays, allow then to determine the positions of the sources. Since the sources are assumed to be known and fixed in space, the temporal variation in baseline orientation can therefore be estimated. Knowing that a large part of the changes in orientation of the baselines are due to rotational motions, the nutation of the Earth's rotation axis can then be deduced from this kind of data.

9.1.1 Normal mode splitting and CMB ellipticity

In this subsection the resolving power of normal mode splitting data with respect to CMB ellipticity is investigated.

Free oscillations including spheroidal and toroidal normal modes are excited by large earthquakes and supply information to constrain the large-scale mechanical structure of the Earth. Observations of normal mode frequencies allow to infer details of the density distribution inside the Earth. The radial eigenfunctions of different modes are sensitive to different depth regions of the Earth. Modes which are sensitive to the deep interior of the Earth, the core region, have a typically high

quality factor and a low harmonic degree l . These modes sample the Earth like PKIKP phases.

The frequency ω_k of a spheroidal normal mode ${}_nS_l$ or toroidal normal mode ${}_nT_l$ (with angular degree l and overtone number n which represents the nodes of the radial eigenfunctions) is degenerate for a spherically symmetric, non-rotating Earth. Rotation and hydrostatic ellipticity remove this degeneracy. So the degenerate multiplet splits into $2l + 1$ singlets with the frequencies ω_m

$$\omega_m = \omega_k \left(1 + a + mb + m^2c \right) \quad (9.8)$$

where $m = -l, \dots, l$, a and c are ellipticity splitting parameters and b is the rotational splitting parameter. The multiplet degenerate frequency ω_k represents the properties of a spherically averaged Earth, whereas the singlet frequencies of the split multiplet are non-linearly related to aspherical earth structure.

The splitting characteristics for an earth model with general aspherical structure of the k th multiplet in representation of the m singlets are described by the splitting matrix

$$\mathbf{H}_{mm'}^k = \omega_k \left(a + mb + m^2c \right) \delta_{mm'} + \sum_s \gamma_s^{mm'} {}_k c_s^t \quad (9.9)$$

where $\gamma_s^{mm'}$ represent 'selection rules' [eg. *Widmer, 1991*] which limit the kind of aspherical structure to which an isolated multiplet is sensitive. Normal-mode splitting due to rotation and hydrostatic ellipticity may be calculated for a reference earth model. The remaining signal in observations is then due to 3-dimensional earth structure. For small perturbations the structure coefficient ${}_k c_l^m$ of the k th multiplet and for structure of harmonic degree l and azimuthal order m is linearly related to earth structure [*Woodhouse and Dahlen, 1978*]. Both volumetric and boundary perturbations contribute to the complex structure coefficient

$$\begin{aligned} {}_k c_s^t = & \int_0^R \left[{}_k R_s(r) \delta \rho_s^t(r) + {}_k K_s(r) \delta \kappa_s^t(r) + {}_k M_s(r) \delta \mu_s^t(r) \right] r^2 dr \\ & - \sum_i r_i^2 h_{si}^t {}_k B_{si} \end{aligned} \quad (9.10)$$

with the volumetric perturbations of density, bulk and shear modulus $\delta \rho_s^t$, $\delta \kappa_s^t$ and $\delta \mu_s^t$ respectively. R is the radius of the Earth. The boundary perturbations are represented by h_{si}^t . The kernels ${}_k R_s(r)$, ${}_k K_s(r)$, ${}_k M_s(r)$ and ${}_k B_{si}$ can be computed [*Woodhouse and Dahlen, 1978*] for a given reference earth model. They describe the sensitivity of a mode to the corresponding perturbation as a function of depth.

For a simple estimation only the influence of boundary perturbations is considered. The variation in the structure coefficient is then only dependent on the topography of the considered i th interface. Here the only interface of interest is the CMB with exclusively its second degree harmonic structure ($l = 2$). Otherwise mantle and core are homogenous. The structure coefficient for the k th multiplet due to a boundary perturbation h_2^0 at the CMB is then

$${}_k c_2^0 = (R^C)^2 h_2^0 {}_k B_2 \quad (9.11)$$

The CMB topography h_2^0 corresponds to a deviation of the polar core radius of

$$\Delta R^C (\theta = 0^\circ) = h_2^0 Y_2^0 (\theta) \quad (9.12)$$

with the fully normalized second degree spherical harmonic

$$Y_2^0 (\theta) = \sqrt{\frac{5}{4\pi}} \left(\frac{3}{2} \cos^2 \theta - \frac{1}{2} \right) \quad (9.13)$$

The kernels ${}_k B_2$ are calculated for the spherical symmetric earth model 1066A [Gilbert and Dziewonski, 1975]. For a fixed hypothetical h_2^0 it is possible to predict the structure coefficients for this earth model for every mode. Here a perturbation of the second zonal degree CMB topography $h_2^0 = 400 \text{ m}$ which is equivalent to a reduction of the polar core radius $|\Delta R^C| (\theta = 0^\circ) = 252 \text{ m}$ is chosen. This boundary perturbation represents an intermediate value from the literature and should yield a reasonable estimate for the second degree harmonic structure coefficient.

In Tables 9.1 and 9.2 (column iv) a summary of published c_2^0 structure coefficients estimated for normal modes excited by the Macquarie Rise 1989, the Great 1994 Bolivia and Kuril Islands earthquakes [He and Tromp, 1996; Widmer et al., 1992(a)] are listed. All these modes display finite energy densities at the CMB and additionally possess non-vanishing energy densities at the surface to be observable. The corresponding predicted structure coefficients for a CMB topography of $h_2^0 = 400 \text{ m}$ according to Equation 9.11 are compared.

Although for a large number of 66 core sensitive modes the structure coefficient c_2^0 could be estimated, the combined information contained in these coefficients still cannot compete with the tight constraints that are being placed on the CMB ellipticity by estimates of the NDFW/FCN period. The estimated structure coefficient c_2^0 exceeds the theoretically predicted value c_{400m} for almost all modes by several orders of magnitude. From Equation 9.11 it follows that the observed modes in Tables 9.1 and 9.2 prefer larger h_2^0 CMB topography. In no case does the expected signal of a CMB ellipticity equivalent to $h_2^0 = 400 \text{ m}$ exceed the observational uncertainty. The results of this normal mode analysis do not seem to be appropriate to constrain an excess ellipticity of the CMB with a resolution comparable to observations of the core resonance in tides and nutations.

Table 9.1: Summary of mode constraints for ellipticity of the CMB. The individual columns are: (i) mode name, (ii) CMB boundary kernel $(R^C)^2 B_2$. The column labeled c_{400m} gives the predicted c_2^0 structure coefficient for a hypothetical CMB topography $h_2^0 = 400m$. Column (iv) gives the observed structure coefficients with observational uncertainties (column (v)). Column (vi) gives the h_2^0 CMB topography needed to produce the observed structure coefficients (column (iv)), assuming an otherwise homogeneous mantle and core. Finally column (vii) gives the ratio of the c_2^0 structure coefficient predicted for $h_2^0 = 400m$ over the observational uncertainty.

Mode	$(R^C)^2 B_2$ [$\frac{\mu Hz}{km}$]	c_{400m} [μHz]	c_2^0 [μHz]	σ [μHz]	h_2^0 [km]	$ c_{400m}/\sigma $ [%]
${}_0S_3$	-0.035	-0.014	0.83	0.69	-24	2.0
${}_0S_4$	-0.133	-0.053	1.92	0.41	-14	13.0
${}_0S_5$	-0.210	-0.084	1.92	0.38	-9	22.0
${}_0S_6$	-0.255	-0.102	1.44	0.35	-5	28.9
${}_0S_7$	-0.260	-0.104	1.17	0.29	-4	35.7
${}_0S_8$	-0.220	-0.088	1.18	0.37	-5	24.1
${}_0S_9$	-0.150	-0.060	-1.54	0.42	10	14.2
${}_0S_{10}$	-0.087	-0.035	-2.89	0.48	33	7.2
${}_1S_2$	-0.052	-0.021	-0.09	1.15	1	1.8
${}_1S_3$	-0.020	-0.008	0.14	0.35	-7	2.3
${}_1S_4$	-0.003	-0.001	0.60	0.65	-317	0.1
${}_1S_5$	0.020	0.008	0.75	0.78	38	1.0
${}_1S_6$	0.020	0.008	2.23	1.39	113	0.6
${}_1S_7$	-0.050	-0.020	3.51	1.18	-71	1.7
${}_1S_8$	-0.180	-0.072	4.84	1.06	-26	6.8
${}_1S_9$	-0.345	-0.138	6.52	1.66	-18	8.3
${}_1S_{10}$	-0.505	-0.202	7.46	2.08	-14	9.7
${}_2S_3$	-0.050	-0.020	8.59	0.29	-173	6.7
${}_2S_4$	0.013	0.005	0.49	0.94	39	0.5
${}_2S_5$	0.035	0.014	2.35	2.38	69	0.6
${}_2S_6$	0.020	0.008	-1.32	1.08	-67	0.7
${}_2S_8$	0.010	0.004	-2.23	0.72	-211	0.6
${}_3S_1$	-0.245	-0.098	0.33	0.29	-1	33.4
${}_3S_2$	-0.125	-0.050	14.54	0.67	-116	7.4
${}_3S_8$	0.188	0.075	5.26	1.50	28	5.0
${}_4S_1$	-0.130	-0.052	1.43	0.51	-11	10.1
${}_4S_2$	0.025	0.010	0.02	0.46	1	2.1
${}_4S_3$	-0.015	-0.006	0.32	0.43	-23	1.3
${}_4S_4$	0.165	0.066	-0.17	1.36	-1	4.9
${}_5S_3$	0.182	0.073	2.75	1.62	15	4.5
${}_5S_4$	-0.065	-0.026	-0.38	0.49	5	5.3
${}_5S_5$	-0.080	-0.032	-0.27	0.67	3	4.8

Table 9.2: Continuation of previous table.

Mode	$(R^C)^2 B_2$ [$\frac{\mu Hz}{km}$]	c_{400m} [μHz]	c_2^0 [μHz]	σ [μHz]	h_2^0 [km]	$ c_{400m}/\sigma $ [%]
${}_5S_6$	-0.063	-0.025	-0.44	0.67	6	3.8
${}_5S_7$	-0.003	-0.001	-1.11	0.69	727	0.1
${}_5S_8$	0.125	0.050	0.84	1.33	6	3.7
${}_5S_{12}$	0.080	0.032	4.86	1.53	60	2.1
${}_6S_3$	-0.242	-0.097	17.59	0.95	-72	10.2
${}_7S_4$	0.282	0.113	4.70	2.59	16	4.4
${}_7S_5$	-0.140	-0.056	5.99	0.66	-43	8.4
${}_7S_6$	-0.280	-0.112	2.83	0.85	-10	13.1
${}_7S_7$	-0.133	-0.053	4.46	0.99	-33	5.3
${}_8S_1$	-0.175	-0.070	3.86	0.22	-22	31.1
${}_8S_5$	-0.205	-0.082	13.92	0.89	-68	9.2
${}_8S_7$	0.430	0.172	5.95	0.81	13	21.3
${}_9S_3$	-0.233	-0.093	13.08	1.49	-56	6.3
${}_9S_{14}$	0.040	0.016	0.24	2.16	6	0.7
${}_{11}S_4$	-0.328	-0.131	16.86	0.32	-51	40.8
${}_{11}S_5$	-0.302	-0.121	13.18	1.13	-43	10.7
${}_{12}S_8$	0.028	0.011	1.18	1.07	43	1.0
${}_{12}S_{12}$	-0.393	-0.157	6.73	1.72	-17	9.2
${}_{13}S_1$	-0.310	-0.124	19.80	1.53	-63	8.1
${}_{13}S_2$	-0.328	-0.131	23.04	0.53	-70	24.6
${}_{13}S_3$	-0.383	-0.153	14.31	0.50	-37	30.9
${}_{16}S_5$	-0.212	-0.085	26.61	0.99	-124	8.6
${}_{16}S_7$	-0.390	-0.156	14.65	2.12	-37	7.3
${}_{17}S_1$	-0.542	-0.217	-2.84	4.21	5	5.1
${}_{17}S_{12}$	-0.388	-0.155	15.09	8.24	-39	1.9
${}_{17}S_{13}$	-0.757	-0.303	12.41	1.47	-16	20.6
${}_{18}S_3$	-0.427	-0.171	18.82	0.95	-44	18.0
${}_{18}S_4$	-0.435	-0.174	22.74	0.90	-52	19.4
${}_{21}S_6$	-0.440	-0.176	30.56	3.36	-69	5.2
${}_{21}S_7$	-0.605	-0.242	26.18	3.94	-43	6.2
${}_{21}S_8$	-0.603	-0.241	25.36	3.44	-42	7.0
${}_{23}S_4$	-0.632	-0.253	24.35	1.84	-38	13.8
${}_{23}S_5$	-0.700	-0.280	22.99	1.84	-32	15.2
${}_{27}S_1$	-0.828	-0.331	24.97	3.97	-30	8.3

Chapter 10

Conclusions and outlook

The purpose of this work was to determine the characteristics of the core resonance. This was accomplished by analyzing different kinds of tidal registrations with respect to tidal admittances. After applying ocean load corrections based on the new altimeter data from the TOPEX/POSEIDON mission to the tidal parameters, a linearized least squares inversion has then been performed with the resonant part of the tidal parameters for the retrieval of the NDFW parameters. Inversions have been performed with digital gravity, strain and tilt measurements at the station BFO. Two of the data sets analyzed here, gravity and strain, are of very high quality and are therefore well suited for retrieval of NDFW properties from them. The tilt data do not belong into this class, as is demonstrated by the insignificant core resonance results for tilt observations. Probably the noise level is simply too high for the small geophysically relevant signal, while in the case of strain the higher noise is compensated by the higher geophysical significance (Equation 3.21 in Chapter 3) or cavity effects are not frequency independent.

For the data set with the best quality, namely gravity, an equivalent FCN period of $T_{FCN} = 405.8 \pm 4.2 \text{ sid. d}$ was obtained. The stack of tidal parameters of gravity and strain results in $T_{FCN} = 412.6 \pm 4.2 \text{ sid. d}$. In this joint inversion (similar to the other cases) reasonable resonance strengths of $A = -0.57 \pm 0.17$ and $B = -0.04 \pm 0.17$ for gravity, and $A = -6.14 \pm 0.22$ and $B = -0.50 \pm 0.22$ for strain, respectively, could be determined (Tables 6.1 and 7.3). All Q estimates of this work are very high and lie in the ranges of -5000 to -11000 and 5000 to $+\infty$, respectively. Very high Q are also typical for FCN analyses of VLBI data. However, the FCN periods of the different analyses fall in the range 405 to 413 *sid. d*, well below the results ($> 1\sigma$) of other authors from tidal and nutational data sets. Comprehensive statistical investigations have been undertaken, because the resonance period estimated in this work differs significantly from the majority of other publications. Particularly investigated was the error propagation from the measurements to the uncertainties in the parameters. It turns out that the uncertainties in the tidal admittances are the most serious error source in our data sets, and also in the well known excellent Bad Homburg gravity data. Therefore it can be safely concluded, that

this is the case for all tidal data sets. Considering the small standard deviation of $2sid.d$ for the nutation results for T_{FCN} by *Gwinn et al.* [1986] it appears, that the tidal measurements cannot compete with nutation measurements by VLBI for the accuracy of NDFW parameters. However, we really cannot judge the quality of this low error estimate.

Special efforts were undertaken to study the air pressure–gravity admittance. In the presented NDFW inversions the air pressure influence does not appear to be as crucial as generally expected, so the largest uncertainties are contributed by the tidal admittances. The correction for air pressure effects in the diurnal band is crucial, but yet there is no perfect method to deal with this. Modulation of S_1 in barometric pressure is clearly present and it is, for a given data set of a few years at most, not necessarily a clear seasonal modulation in the latitudes of BFO and Potsdam. Studies of S_3 do not help for S_1 either. The modulation leads to systematic effects in the tidal admittances for sure due to leakage from an imperfectly modeled S_1 to the neighbouring tides. However, from our results it appears that these effects probably are drowned in the uncertainties due to the noise in the raw tidal data.

Putting it all together we have a strongly non–harmonic S_1 in air pressure, which could be additionally annually modulated like the S_1 at Potsdam. But the behaviour of the S_1 signal in gravity does not have to be equal to the signal in air pressure. Nevertheless it appears that the influence of air pressure on the FCN period is less than the influences resulting from the uncertainties of the tidal parameters.

The most recent ocean load corrections on the basis of the TOPEX/POSEIDON mission did not improve the NDFW parameter estimate. No significant effect on the parameters could be detected. *Schastok* [1995] remarked that past estimates of the ocean’s effects on nutations could conceivably have overlooked non–negligible contributions from higher order ocean–tide harmonics. If such contributions would turn out to be important, there would be presumably implications for the nutation results, since a crucial point in all FCN/NDFW studies are the ocean corrections to the observed amplitudes and phases.

It must be mentioned that the ocean correction for the small amplitude tides ψ_1 and ϕ_1 are derived from the tide K_1 , because for BFO no individual models were available. Therefore corrections for K_1 are scaled with the amplitude of ψ_1 and ϕ_1 , respectively. The same was done for the generation of the random ocean load errors. This results consequently in larger ocean errors for the tidal constituents P_1 and K_1 . The random ETERNA error (error of tidal analysis) is scaled with respect to the parameter uncertainty from the tidal analysis. So the random ETERNA errors of ψ_1 and ϕ_1 are the largest. This is important, since the constituent closest to the resonance frequency has the largest influence.

With some errors being large, the linear approximation of the model function breaks down, and this exhibits the need for an error estimation beyond standard errors. The Monte Carlo method allows to propagate the errors (exact formulation: the uncertainties) of the tidal estimates into the uncertainties of the NDFW parameters without any linearization approximation, which for instance is implied

by using the analytical solution with Taylor series expansion. The analytical error propagation has a poor data basis, whereas the Monte Carlo simulations provide a sufficient basis for statistical error considerations. Last but not least, by estimating uncertainties from Monte Carlo simulations, correlations between parameters have implicitly been taken into consideration in projecting all simulation results onto the subspace of interest. All this makes the Monte Carlo simulations the best applicable method for retrieving more conservative parameter estimates.

The inversion with fixed infinite Q shows that its amount can virtually be changed unlimited to higher values. This will be compensated by higher estimates of the resonance strength in the fitting procedure. So the resonance period and its uncertainty remain unaffected with respect to the unconstrained inversion. In conclusion, there are similar results for free and infinite fixed Q in the resonance period. The Q -factor depends heavily on the tidal constituent closest to the resonance period which unfortunately happens to be also the smallest constituent with respect to SNR. This leads to parameter estimates for Q which do not seem to be reasonable. The estimated Q -factor is negative and distinguishable from positive values. Without physical justification for a negative Q -factor, the existence of systematic error influences may be the explanation. The phase of the tide ψ_1 together with the ψ_1 ocean correction, which is only a very poor estimate as mentioned before, is suspected to be a significant error source. With systematic errors of this kind being unknown up to now, they could not be considered in previous publications of other authors. But systematic effects due to the missing of an individual model for the load effect of ψ_1 must appear globally. So it would be useful to apply a similar error analysis to all kind of tidal data used to constrain the CMB ellipticity and to make every effort to develop an individual model for the ocean correction of the tide ψ_1 . Concerning the imperfect ocean corrections the station BFO has the advantage of the large distance to the oceans compared to other stations.

It is now common practice to interpret the lower observational values of the resonance period with reference to the hydrostatic value as increased ellipticity of the core-mantle boundary. Since in this work the frequency shift is about twice the frequency shift of *Neuberg et al.*, [1990], consequently the amount of ellipticity increase must be about twice the value they obtained, namely 500 to 700 m with the extremal values for elastic and anelastic mantle, respectively. Normal mode splitting analyses for the retrieval of the structure coefficient C_2^0 which is sensitive for the ellipticity of the core do not produce significant estimates. Therefore the estimation of the ellipticity of the core is best performed by core resonance analyses of tides or nutations.

Glossary of notations

Abbreviations

Symbol	Meaning
A	equatorial moment of inertia, real part of resonance strength
A^C, A^M	equatorial moment of inertia of core or mantle
\mathbf{A}^T	Matrix \mathbf{A} transposed
α, α^C	dynamical ellipticity of whole Earth or core
α	error probability
B	imaginary part of resonance strength
β	parameter uncertainty
\mathbf{C}	covariance matrix
c_s^t	structure coefficient
C_l^m	coefficient of spherical harmonic expansion
C, C^C, C^M	polar moment of inertia of the whole Earth, core or mantle
D	dilatation, complex tidal admittance
Δ	tilt, parameter uncertainty
δ	δ -factor
ε_{ij}	strain tensor
ε	parameter uncertainty
f_{NDFW}	resonance frequency
G	gravitational constant
g	gravity
γ	damping constant
\mathbf{F}	volume force
h_2^0	boundary perturbation
θ	spherical co-latitude
$\boldsymbol{\theta}$	solution vector
h_n, k_n and l_n	Love numbers
K	bulk modulus
λ	Lamé constant, spherical longitude, singular value
$M(\omega_j)$	model of harmonic oscillator
M	mass of tide generating body
μ	shear modulus
∇	nabla operator
ω	angular frequency
ω_{NDFW}	angular resonance frequency
P_n	Legendre polynomials
P_n^m	associated Legendre functions
Q	quality factor

Continuation of Abbreviations

Symbol	Meaning
R, R^C	mean radius of the Earth or core
$R_0(\theta)$	hydrostatic figure of the core
$\Delta R^C(\theta)$	deviation from the hydrostatic figure of the core
\mathbf{S}	stress tensor
S_l^m	coefficient of spherical harmonic expansion
${}_n S_l$	spheroidal normal mode
σ	standard error
${}_n T_l$	toroidal normal mode
T_{FCN}	resonance period
t	time
u	displacement
V	tidal potential
χ^2	misfit
ξ	azimuthal angle

Constants

1 sidereal day	= 0.99726958 solar days
G	= $6.6732 \cdot 10^{-11} m^3 kg^{-1} s^{-2}$ (Gravitational constant)
Mantle $(C - A)/C$	= $1/298.69 = 0.00335^1$
Core $(C - A)/C$	= $1/389.10 = 0.00257^1$ (PREM)
R^C	= 3480 km (PREM)
i	= $\sqrt{-1}$

Expressions

$\delta_{ij} = \begin{cases} 1 & \text{for } i = j \\ 0 & \text{for } i \neq j \end{cases}$	Kronecker symbol
$C_{ij} = \int_V \rho (x_k x_k \delta_{ij} - x_i x_j) dV$	components of the tensor of inertia

¹[Dickey, 1995]

References

- Abramowitz, M. and Stegun, I., Handbook of Mathematical Functions, *Dover Publications*, New York, 1968.
- Agnew, D. C., Strainmeters and Tiltmeters, *Rev. Geophys.*, Vol 24, No. 3, 579 – 624, 1986.
- Agnew, D. C., Ocean-load tides at the South Pole: A validation of recent ocean-tide models, *Geophys. Res. Let.*, Vol. 22, No. 22, 3063 – 3066, 1995.
- Agnew, D. C., SPOTL: Some programs for ocean–tide loading, *Reference Series 96–8, June 18*, Institute of Geophysics and Planetary Physics, Scripps Institution of Oceanography, Univ. of California, San Diego, La Jolla, 1996.
- Bevington, P. R., Data reduction and error analysis for the physical sciences, *McGraw–Hill*, New York, 1969.
- Chao, B. F., As the world turns, *EOS, Trans. Am. Geophys. Union*, 66, 766 – 770, 1985.
- Chapman, S. and Lindzen, R. S., Atmospheric tides, *Reidel*, Dordrecht, 1970.
- Constable, C. and Tauxe, L., The bootstrap for Magnetic Susceptibility Tensors, *J. Geophys. Res.*, 95, 8383 – 8395, 1990.
- Crossley, D. J., Jensen, O. G. and Hinderer, J., Effective barometric admittance and gravity residuals, *Phys. Earth Planet. Inter.*, 90, 183 – 195, 1995.
- Cummins, P. and Wahr, J., A study of the Earth’s free core nutation using International Deployment of Accelerometers gravity Data, *J. Geophys. Res.*, 98, 2091 – 2104, 1993.
- Defraigne, P., Dehant, V. and Hinderer, J. Stacking gravity tide measurements and nutation observations in order to determine the complex eigenfrequency of the nearly diurnal free wobble. *J. Geophys. Res.*, 99, 9203 – 9213, 1994.
- Defraigne, P., Dehant, V. and Hinderer, J., Correction to ‘Stacking gravity tide measurements and nutation observations in order to determine the complex eigenfrequency of the nearly diurnal free wobble’, *J. Geophys. Res.*, 100, 2041 – 2042, 1995.
- Dehant, V., Tidal parameters for an Inelastic Earth, *Phys. Earth Planet. Inter.*, 49, 97 – 116, 1987.
- Dickey, J. O., Earth Rotation, *Global Earth Physics: A handbook of physical constants, American Geophysical Union reference shelf; 1*, (Ed.: Ahrens), Washington, 356 – 368, 1995.
- Doornbos, D. J. and Hilton, T., Models of the Core–Mantle Boundary and the Travel Times of Internally Reflected Core Phases, *J. Geophys. Res.*, 94,

- 15741 – 15751, 1989.
- Draper, N. R. and Smith, H., Applied Regression Analysis, *John Wiley & Sons*, New York, 1966.
- Dziewonski, A. M. and Anderson, D. L., Preliminary reference Earth model (PREM), *Phys. Earth Planet. Inter.*, 25, 297 – 356, 1981.
- Eanes, R. and Bettadpur, S., The CSR3.0 global ocean tide model, *Center for Space Research, Technical Memorandum*, CSR-TM-95-06, 1995.
- Farrell, W. E., Deformation of the Earth by surface loads, *Rev. Geophys. Space Phys.*, 10, 761 – 797, 1972.
- Florsch, N., Chambat, F., Hinderer, J. and Legros, H., A simple method to retrieve the complex eigenfrequency of the earth's nearly diurnal free wobble; application to the Strasbourg superconducting gravimeter data, *Geophys. J. Int.*, 116, 53 – 63, 1994.
- Forte, A. M., Mitrovica, J. X. and Woodward, R. L., Seismic-geodynamic determination of the origin of excess ellipticity of the core-mantle boundary. *Geophys. Res. Lett.*, Vol. 22, No. 9, 1013 – 1016, 1995.
- Francis, O. and Mazzega, P., Global charts of ocean tide loading effects. *J. Geophys. Res.*, 59, 11411 – 11424, 1990.
- Gilbert, F. and Dziewonski, A. M., An application of normal mode theory to the retrieval of structural parameters and source mechanisms from seismic spectra, *Phil. Trans. R. Soc. Lond.*, A278, 187 – 269, 1975.
- Goodkind, J. M., Q of the nearly diurnal free wobble, *Proc. 9th Int. Symp. Earth Tides*, New York, 1981, (Ed.: Kuo, J.T.), Schweizerbart, Stuttgart, 569 – 575, 1983.
- Gwinn, C. R., Herring, T. A. and Shapiro, I. I., Geodesy by radio interferometry: Studies of the forced nutations of the Earth. 2nd Interpretation, *J. Geophys. Res.*, 91, 4755 – 4765, 1986.
- Harrison, J. C., Earth tides, *Benchmark paper in geology*, Vol. 85, Van Nostrand Reinhold Company Inc., New York, 1985.
- Hartmann, T. and Wenzel, H.-G., The HW95 tidal potential, *Geophys. Res. Lett.*, Vol. 22, No. 24, 3553 – 3556, 1995.
- He, X. and Tromp, J., Normal Mode Constraints on the Structure of the Earth, *J. Geophys. Res.*, 101, B9, 20053 – 20082, 1996.
- Herring, T. A. and Dong, D., Measurement of diurnal and semidiurnal rotational variations and tidal parameters of Earth, *J. Geophys. Res.*, 99, 18051 – 18071, 1994.
- Herring, T.A., Gwinn, C.R. and Shapiro, I.I., Geodesy by radio interferometry:

- Studies of the forced nutations of the Earth. *J. Geophys. Res.*, *91*, 4745 – 4754, 1986.
- Herring, T. A., Buffett, B. A., Mathews, P. M. and Shapiro, I. I., Forced Nutations of the Earth: Influence of Inner Core Dynamics, 3. Very Long Interferometry Analysis, *J. Geophys. Res.*, *91*, 4755 – 4765, 1991.
- Hinderer, J., Legros, H. and Amalvict, M., A search for Chandler and nearly diurnal free wobbles using Liouville equations, *Geophys. J. R. astr. Soc.*, *71*, 303 – 332, 1982.
- Hinderer, J., Zürn, W. and Legros, H., Interpretation of the strength of the ‘nearly diurnal free wobble’ – resonance from stacked gravity tide observations. *Proc. 11th Int. Symp. Earth Tides*, Helsinki, 1989, (Ed.: Kakkuri, J.), Schweizerbart, Stuttgart, 549 – 555, 1991.
- Hough, S. S., The oscillations of a rotating ellipsoidal shell containing fluid, *Phil. Trans. R. Soc. A*, *186*, 469 – 506, 1895.
- Jiang, X., Wobble-nutation modes of the Earth, *Ph.D. Thesis*, Department of Physics, Univ. York, North York, Ont., 1993.
- Jiang, X. and Smylie, D. E., A search for free core nutation modes in VLBI nutation observations, *Phys. Earth Planet. Inter.*, *90*, 91 – 100, 1995.
- Kohl, M. L., Measurement and Interpretation of Tidal Tilts in Southern California, *Ph.D. thesis*, Univ. of Colorado, Boulder, 1993.
- Kohl, M. L. and Levine, J., Measurements and Interpretation of tidal tilts in a small array. *J. Geophys. Res.*, *100*, 3929 – 3941, 1995.
- Lamb, H., Hydrodynamics, *6th ed.* Cambridge University Press, Cambridge, 1932.
- Lambeck, K., Geophysical Geodesy, Clarendon Press, Oxford, 718 pp, 1988.
- Lawson, C. L. and Hanson, R. J., Solving Least Squares Problems, Prentice-Hall, Englewood Cliffs, N.J., 1974.
- Le Provost, C., Bennet, A. F. and Cartwright, D. E., Ocean tides for and from TOPEX/POSEIDON, *Science*, *267*, 639 – 642, 1995.
- Le Provost, C., Genco, M. L., Lyard, F., Vincent, P. and Canceil, P., Spectroscopy of the world ocean tides from a finite element hydrodynamic model, *J. Geophys. Res.*, *99*, 24777 – 24797, 1994.
- Levine, J., Harrison, J. C. and Dewhurst, W., Gravity tide measurements with a feedback gravity meter, *J. Geophys. Res.*, *91*, 12835 – 12841, 1986.
- Mathews, P. M., Buffett, B. A., Herring, T. A. and Shapiro, I. I., Forced nutations on the Earth: Influence of inner core dynamics, 1. Theory, *J. Geophys. Res.*, *96*, 8219 – 8242, 1991.

- Mathews, P. M., Buffett, B. A. and Shapiro, I. I., Love numbers for diurnal tides: Relation to wobble admittances and resonance expansions, *J. Geophys. Res.*, *100*, 9935 – 9948, 1995.
- Merriam, J. B., Atmospheric excitation of the Earth's rotation rate, *Variations in Earth's rotation, Geophys. Monogr. 59*, (Eds.: Mc Carthy, D. D. and Carter, W. E.), IUGG, Washington D. C., 119 – 126, 1990.
- Merriam, J. B., The Atmospheric Pressure Correction in Gravity at Cantley, Quebec, *Proc. 12th Int. Symp. Earth Tides*, Beijing, China, 1993, in press.
- Merriam, J. B., The Nearly Diurnal Free Wobble Resonance in Gravity measured at Cantley, Quebec, *Geophys. J. Int.*, *119*, 369 – 380, 1994.
- Morelli, A. and Dziewonski, A. M., Topography of the core–mantle boundary and lateral homogeneity of the liquid core, *Nature*, *Vol 325, No. 6106*, 678 – 683, 1987.
- Mukai, A., Higashi, T., Takemoto, S., Nakagawa, I. and Naito, I., Accurate estimation of atmospheric effects on gravity observations made by a superconducting gravity meter at Kyoto, *Phys. Earth Planet. Inter.*, *91*, 149 – 159, 1995.
- Munk, W. H. and MacDonald, G. J. F., The Rotation of the Earth, *Cambridge University Press*, Cambridge, 323 pp, 1960.
- Neuberg, J., Erdkernresonanz im ganztägigen Gezeitenband, *Diss. Univ. Karlsruhe*, 137 pp, 1987.
- Neuberg, J., Hinderer, J. and Zürn, W., Stacking gravity tide observations in Central Europe for the retrieval of the complex eigenfrequency of the Nearly Diurnal Free Wobble, *Geophys. J. R. astron. Soc.*, *91*, 853 – 868, 1987.
- Neuberg, J., Hinderer, J. and Zürn, W., On the complex eigenfrequency of the 'Nearly Diurnal Free Wobble' and its geophysical interpretation, *Geophysical Monograph 59: Variations in Earth Rotation*, (Eds.: McCarthy, D. D. and Carter, W. E.), IUGG volume 9, AGU and IUGG, Washington D.C., 11 – 16, 1990.
- Neuberg, J. and Zürn, W., Investigation of the Nearly Diurnal Resonance using Gravity, Tilt and Strain data simultaneously, *Proc. 10th Int. Symp. Earth Tides*, Madrid, 1985, (Ed.: R. Vieira), Cons. Sup. Invest. Cient., 305 – 311, 1986.
- Peterson, J., Observations and Modeling of seismic background noise, *Open-File Report 93 – 332*, U.S. Department of Interior, Geological Survey, Albuquerque, New Mexico, 1993.
- Nelder, J. A. and Mead, R., A simplex method for function minimization, *Computer Journal*, *7*, 308 – 313, 1965.

- Polzer, G. Zürn, W. and Wenzel, H. G., NDFW analysis of Gravity, Strain and Tilt Data from BFO, *Bull. Inf. Mar. Terr.*, 125, 9514 – 9545, 1996.
- Press, W. H., Teukolsky, S. T., Vetterling, W. T. and Flannery, B. P., (Eds.), Numerical recipes – C version, *Cambridge University Press*, Cambridge, 2nd ed., 994 pp, 1992.
- Richter, B., Wenzel, H.–G., Zürn, W. and Klopping, F., From Chandler wobble to free oscillations: comparison of cryogenic gravimeters and other instruments in a wide period range, *Phys. Earth Planet. Inter.*, 91, 131 – 148, 1995.
- Richter, B. and Zürn, W., Chandler Effect and Nearly Diurnal Free Wobble as determined from Observations with a superconducting Gravimeter, *Proc. IAU Symp. 128, The Earth's Rotation and Reference Frames for Geodesy and Geodynamics*, Coolfont, Virginia 1986, (Eds.: Babcock, A. K., Wilkins, G. A.), 309 – 315, 1988.
- Rochester, M. G., Jensen, O. G. and Smylie, D. E., A search for the Earth's 'Nearly Diurnal Free Wobble', *Geophys. J. R. astr. Soc.*, 38, 349 – 363, 1974.
- Sasao, T., Okubo, S. and Saito, M., A simple theory on the dynamical effects of a stratified fluid core upon nutational motion of the Earth, *Proc. IAU Symp.: Nutation and the Earth's rotation*, (Eds.: Fedorov, E. P., Smith, M. L. and Bender, P. L.), Reidel, Dordrecht, 165 – 183, 1980.
- Sato, T., Fluid Core Resonance Measured by Quartz Tube Extensometers at the Esashi Earth Tides Station, *Proc. 11th Int. Symp. Earth Tides*, Helsinki, 1989, (Ed.: Kakkuri J.), Schweizerbart, Stuttgart, 573 – 582, 1991.
- Sato, T., Tamura, Y., Higashi, T., Takemoto, S., Nakagawa, I., Morimoto, N., Fukuda, Y., Segawa, J. and Seama, N., Resonance Parameters of the Free Core Nutation Measured from Three Superconducting Gravimeters in Japan, *J. Geomag. Geoelectr.*, 46, 571 – 586, 1994.
- Schastok, J., Nutations of an Anelastic Earth with Oceans, *Abstracts, IUGG, XXI General Assembly*, Boulder, Colorado, B, p. 22, 1995.
- Scherneck, H. G., Regional Ocean Tide Modelling, *Proc. 11th Int. Symp. Earth Tides*, Helsinki, 1989, (Ed.: Kakkuri, J.), Schweizerbart, Stuttgart, 57 – 582, 1991.
- Sommerfeld, A., Theoretische Vorlesungen über Physik, Band I Mechanik *Geest & Portig*, Leipzig, 1964.
- Schüller, K., Simultaneous tidal and multi-channel input analysis as implemented in the HYCON-method, *Proc. 10th Int. Symp. Earth Tides*, Madrid 1986 (Ed.: R. Vieira), Cons. Sup. Invest. Cient., 515 – 520, 1986.
- Schwahn, W., Effects of inertial forces due to the forced nutation on the gravime-

- ter factor in the diurnal range, *Bull. Inf. Mar. Terr.*, 121, 9036 – 9042, 1995.
- Schwiderski, E. W., On charting global ocean tides, *Rev. Geophys. Space Phys.*, 18, 243 – 268, 1980.
- Siebert, M., Atmospheric tides, *Advances in Geophysics*, 7, 105 – 182, 1961.
- Tamura, Y., A Harmonic Development of the Tide-Generating Potential, *Bull. Inf. Mar. Terr.*, 99, 6813 – 6855, 1987.
- Toomre, A., On the ‘Nearly Diurnal Wobble’ of the Earth, *Geophys. J. R. astr. Soc.*, 38, 335 – 348, 1974.
- Volland, H., Atmospheric Tidal and Planetary Waves, *Kluwer, Dordrecht*, 348 pp, 1988.
- Wahr, J. M., Body Tides on an Elliptical, Rotating, Elastic and Oceanless Earth, *Geophys. J. R. astr. Soc.*, 64, 677 – 703, 1981.
- Wahr, J. and Bergen, Z., The effects of mantle anelasticity on nutations, earth tides, and tidal variations in rotation rate, *Geophys. J. R. astr. Soc.*, 87, 633 – 668, 1986.
- Wahr, J. M. and de Vries, D., The Earth forced nutations: Geophysical implications, in: *Variations in Earth’s rotation*, *Geophys. Monogr.* 59, D. D. McCarthy and W. E. Carter (eds.), IUGG, Washington D. C., 79 – 84, 1990.
- Wang, R., Tidal response of the Solid Earth, *Tidal Phenomena*, (Eds.: Wilhelm, H., Zürn, W. and Wenzel, H.–G.), Springer, Berlin, 27 – 26, 1997.
- Warburton, R. J. and Goodkind, J. M., The Influence of Barometric-Pressure Variations on Gravity, *Geophys. J. R. astr. Soc.*, 48, 281 – 292, 1977.
- Wenzel, H.–G., PRETERNA – a preprocessor for digitally recorded tidal data, *Bull. Inf. Mar. Terr.*, 118, 8722 – 8734, 1994(a).
- Wenzel, H.–G., Earth tide analysis Package ETERNA 3.0, *Bull. Inf. Mar. Terr.*, 118, 8719 – 8721, 1994(b).
- Wenzel, H.–G., Earth tide data processing package ETERNA 3.20, *Bull. Inf. Mar. Terr.*, 120, 9019 – 9022, 1994(c).
- Wenzel, H.–G., The nanogal software: Earth tide data processing package ETERNA 3.30, *Bull. Inf. Mar. Terr.*, 124, 9425 – 9439, 1996.
- Wenzel, H.–G., Tide-Generating Potential for the Earth, *Tidal Phenomena*, (Eds.: Wilhelm, H., Zürn, W. and Wenzel, H.–G.), Springer, Berlin, 9 – 26, 1997.
- Widmer, R., The large-scale structure of the deep Earth as constrained by free oscillation observations, *PhD thesis*, Univ. California, San Diego, 150 pp, 1991.

- Widmer, R., Masters, G. and Gilbert, F., Observably split multiplets – data analysis and interpretation in terms of large-scale aspherical structure, *Geophys. J. Int.*, *111*, 559 – 576, 1992(a).
- Widmer, R., Zürn, W. and Masters, G., Observation of low-order toroidal modes from the 1989 Macquarie Rise event, *Geophys. J. Int.*, *111*, 226 – 236, 1992(b).
- Wilhelm, H., Spheroidal and torsional global response functions *J. Geophys.*, *59*, 16 – 22, 1986.
- Wilkinson, J. H. and Reinsch, C., Handbook for Automatic Computation, II, Linear Algebra, (Ed.: F.L. Bauer), *Springer-Verlag*, New York, 134 – 151, 1971.
- Woodhouse, J. H. and Dahlen, F. A., The effect of a general aspherical perturbation on the free oscillations of the earth, *Geophys. J. R. Astron. Soc.*, *53*, 335 – 354, 1978.
- Yoder, C. F., Astrometric and Geodetic Properties of Earth and the Solar System, *Global Earth Physics: A handbook of physical constants*, *American Geophysical Union reference shelf; 1*, (Ed.: Ahrens), Washington, 1 – 31, 1995.
- Zschau, J. and Wang, R., Imperfect Elasticity in the Earth's Mantle, Implications for earth tides and long period deformations. *Proc. 9th Int. Symp. Earth Tides*, New York, 1981, (Ed.: J.T. Kuo), Schweizerbart, Stuttgart, 605 – 629, 1983.
- Zürn, W., The Nearly-diurnal Free Wobble-Resonance, *Tidal Phenomena*, (Eds.: Wilhelm, H., Zürn, W. and Wenzel, H.-G.), Springer, Berlin, 95 – 109, 1997.
- Zürn, W., Neuberg, J. and Emter, D., Search for the 'Nearly Diurnal Free Wobble'-Resonance in strain-induced local tidal tilts, *Bull. Inf. Mar. Terr.*, *102*, 7107 – 7117, 1988.
- Zürn, W. and Rydelek, P. A., Investigation of the 'Nearly Diurnal Free Wobble'-Resonance in individual Tidal records, *Proc. 11th Int. Symp. Earth Tides*, Helsinki, 1989, (Ed.: Kakkuri, J.), Schweizerbart, Stuttgart, 521 – 530, 1991.
- Zürn, W. and Rydelek, P. A., Revisiting the Phasor-walkout method for detailed investigation of harmonic signals in time series. *Surveys in Geophysics*, *15*, Kluwer Academic Publishers, Netherlands, 409 – 431, 1994.
- Zürn, W., Rydelek, P. A., Polzer, G. and Weinbrecht, J., Identification of Persistent Harmonic Signals Using the Phasor-Walkout Method, *Proc. 12th Int. Symp. Earth Tides*, Beijing, 1993, (Ed.: Hsu, H. T.), Science Press, 279 – 287, 1995.
- Zürn, W., Rydelek P. A. and Richter B., The Core-resonance Effect in the Record from the Superconducting Gravimeter at Bad Homburg, *Proc. 10th*

Int. Symp. Earth Tides, Madrid 1986, (Ed.: R. Vieira), Cons. Sup. Invest. Cient., 141 – 147, 1986.

Zürn, W. and Wilhelm, H., Tides of the solid Earth, *Landolt-Börnstein: New Series, Volume V/2a, Geophysics of the solid Earth, the Moon and the Planets*, (Eds.: Soffel, H. and Fuchs, K.), Springer, Berlin, 280 – 299, 1984.

Appendix A

The instrument responses

The transfer functions of the instruments LaCoste–Romberg gravimeter ET–19, the Askania borehole pendulum BLP10 and the Cambridge–Invar strainmeter St3 from the station BFO are shown in Fig. A.1 in the frequency range of 10^{-3} to 10^5 *cpd* in the representation of amplitude and phase. A pole and zero representation is published on the Internet at URL <http://www-gpi.physik.uni-karlsruhe.de/pub/widmer/BFO>. The instrument responses of all the instruments include the response of the analog anti–aliasing filter. In the case of the strainmeter (as well as barometer though not shown here) the frequency dependence is totally dominated by this filter.

Because of the plateau in the relevant diurnal period range, the transfer functions can be assumed to be constant. Then for the calibration of the instruments only a specific calibration constant has to be applied in each case.

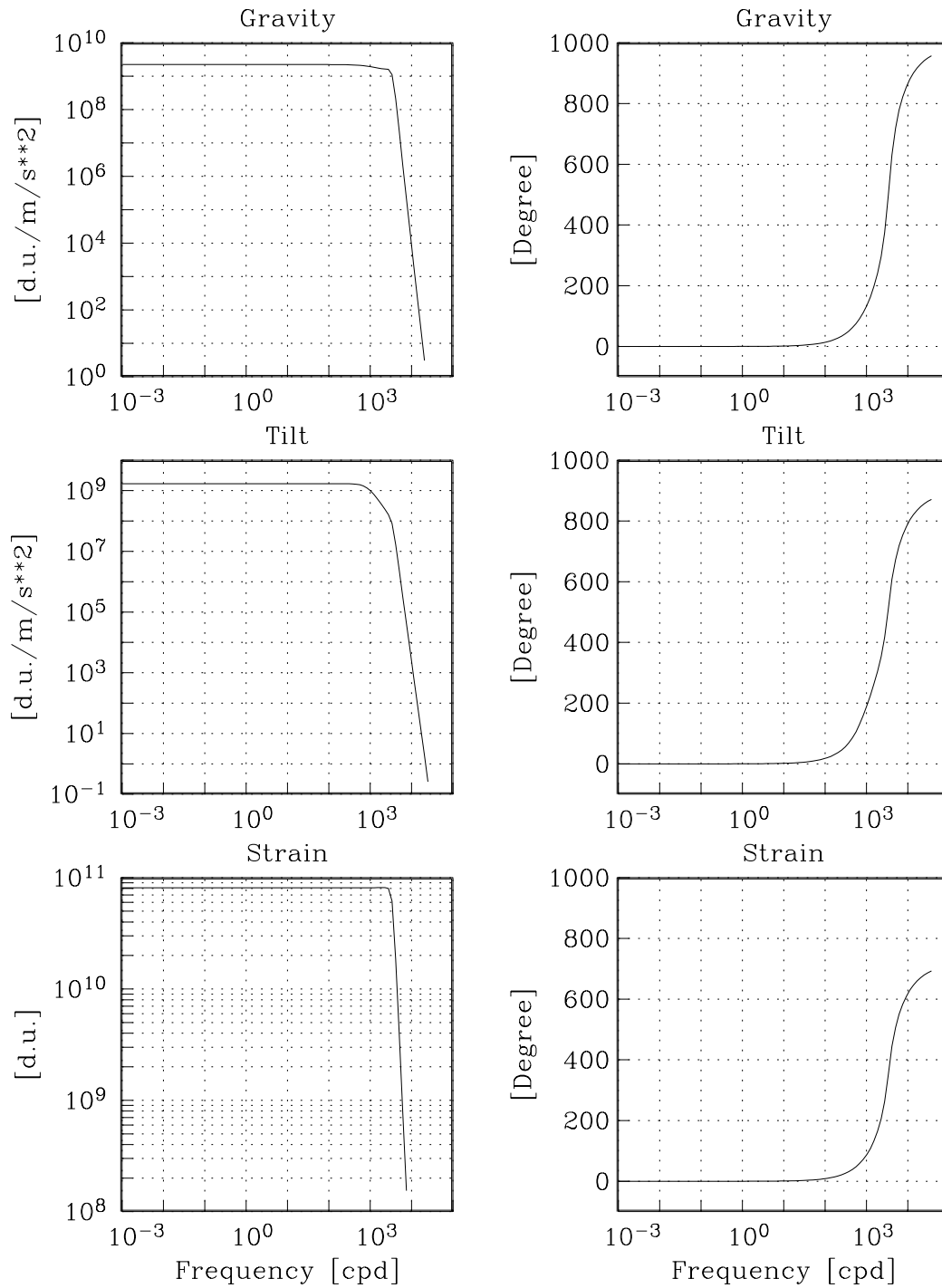


Figure A.1: Transfer functions of the LaCoste–Romberg gravimeter ET–19, the Askania borehole pendulum BLP10 and the Cambridge–Invar strainmeter St3. The left column shows the amplitude transfer functions in digital units per m/s^2 and digital units for strain. On the right column the phase transfer functions in degrees are shown. The phase is allowed to reach multiples of 2π .

Appendix B

Tidal observations

In Fig. B.1 the spectra of the high-pass filtered time series of gravity, strain and tilt are shown. The corresponding time series registered by the LaCoste-Romberg Gravimeter ET-19 with electrostatic feedback, the Cambridge-Invar-Strainmeter St3 (azimuth N 300°E) and the Askania borehole pendulum BLP10 (EW-component) are the input to the tidal analysis with the ETERNA program. The long period contributions, of whatever origin, Earth response or instrument drift have been suppressed by the ETERNA high-pass filter no 6 in all data sets. Clearly distinguishable are the diurnal, semi-diurnal and ter-diurnal tidal bands. The simultaneously recorded air pressure with its prominent spectral lines due to the harmonics of the solar day has already been shown in Fig. 4.2.

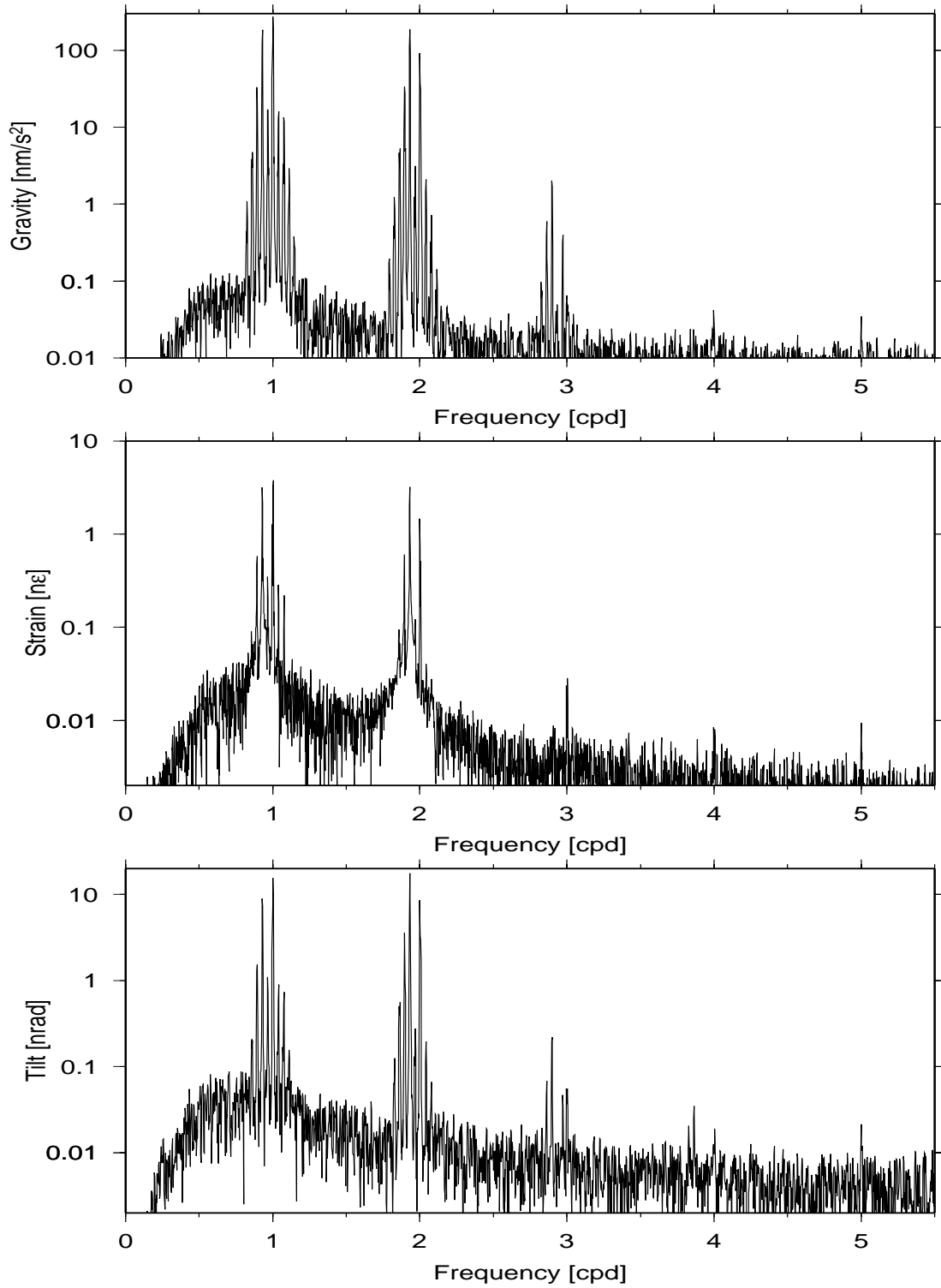


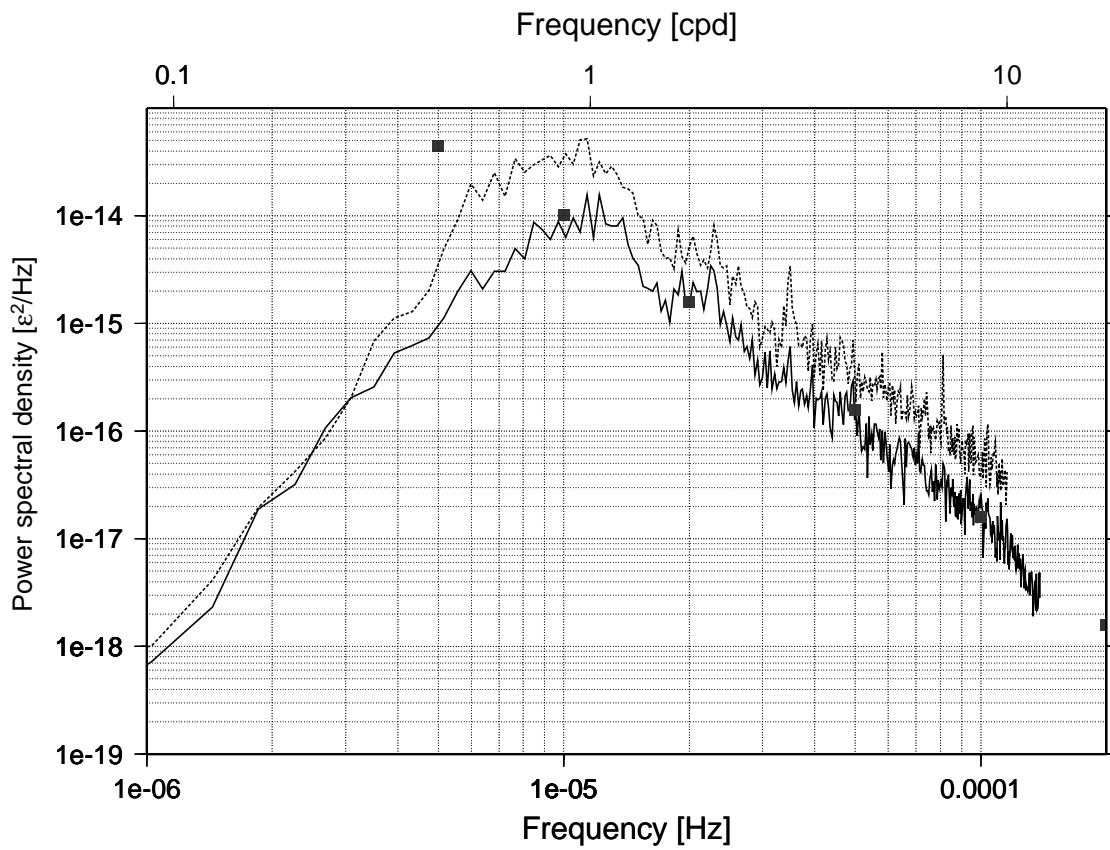
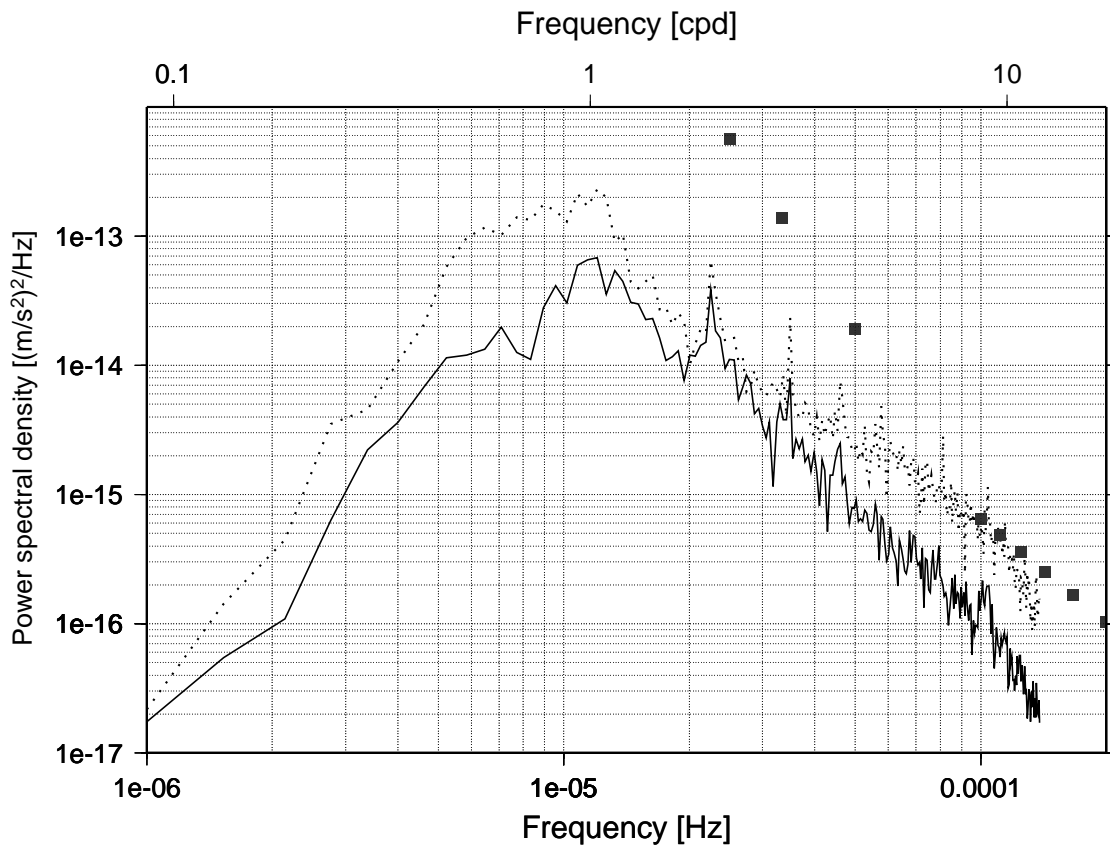
Figure B.1: Highpass filtered spectra of gravity (≈ 13 month), strain (≈ 20 month) and tilt (≈ 13 month) observations from station BFO.

Appendix C

Comparison with Noise Models

To classify the quality of the data used in this work in a broad context, additionally to the comparison to older data sets from the station BFO (3.2) the residuals after the tidal analysis are compared to published noise models. In Fig. C.1 and Fig. C.2 the residuals after the tidal analysis are shown in the representation of power spectral densities with each spectral datum representing a mean over 21 elementary bandwidths. The origin of the data is visible in the texture of the graph. So in each case the solid squares depict the noise model. The continuous curves represent the residuals when the air pressure is fitted and removed in the tidal analysis, whereas the dashed lines corresponds to tidal analyses without measures for air pressure influence due to meteorologic or thermal effects. In all cases the noise reduction due to the subtraction of air pressure is prominent. The largest effect is demonstrated in gravity. Also, in the range [$\approx 1 - 5$ *cpd*] the BFO gravity residuals are significantly smaller than the mean value of a selection of stations represented by the noise model. In Fig. C.1 the gravity residuals are compared to the New Low Noise Model (NLNM) [Peterson, 1993]. For this model registrations of 75 stations from different global seismograph networks were compiled. The noise model for strain and tilt is based on the best data from the NW laser strainmeter and the long fluid tiltmeter at Piñon Flat Observatory [Agnew, 1986] (Fig. C.2).

The noise sources in this frequency range are assumed to be thermoelastic deformations, pore pressure changes, joint deformation related to ground water motion and air pressure changes. Diurnal and seasonal temperature variations, rainfall and fluctuations in the ground–water table may also strain and tilt the crust and produce periodic noise. The roll–off at low frequencies in the tidal residuals is caused by the high–pass filter in ETERNA (Chapter 3.2) and therefore has no significance.



Left-hand side:

Figure C.1: Residuals from tidal analysis at station BFO. Upper panel: Power spectral density of gravity residuals (LaCoste–Romberg gravimeter ET–19), lower panel: power spectral density of strain residuals (the Cambridge–Invar strainmeter St3). The solid square symbols belong to the respective noise models.

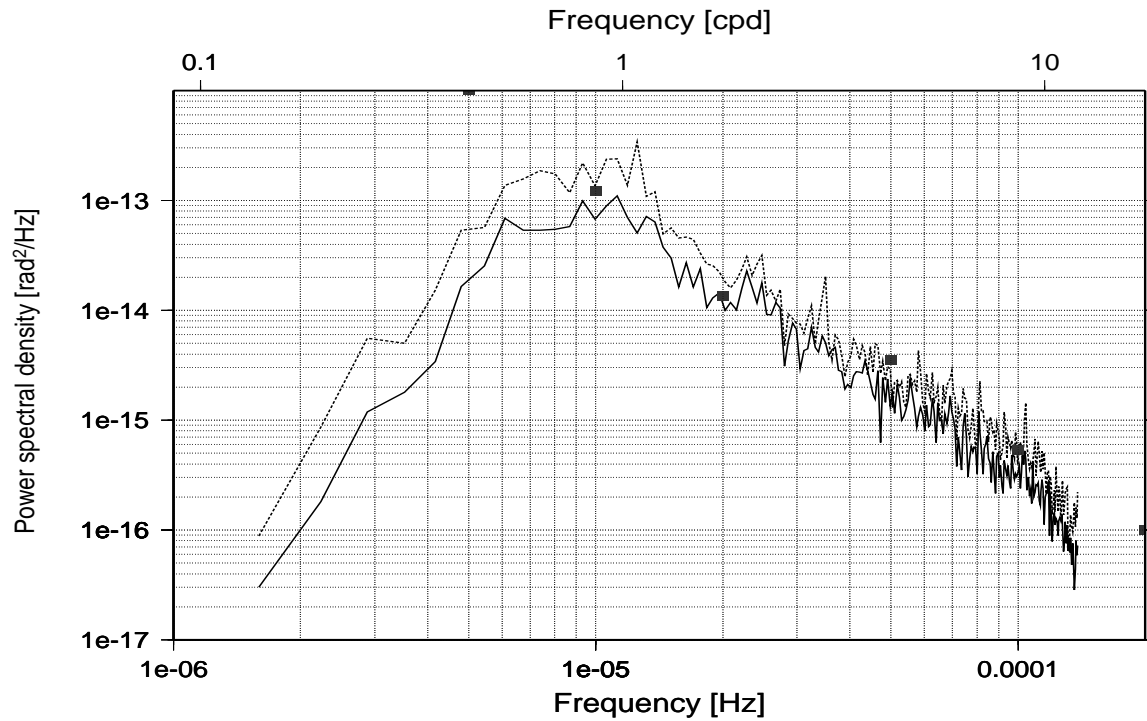


Figure C.2: Residuals from tidal analysis at station BFO. Power spectral density of tilt residuals obtained by the tidal analysis of the registrations of the Askania borehole pendulum BLP10. The solid square symbols belong to the tilt noise model.

Acknowledgements

I thank Prof. Dr. Helmut Wilhelm for being my referee. Prof. Dr. Hans-Georg Wenzel I wish to thank for being referee, for carefully reading the manuscript and for providing his ETERNA software package including his sound advice from long years of experience. I sincerely thank Dr. Walter Zürn who was always a patient and critical advisor. Especially I would like to thank Dr. Rudolf Widmer-Schmidrig for his ever present interest in my work, for fruitful discussions and providing software. I thank Dr. Gabi Laske and Dr. Fred Pollitz for their interest in my work and being committed colleagues. Thanks to all the other colleagues who contributed to the nice atmosphere to work in. I thank Dr. Duncan Agnew for calculating the ocean load signals for BFO. Support from Deutsche Forschungsgemeinschaft under grant We 1653/1 made this work possible and is gratefully acknowledged. Calculations were performed by a SUN-ELC-workstation under the operating system SunOS 4.1.1 with the graphical user surface OpenWindows and by Hewlett Packard workstations HP 715/50 under HP-UX 9.05 and Visual User Environment 3.0. This thesis was written in L^AT_EX_{2 ϵ} .